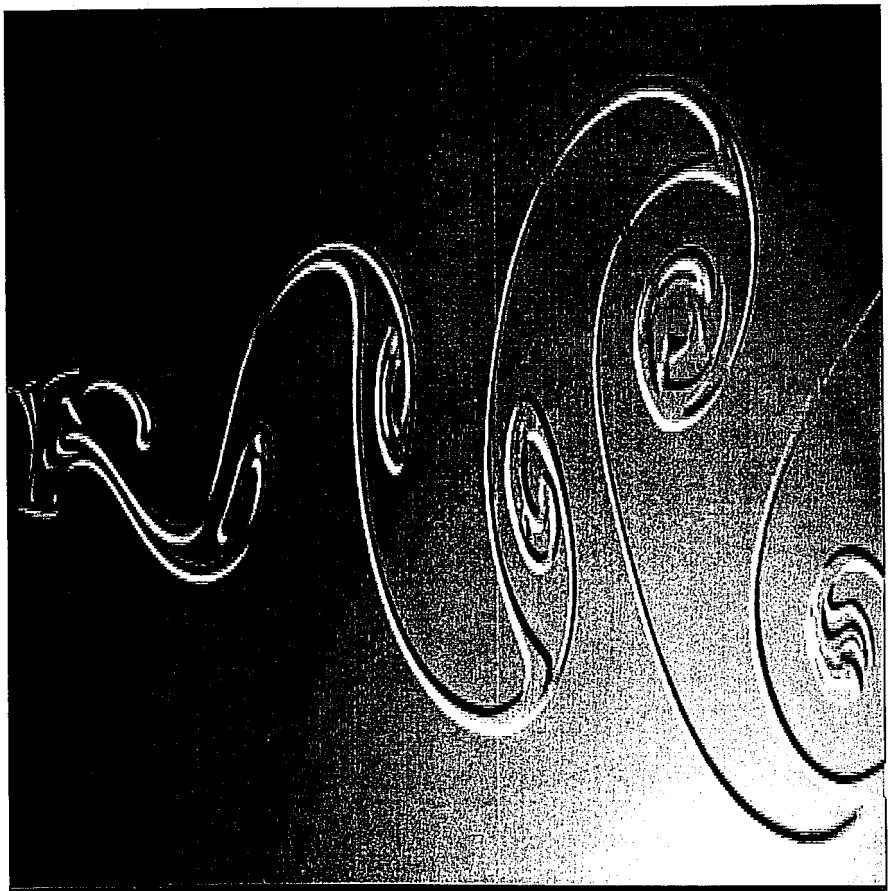

Transição e Turbulência

I Escola de Primavera — Anais - Vol.II

Associação Brasileira de Ciências Mecânicas - ABCM

Instituto Alberto Luiz Coimbra de Pós-Graduação e
Pesquisa de Engenharia - COPPE/UFRJ
Instituto Militar de Engenharia - IME/RJ

21 a 25 de Setembro de 1998, Rio de Janeiro, Brasil.

Transição e Turbulência
I Escola de Primavera

Associação Brasileira de Ciências Mecânicas - ABCM

ABCM
Carlos Alberto de Almeida, Presidente
Hans Ingo Weber, Vice-Presidente
Paulo Batista Gonçalves, Secretário Geral
Felipe Bastos de F. Rachid, Diretor de Patrimônio
Nestor Alberto Zouain Pereira, Secretário

Comitê de Ciências Térmicas da ABCM
Antônio César P. Brasil Jr.
Leonardo Goldstein Jr.
José Alberto do Reis Parise
Jurandir ItizoYanagihara
Atila P. Silva Freire
João Luís F. Azevedo
Sílvia Azucena Nebra de Perez

Conselho Científico da Escola de Primavera

Álvaro T. Prata	UFSC
Atila P. Silva Freire	COPPE/UFRJ
Daniel Onofre A. Cruz	UFPA
Leonardo Goldstein Jr.	UNICAMP
Luis Fernando A. Azevedo	PUC/RJ

Palestrantes Convidados Internacionais

Robert A. Antonia	University of Newcastle, Australia
Leslie J. S. Bradbury	Plymouth University, UK
Marcel Lesieur	Institut National Polytechnique, França
Michael Gaster	Queen Mary College, UK

Palestrantes Convidados Nacionais

Angela O. Nieckele	Pontifícia Universidade Católica/RJ
Antônio César P. Brasil Jr.	Universidade de Brasília
Aristeu da Silveira Neto	Universidade Federal de Uberlândia
Atila P. Silva Freire	COPPE/UFRJ
Daniel Onofre A. Cruz	Universidade Federal do Pará
César J. Deschamps	Universidade Federal de Santa Catarina
Luis Fernando A. Azevedo	Pontifícia Universidade Católica/RJ
Philippe Patrick M. Menut	COPPE/UFRJ

Editores

Atila P. Silva Freire	COPPE/UFRJ
Philippe Patrick M. Menut	COPPE/UFRJ
Su Jian	COPPE/UFRJ

Secretários

Mila R. Avelino	UERJ
Cláudio C. Pellegrini	FUNREI
Patricia Chedier	COPPE/UFRJ

AMBASSADE DE FRANCE
Service Culturel, Scientifique
et de Coopération

Coordenação de Aperfeiçoamento
de Pessoal de Nível Superior

Fundação Universitária
José Bonifácio

A I Escola de Primavera em Transição e Turbulência é uma iniciativa do Comitê de Ciências Térmicas da Associação Brasileira de Ciências Mecânicas (ABCM). Sonho antigo da comunidade de mecânica dos fluidos, ela agora se torna realidade graças ao entusiasmo de alguns pesquisadores e o apoio generoso de certas entidades.

O Conselho Britânico, a Embaixada da França e a CAPES financiaram a vinda dos palestrantes internacionais. O apoio decisivo da Fundação José Bonifácio permitiu que os Anais com as contribuições técnicas e as notas dos mini-cursos estivessem disponíveis aos participantes em tempo hábil. A Reitoria da UFRJ e a COPPE/UFRJ garantiram a acomodação de todos os palestrantes convidados, nacionais e internacionais. A FADESP, Federação de Amparo ao Desenvolvimento do Estado do Pará, financiou a viagem de alguns palestrantes nacionais.

O CNPq, a FAPERJ e a FINEP colaboraram com a impressão do livro sobre Turbulência e de um volume especial da Revista Brasileira de Ciências Mecânicas dedicado ao evento, os quais deverão estar à disposição dos leitores a partir do começo do ano que vem.

O Instituto Militar de Engenharia cedeu graciosamente suas excelentes instalações para estagiar o evento. Seu corpo de professores e funcionários foi sempre muito solicito.

Finalmente, reitero o enorme apoio recebido da UFRJ, em todos os níveis, para o pleno sucesso da Escola de Primavera em Transição e Turbulência. Em tempos difíceis, de críticas contundentes e dilacerantes, é sempre um conforto ter a certeza de pertencer a uma instituição séria, com excelente quadro funcional, discente e docente.

APSF

Spectral Eddy-Viscosity Based LES of Shear and Rotating Flows
Marcel LESIEUR, Frank DELCAYRE, Eric LAMBALLAIS e
Jorge SILVESTRINI 321

The Pulsed Wire Anemometer - Review and Further Developments
Leslie J. S. BRADBURY 339

Interaction entre Deux Panaches Turbulents d'un Mélange Gáz-Liquide
Philippe P. M. MENUT, Antonio E. dos Santos FERREIRA, e
Jader R. BARBOSA Jr. 365

Numerical Study of Turbulent Boundary Layer Flow over a
Surface with Step Change in Roughness - A Comparison
with Experimental Data
Mila R. AVELINO 377

Interação entre Distribuição de Fases e Estrutura de Turbulência
em Escoamentos Bi-fásicos com Bolhas - Uma Revisão
Ana Cristina R. CASTRO and Jian SU 391

Estudo Comparativo de Camada Limite Turbulenta Compressível
usando Modelo Algébrico e Kappa-Epsilon
Wagner M. Brasil e Jian Su 409

Spectral Eddy-Viscosity Based LES of Shear and Rotating Flows

Marcel Lesieur , Frank Delcayre , Eric Lamballais[2], and Jorge Silvestrini

LEGI-IMG, B.P. 53, 38041 Grenoble Cedex 09, FRANCE
[2] Université de Poitiers, CEAT, 86793 Poitiers, FRANCE

Abstract. We present the eddy-viscosity concept in Fourier space. For large-eddy simulations (LES) of isotropic turbulence, EDQNM eddy coefficients are compared with those obtained through a double filtering in spectral space. Afterwards, we present the spectral-dynamic model, which accounts for cutoff spectra not following Kolmogorov's law, It is applied with success to a temporal mixing layer and a plane channel. In the latter case, we show how the pressure pdf goes from a symmetric shape at the wall to a very skewed distribution in the channel centre, remembering the pdf's observed in isotropic turbulence and mixing layers.

For flows in complex geometries, we employ the filtered structure-function model, or the selective structure-function model. The first is applied to a spatial mixing layer, and the second to a backward-facing step. In the latter case, we discuss vortex identification with the aid of the Q-criterion.

The last application concerns incompressible rotating shear layers, very important for turbomachinery and GFD applications: we show in particular in some anticyclonic conditions a universal behaviour (both for free-shear and wall flows) of the local Rossby number, which becomes constant and equal to -1. We explain this result by a nonlinear longitudinal re-orientation of the absolute vorticity.

1 LES in Physical Space

We first recall the basic formalism of large-eddy simulations (see e.g. [1] for a review). The density ρ_0 is assumed to be uniform. Let $G_{\Delta x}$ be a low-pass filter, where Δx is characteristic of the grid size. We define the filtered field associated to a function $f(\boldsymbol{x},t)$ by

$$\bar{f}(\boldsymbol{x},t) = f * G_{\Delta x} = \int f(\boldsymbol{y},t) G_{\Delta x}(\boldsymbol{x}-\boldsymbol{y}) d\boldsymbol{y} \quad . \tag{1}$$

The filter has to be chosen in order to properly eliminate the subgrid scales of wavelength smaller than Δx. It commutes with space and time derivatives if Δx is constant in space and time, which will be assumed here. Let us consider Navier-Stokes equations

$$\frac{\partial u_i}{\partial t} + \frac{\partial}{\partial x_j}(u_i u_j) = -\frac{1}{\rho_0}\frac{\partial p}{\partial x_i} + \frac{\partial}{\partial x_j}(2\nu\, S_{ij}) \quad , \tag{2}$$

where

$$S_{ij} = \frac{1}{2}\left(\frac{\partial u_i}{\partial x_j} + \frac{\partial u_j}{\partial x_i}\right) \tag{3}$$

is the deformation tensor. Let us apply the filter to Navier-Stokes:

$$\frac{\partial \bar{u}_i}{\partial t} + \frac{\partial}{\partial x_j}(\bar{u}_i \bar{u}_j) = -\frac{1}{\rho_0}\frac{\partial \bar{p}}{\partial x_i} + \frac{\partial}{\partial x_j}(2\nu \bar{S}_{ij} + T_{ij}) \quad , \tag{4}$$

where

$$T_{ij} = \bar{u}_i \bar{u}_j - \overline{u_i u_j} \tag{5}$$

is the subgrid stresses tensor. The filtered continuity equation writes

$$\frac{\partial \bar{u}_j}{\partial x_j} = 0 \quad . \tag{6}$$

If an eddy-viscosity assumption is done, we have:

$$T_{ij} = 2\nu_t(\boldsymbol{x}, t)\ \bar{S}_{ij} + \frac{1}{3} T_{ll}\ \delta_{ij} \quad , \tag{7}$$

where the eddy viscosity ν_t has to be specified, and the LES momentum equations write

$$\frac{\partial \bar{u}_i}{\partial t} + \frac{\partial}{\partial x_j}(\bar{u}_i \bar{u}_j) = -\frac{1}{\rho_0}\frac{\partial \bar{P}}{\partial x_i} + \frac{\partial}{\partial x_j}[2(\nu + \nu_t)\bar{S}_{ij}] \ . \tag{8}$$

We have introduced a modified pressure

$$\bar{P} = \bar{p} - \frac{1}{3}\rho_0 T_{ll} \quad . \tag{9}$$

Eddy viscosities classically used are Smagorinsky's[2], the structure-function model[3], and more recently the dynamic Smagorinsky's model[4].

In fact, the eddy-viscosity model is just based upon an analogy with molecular dissipation: molecular viscosity ν characterizes for a "macroscopic" fluid parcel the momentum exchanges with the surrounding fluid due to molecular diffusion across its interface. Here, the molecular viscosity is justified through kinetic-theory models of liquids or gases which assume a wide separation between macroscopic and microscopic scales. No such scale-separation exists in the LES problem, where one observes in general a distribution of energy continuously decreasing from the energetic to the smallest dissipative scales, even in inflexional shear flows with vigorous coherent vortices. Hence the lack of spectral gap is a major drawback of the eddy-viscosity assumption.

In this respect, the spectral eddy-viscosity idea is preferable, provided one can work in Fourier space, which applies only to simple geometries.

2 LES in Fourier Space

2.1 Spectral eddy coefficients

We assume that Navier-Stokes is written in Fourier space. This requires statistical homogeneity in the three directions of space, but we will see below how to handle flows with one direction of inhomogeneity. Let

$$\hat{u}_i(k,t) = \left(\frac{1}{2\pi}\right)^3 \int e^{-ik.x}\ u(x,t)dx \tag{10}$$

(defined in the framework of generalized-functions theory) be the spatial Fourier transform of the velocity field. We define $k_C = \pi\Delta x^{-1}$ as the cutoff wavenumber. The filter is a sharp filter such that

$$\overline{\hat{f}} = \hat{f} \ \text{ for } \ |k| < k_C = \pi/\Delta x, \overline{\hat{f}} = 0 \ \text{ for } \ |k| > k_C \tag{11}$$

Let us write Navier-Stokes in Fourier space in the following form

$$\begin{aligned} &\tfrac{\partial}{\partial t}\hat{u}_i(k,t) + [\nu + \nu_t(k|k_C)]k^2\hat{u}_i(k,t) \\ &= -ik_m\left(\delta_{ij} - \tfrac{k_ik_j}{k^2}\right)\int_{|p|,|q|<k_C}^{p+q=k} \hat{u}_j(p,t)\hat{u}_m(q,t)dp \end{aligned} \tag{12}$$

where the spectral eddy viscosity $\nu_t(k|k_C)$ is defined by

$$\begin{aligned} &\nu_t(k|k_C)k^2\hat{u}_i(k,t) = \\ &ik_m\left(\delta_{ij} - \tfrac{k_ik_j}{k^2}\right)\int_{|p|\text{or}|q|>k_C}^{p+q=k} \hat{u}_j(p,t)\hat{u}_m(q,t)dp\ . \end{aligned} \tag{13}$$

With this definition, the eddy viscosity may not be real. A spectral eddy-diffusivity may be defined in the same way: one writes the passive-scalar equation in Fourier space as

$$\frac{\partial}{\partial t}\hat{T}(k,t) + [\kappa + \kappa_t(k|k_C)]k^2\hat{T}(k,t) = -ik_j\int_{|p|,|q|<k_C}^{p+q=k} \hat{u}_j(p,t)\hat{T}(q,t)dp \tag{14}$$

with

$$\kappa_t(k|k_C)k^2\hat{T}(k,t) = ik_j\int_{|p|\text{or}|q|>k_C}^{p+q=k} \hat{u}_j(p,t)\hat{T}(q,t)dp\ . \tag{15}$$

2.2 EDQNM plateau-peak coefficients

Equations (13) and (15) define the eddy coefficients in terms of the subgrid motions, which are unknown. We will in fact determine these coefficients at an energetic level, writing the evolution equations for the kinetic-energy and passive-scalar spectra given by a two-point closure of isotropic turbulence,

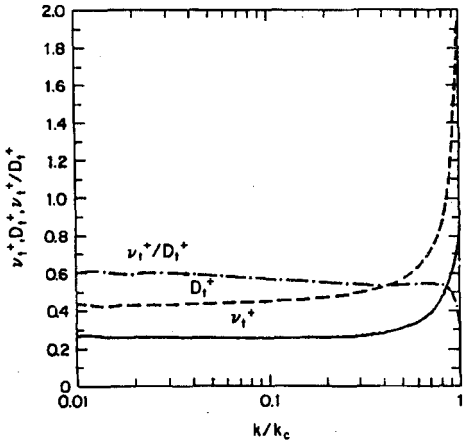

Figure1. EDQNM spectral eddy coefficients in a 3D Kolmogorov cascade

the EDQNM[1] theory (see [5]). Splitting the transfers across k_C in the same way as done in Eqs (12) and (14) one can calculate the eddy-coefficients. For three-dimensional isotropic turbulence, and if k_C lies within a long $k^{-5/3}$ range, it is found

$$\nu_t(k|k_C) = 0.441\ {C_K}^{-3/2} X(k/k_C) \left[\frac{E(k_C)}{k_C}\right]^{1/2} \tag{16}$$

where C_K is the Kolmogorov constant, $E(k_C)$ the kinetic-energy spectrum at k_C, and $X(k/k_C)$ a non-dimensional function equal to 1 up to about $k/k_C = 1/3$, and sharply rising above ("plateau-peak" behaviour, see [6]). An analogous study using the Test-Field Model (TFM)[2] had previously been done by Kraichnan [7]. However, Kraichnan did not point out the scaling of the eddy viscosity against $[E(k_C)/k_C]^{1/2}$, which turns out to be essential for LES purposes. The function $0.441\ {C_K}^{-3/2} X(k/k_C)$ of Eq. (16) is represented on Fig. 1, taken from [8]. The plateau part can be obtained analytically through leading-order expansions with respect to the small parameter k/k_C. It does in fact corresponds to a regular eddy viscosity in physical space, as if there was a spectral gap, with the gap part ($E(k) = 0$) extending up to k_C, and a Kolmogorov energy spectrum above. As for the "peak" (Kraichnan called it "cusp"), it is mostly due to semi-local interactions across k_C (such that $p << k \sim q \sim k_C$), and contains also possible backscatter contributions coming from subgrid modes p and q much larger than k_C. The latter are however very small if k_C lies in a $k^{-5/3}$ cascade, as can easily

[1] Eddy-Damped Quasi-Normal Markovian

[2] This model is in fact equivalent to the EDQNM model in a Kolmogorov inertial range.

be shown (see [1] p 51). Fig. 1 presents also the EDQNM eddy diffusivity and the corresponding turbulent Prandtl number, calculated in [8]. The eddy diffusivity has also the plateau-peak behaviour, and the turbulent Prandtl number is approximately constant (≈ 0.6) in Fourier space. In fact, such a value is the highest one permitted by adjustments of the constants arising in the passive-scalar spectrum EDQNM equation (see [5], pp 259-260, and also [9]).

2.3 LES of isotropic turbulence

We have carried out LES of decaying isotropic turbulence[10][11][3], using the EDQNM plateau-peak eddy coefficients defined above. Exemples of these calculations are shown on Figure 2. Initial spectra are $\sim k^8$ in the infrared region. One sees an initial infrared k^4 backscatter, well described by the EDQNM theory (see [5] p 245). We see also the ultraviolet kinetic-energy cascade which builds up: first, a $k^{-5/3}$ slope forms at the cutoff, then it steepens slightly and evolves towards a k^{-2} slope during the self-similar decay. On the other hand, the passive scalar has a very short Corrsin-Oboukhov's $k^{-5/3}$ range close to k_C, and a large anomalous range shallower than k^{-1} in the energetic scales. This range is interpreted by [3] as due to the rapid stirring of the scalar fluctuations by the coherent vortices of such a turbulence. The latter consist in long and thin tubes of high vorticity and low pressure, which have been characterized numerically by various groups since the work of Siggia [?]. On the figure, the cutoff is $k_C \approx 60$. We have considered a fictitious cutoff $k'_C = k_C/2$, performed a double filtering in Fourier space across k_C and k'_C: let us decompose the kinetic-energy transfers across k'_C as

$$T_{>k'_C}(k) = T_{>k_C}(k) + T_{k'_C<;<k_C}(k) \qquad (17)$$

where $T_{k'_C<;<k_C}(k)$ involves triad integrals such that

$$|p|_{\text{or}}|q| > k'_C \quad , \quad |p|_{\text{and}}|q| < k_C \quad .$$

Eq. (17) is is the exact energetic equivalent of Germano's identity[4] in spectral space, stressing that the subgrid transfers[3] across k'_C are equal to the subgrid transfers across k_C plus "resolved" subgrid transfers across k'_C. Figure 3 shows the eddy viscosity $-(1/2)k^{-2}T_{k'_C<;<k_C}(k)$ derived from the resolved subgrid transfers in the calculations of [3][4], and the equivalent eddy diffusivity for a passive scalar. Both are normalized by $[E(k'_C)/k'_C]^{1/2}$ It confirms that the plateau-peak behaviour does exist for the eddy viscosity, but is questionable for the eddy diffusivity. This anomaly is certainly related to the existence of the large-scale k^{-1} scalar spectrum found above. It is shown in [3] that the anomaly disappears when the temperature is no more passive and coupled with the velocity within the frame of Boussinesq approximation (stable stratification).

[3] of momentum, or scalar

[4] The same is obtained in [10]

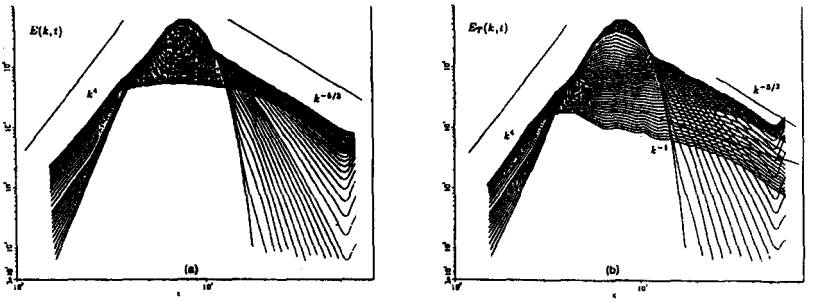

Figure2. LES of 3D isotropic decaying turbulence, from [10]

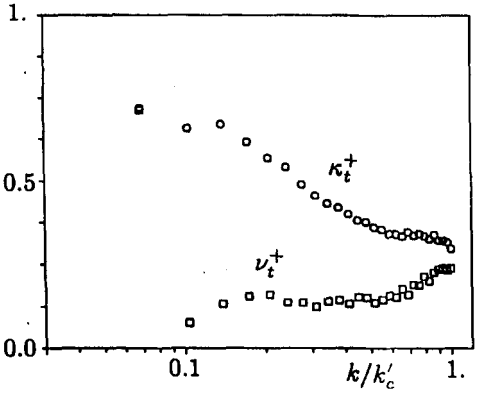

Figure3. LES of 3D isotropic decaying turbulence, resolved eddy-viscosity and diffusivity calculated trough a double filtering (from [3])

2.4 Spectral-dynamic model

The plateau-peak model assumed a $k^{-5/3}$ kinetic-energy spectrum at the cutoff. Let us now consider spectra $\propto k^{-m}$ for $k > k_C$, with $m \neq 5/3$. We re-calculate analytically the plateau with the same EDQNM leading-order expansions in k/k_C as above. We retain the peak shape through $X(k/k_C)$ in order to be consistant with the Kolmogorov spectrum expression of the eddy viscosity. The spectral eddy viscosity is now

$$\nu_t(k|k_C) = 0.31 C_K{}^{-3/2} \sqrt{3-m}\,\frac{5-m}{m+1} X(k/k_C) \left[\frac{E(k_C)}{k_C}\right]^{1/2}, \qquad (18)$$

for $m \leq 3$ (see [3]). For $m > 3$, the scaling is no more valid, and the eddy viscosity will be set equal to zero. In the spectral-dynamic model, the exponent m is determined through the LES with the aid of least-squares fits of

the kinetic-energy spectrum close to the cutoff. Within this approximation, the turbulent Prandtl number is

$$P_r^t = 0.18\ (5 - m) \tag{19}$$

(see [5]).

We have applied the spectral-dynamic model to the temporal mixing layer. Here, the spectrum allowing to determine the exponent m is calculated by a spatial average in the computational box. In the case of an initial 3D white-noise perturbation, statistical data concerning velocity, rms velocity fluctuations and Reynolds stresses are in very good agreement with the experiments of unforced mixing layers carried out in Stanford. The simulation with a quasi two-dimensional forcing is less good from this standpoint. We recall that the second case yields a vortex topology consisting of quasi 2D Kelvin-Helmholtz billows stretching intense longitudinal hairpins, while the first one gives rise to a helical-pairing type interaction between the big vortices (see [14][5]).

2.5 Plane Poiseuille flow

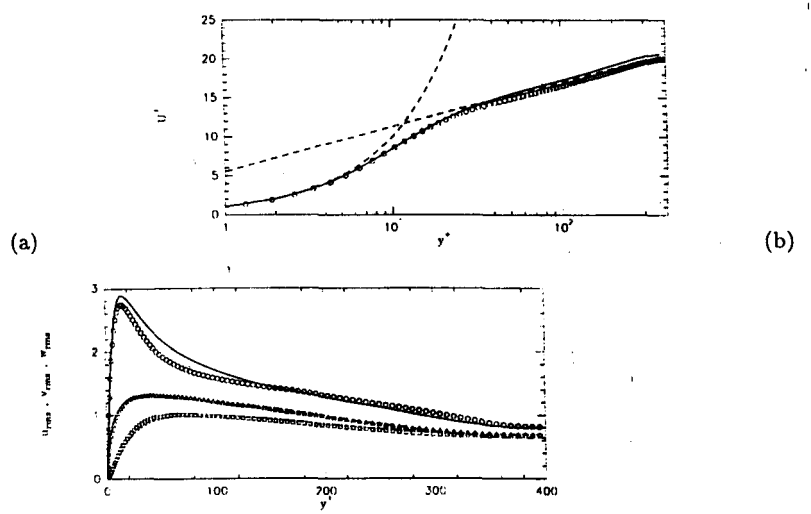

Figure4. Turbulent channel flow, comparisons of the spectral-dynamic model (straight lines, $h^+ = 389$) with the DNS of Kim ([17], symbols, $h^+ = 395$); a) mean velocity, b) rms velocity components.

We present now spectral-dynamic model results for a periodic channel. We use a mixed spectral-compact code, the compact scheme being employed

in the transverse direction, while pseudo-spectral methods are used in the longitudinal and spanwise directions which are periodic. Calculations start with a parabolic Poiseuille velocity profile, to which a small 3D white-noise perturbation is superposed, and are run up to complete statistical stationarity, assuming a constant flow rate of average velocity U_m across the section. The channel has a width $2h$. The kinetic-energy spectrum allowing to determine the eddy-viscosity is calculated at each time step by averaging in planes parallels to the walls, so that m is a function of (y,t). The code has been validated with a DNS at $h^+ = 160$, and compares very well with purely spectral DNS at same Reynolds, as far as the first and second-order statistics are concerned. At $h^+ = 204$, the first and second-order velocity statistics compare still well with the LES of [15] using the classical dynamic model. We present here one LES at $R_e = 2hU_m/\nu = 14000$ ($h^+ = 389$), taken from [16]. There is a grid refinement close to the wall, in order to simulate accurately the viscous sublayer (first point at $y^+ = 1$). We have compared the calculation with a DNS at $h^+ = 395$ carried out in [17]. Figure 4 shows the mean velocity and the rms velocity components. The agreement is very good, which is a severe challenge for the model. Notice that the LES allows to reduce the computational cost by a factor of the order of 100, which is huge.

3 Structure-Function Models

For many practical applications, the geometry of the domain is too complex to allow for pseudo-spectral, or even spectral, methods to be used. In this case, numerical schemes are formulated in physical space, and the LES subgrid model has to be expressed in physical space also.

In fact, the cusp part of the plateau-peak eddy viscosity can be formulated in physical space in the form of a hyperviscosity (see [18]). However, the implementation of the spectral-dynamic model may pose some problems with the local determination of m in physical space. Up to now, we have developed models of the structure-function family, which we will be briefly described here (see [1] [5] for more details). The idea of the structure-function model proposed in Ref. [3] is to erase the peak by subgrid-energy conservation, which yields a k-independant eddy viscosity allowing to go back to physical space. One then takes as dissipative operator in the momentum equation

$$2\frac{\partial}{\partial x_j}\left[\nu_{SF}\bar{S}_{ij}\right] \quad , \tag{20}$$

with

$$\nu_{SF}(\boldsymbol{x},t) = \frac{2}{3}\,C_K{}^{-3/2}\,\left[\frac{E(k_C,\boldsymbol{x},t))}{k_C}\right]^{1/2} \quad , \tag{21}$$

with $k_C = \pi/\Delta x$, where $E(k_C, \boldsymbol{x}, t)$ is a local kinetic-energy spectrum, calculated in terms of the local second-order velocity structure function of the filtered field

$$F_2(\boldsymbol{x}, \Delta x) = \left\langle \|\overline{\boldsymbol{u}}(\boldsymbol{x}, t) - \overline{\boldsymbol{u}}(\boldsymbol{x} + \boldsymbol{r}, t)\|^2 \right\rangle_{\|\boldsymbol{r}\| = \Delta x} \tag{22}$$

as if the turbulence is three-dimensionally isotropic. This yields for a Kolmogorov spectrum

$$\nu_t^{SF}(\boldsymbol{x}, \Delta x) = 0.105\, C_K^{-3/2}\, \Delta x\, [F_2(\boldsymbol{x}, \Delta x)]^{1/2} \quad . \tag{23}$$

F_2 is calculated with a local statistical average of square-velocity differences between $\boldsymbol{x}$ and the six closest points surrounding $\boldsymbol{x}$ on the computational grid. In some cases, the average may be taken over four points parallel to a given plane. Notice also that if the computational grid is not regular (but still orthogonal), interpolations of (23) based upon Kolmogorov's 2/3 law for the 2nd order structure function have been proposed by [1]. Such a structure-function model (SF) works very well for decaying isotropic turbulence, where it yields a fairly good Kolmogorov spectrum ([3]), better than Smagorinsky's model (with $C_S = 0.2$) and the plateau-peak models (simple or dynamic). However, these two models are too dissipative in free shear flows, and other models must be employed. As for wall flows, the SF model does not work for transition in an incompressible boundary layer where, like Smagorinsky, it is too dissipative and prevents secondary instabilities of TS waves to develop. To overcome this difficulty, two improved versions of the SF model have been developed: the selective structure-function model (SSF), and the filtered structure-function model (FSF).

In the SSF, we switch off the eddy-viscosity when the flow is not three-dimensional enough. The three-dimensionalization criterion is the following: one measures the angle between the vorticity at a given grid point and the average vorticity at the six closest neighbouring points (or the four closest points in the four-point formulation). If this angle exceeds 20^0, the most probable value according to simulations of isotropic turbulence at a resolution of $32^3 \sim 64^3$, the eddy-viscosity is turned on. Otherwise, there is only molecular dissipation which acts.

In the FSF model [19], The filtered field $\tilde{u}_i$ is submitted to a high-pass filter in order to get rid of low-frequency oscillations which affect $E(k_C, \boldsymbol{x}, t)$ in the SF model. The high-pass filter is a Laplacian discretized by second-order centered finite differences and iterated three times. It is found

$$\nu_t^{FSF}(\boldsymbol{x}, \Delta x) = 0.0014\, C_K^{-3/2}\, \Delta x\, [\tilde{F}_2(\boldsymbol{x}, \Delta x)]^{1/2} \quad . \tag{24}$$

4 Incompressible Spatial Free-Shear Layers

4.1 Spatial mixing layer

We present FSF-based LES of spatially-growing incompressible mixing layers initiated upstream by a hyperbolic-tangent velocity profile superposed

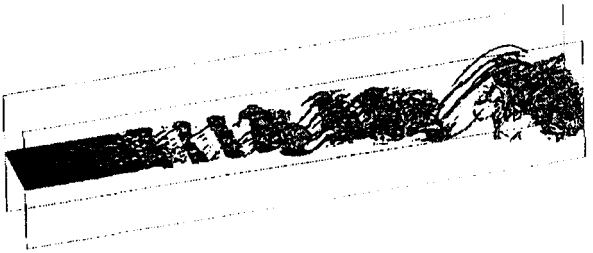

Figure5. LES of an incompressible mixing layer forced upstream by a quasi two-dimensional random perturbation; vorticity modulus at a threshold $(2/3)\omega_i$.

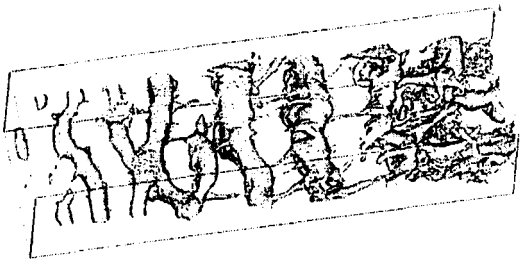

Figure6. Same as Figure 5, but with a three-dimensional upstream white-noise forcing, low-pressure field

on the average flow, plus a weak random forcing regenerated at each time step. The numerical code is the same as for the channel. With an upstream forcing consisting in a quasi two-dimensional random perturbation, intense longitudinal hairpins stretched between quasi 2D Kelvin-Helmholtz vortices are found again (Figure 5). When the forcing is a three-dimensional random white noise, helical pairing occurs upstream, as indicated by the low-pressure maps of Figure 6. But none of these simulations has reached self-similarity, and they are still dependant of the computational domain size in the three space directions. Thus calculations in bigger domains are necessary.

4.2 Backward-facing step

We consider a step of height H and expansion ratio 1.2 at a Reynolds number $U_0 H/\nu = 5100$, in a configuration studied experimentally and numerically at Stanford (see [20] for details). A schematic view of the flow and the computational domain is presented on Fig.7. A free-slip boundary condition is used on the upper boundary, well justified with respect to the laboratory experiment consisting in a double-expansion channel. The subgrid-model used is the SSF in a four-point formulation in planes parallel to the horizontal.

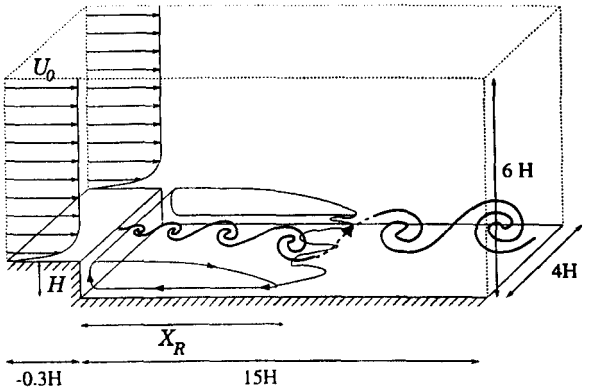

Figure 7. Schematic view of the backward-facing step computational domain

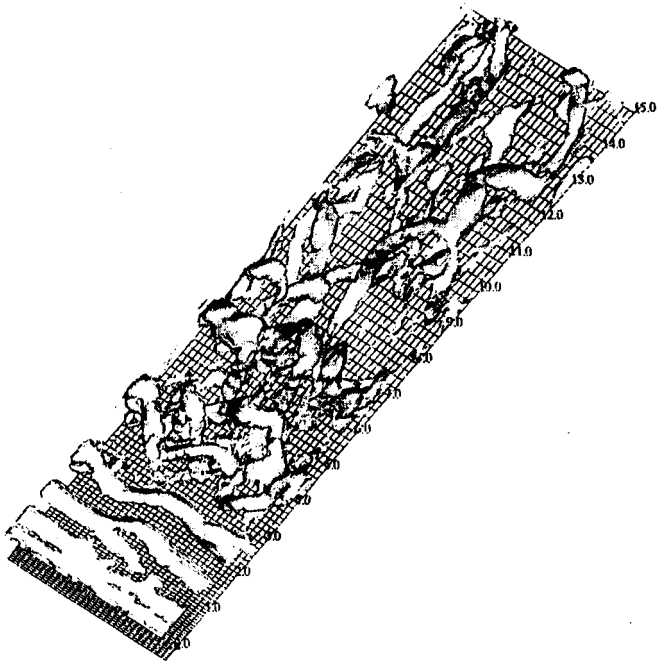

Figure 8. Backward-facing step, visualization of coherent vortices with high vorticity modulus and positive Q

The computational grid is refined in regions close to the lower wall and in the detachment region behind the step. No wall law is used. At the inlet, we impose Spalart's [21] mean turbulent boundary-layer velocity profile, to which a small 3D white noise perturbation is superposed. We have an Orlanski's outflow boundary condition, and periodicity in the spanwise direction. The coherent vortices are visualized with the aid of surfaces of high vorticity modulus and positive Q. The latter is defined in the following way: if one decomposes the velocity-gradient tensor as $S_{ij} + \Omega_{ij}$, where S_{ij} and Ω_{ij} are respectively the deformation and rotational components, Q is the second invariant of the velocity gradient

$$Q = \frac{1}{2}(\Omega_{ij}\Omega_{ij} - S_{ij}S_{ij}) = \frac{1}{4}(\omega^2 - 2S_{ij}S_{ij}) \quad . \tag{25}$$

A well-known result is that $\nabla^2 p = 2Q$. Indeed, the Poisson equation for the pressure writes

$$-\nabla^2 p = \frac{\partial^2}{\partial x_i \partial x_j} u_i u_j = \frac{\partial}{\partial x_i}\left[u_j \frac{\partial u_i}{\partial x_j}\right] = \frac{\partial u_i}{\partial x_j}\frac{\partial u_j}{\partial x_i} =$$

$$(S_{ij} + \frac{1}{2}\epsilon_{ij\lambda}\omega_\lambda)(S_{ji} + \frac{1}{2}\epsilon_{ji\mu}\omega_\mu) =$$

$$S_{ij}S_{ij} - \frac{1}{2}\omega^2 = -2Q \; .$$

In fact, one can easily check that in a quasi 2D coherent vortex where the isobaric lines are convex, a pressure trough in the core of the vortex implies that the pressure Laplacian, and hence Q, are in the average positive. Indeed, let C be such a close contour. We build a small vortex tube portion of cross section C and length l. The flux of the pressure gradient getting out of the tube is positive, so that, due to the divergence theorem, a spatial average of $\nabla^2 p$ within the tube is positive. Hence, $Q > 0$ is a necessary condition for the existence of a depression. In practice, simulations of various types of flows confirm that coherent vortices are well characterized by iso-surfaces of high vorticity modulus and positive Q. Fig. 8 presents such a visualization for the step. It confirms what we have observed by an animation: quasi 2D Kelvin-Helmholtz vortices are shed behind the step. Then, they undergo helical pairings and transform into a field of big staggered arch-like vortices which impact the lower wall and are carried away downstream. This scenario is confirmed by the measure of frequency pressure spectra at four positions in the flow: (1) just behind the step, just before reattachment, just behind reattachment and much further downstream. Position (1) is marked by a peak at a Strouhal number (in units U_0/H) of 0.23, corresponding to the shedding of Kelvin-Helmholtz vortices. At position (2), a second peak of higher amplitude is present at the subharmonic Strouhal number 0.12, corresponding physically to helical pairing. At positions (3) and (4), the two previous Strouhal numbers are still there, but a third peak forms at a Strouhal of 0.07, corresponding to the well-known flapping of the recirculation bubble.

5 Rotating Shear Flows

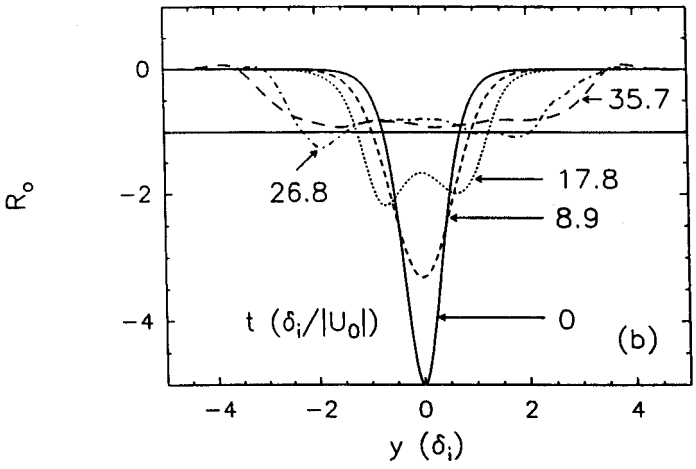

Figure 9. DNS of a weakly rotating mixing layer: evolution with time of the Rossby-number profile (courtesy O. Métais).

We consider incompressible shear layers rotating with a uniform angular velocity Ω about an axis parallel to the basic vorticity vector. Such a problem has important applications for turbomachinery (cavitation in particular) and in Geophysical Fluid Dynamics. We work in a relative rotating frame, where rotation is accounted for with the aid of a Coriolis force $-f\boldsymbol{z} \times \boldsymbol{u}$, where $\boldsymbol{z}$ is the unit vector on the spanwise axis and $f = 2\Omega$. The local Rossby number at any time is defined by

$$R_o(y) = -\frac{1}{f}\frac{d\bar{u}}{dy} \quad , \tag{26}$$

where $\bar{u}(y)$ is the mean longitudinal velocity profile. Regions with a positive (resp. negative) local Rossby will be called cyclonic (resp. anticyclonic). We recall also that the absolute vorticity vector is $\boldsymbol{\omega}_a = \boldsymbol{\omega} + f\boldsymbol{z}$, and satisfies Helmholtz theorem in its conditions of applicability.

I synthesize here results coming both from the 3D linear-stability studies of [22], and the DNS or LES of [23] and [16]. As in instability studies, we start with a basic parallel velocity profile, weakly perturbed. There is a critical local Rossby number of -1 such that:

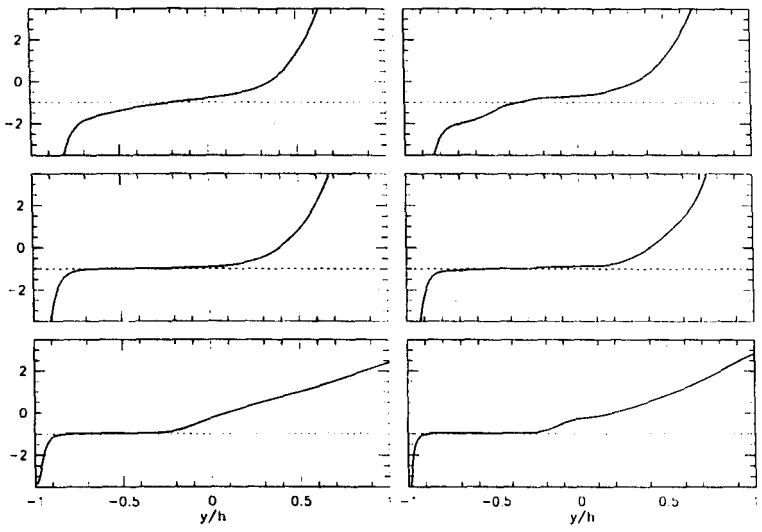

Figure10. DNS and LES of a weakly rotating channel, evolution with time of the Rossby-number profile (courtesy O. Métais).

i) In regions where initially $R_o(y) \geq -1$, the shear layer is two-dimensionalized. In a mixing layer for instance, 3D perturbations are damped, and straight Kelvin-Helmholtz billows form[5]. This result agrees in particular with Proudman-Taylor's theorem when $|R_o| << 1$.
ii) For $R_o(y) < -1$ ("weak" anticyclonic rotation), the flow is highly three-dimensionalized, with production of intense Görtler-like longitudinal rolls. They correspond to hairpins of absolute vorticity which are oriented in a purely longitudinal plane. As a result, their spanwise vorticity component is zero, which implies that the mean velocity profile becomes constant and equal to f, so that the local Rossby number uniformizes to the value -1. This is clear for the mixing layer DNS of Figure 9 (taken from [23]), and for the channel shown on Figure 10.

It is difficult to understand why the absolute vorticity is not only stretched but also re-oriented longitudinally. We propose here an exact analysis based

[5] without stretching of longitudinal vortices nor helical pairing

on Euler equations, where we assume x-independance[6]. The evolution equations (following the motion) of the absolute vorticity ω_a of components $\omega_1 = \partial w/\partial y - \partial v/\partial z, \omega_2 = \partial u/\partial z, \omega_3 + f = -\partial u/\partial y + f$ is

$$\frac{D}{Dt}\omega_a = \overline{\overline{F}} : \omega_a \quad , \tag{27}$$

with

$$\overline{\overline{F}} = \begin{pmatrix} 0 & f & 0 \\ 0 & \overline{\frac{\partial v}{\partial y}} & \overline{\frac{\partial v}{\partial z}} \\ 0 & \overline{\frac{\partial w}{\partial y}} & \overline{\frac{\partial w}{\partial z}} \end{pmatrix} = \overline{\overline{F}}_1 + \overline{\overline{F}}_2 \quad , \tag{28}$$

$$\overline{\overline{F}}_1 = \begin{pmatrix} 0 & f & 0 \\ 0 & 0 & 0 \\ 0 & 0 & 0 \end{pmatrix} \quad , \tag{29}$$

and

$$\overline{\overline{F}}_2 = \begin{pmatrix} 0 & 0 & 0 \\ 0 & \overline{\frac{\partial v}{\partial y}} & \overline{\frac{\partial v}{\partial z}} \\ 0 & \overline{\frac{\partial w}{\partial y}} & \overline{\frac{\partial w}{\partial z}} \end{pmatrix} \quad . \tag{30}$$

Here, $\overline{\overline{F}}_1 : \omega_a$ lies in a purely longitudinal plane and will stretch ω_a in this direction, since it corresponds to

$$\frac{D\omega_1}{Dt} = f\omega_2 \quad . \tag{31}$$

Let us consider now ω_n, the projection of ω_a in the y, z plane. We have

$$\frac{D}{Dt}\omega_n = \overline{\overline{F}}_2 : \omega_n \quad . \tag{32}$$

[6] Indeed, the linear-stability analysis shows that there exists a longitudinal mode which dominates shear instabilities under a Rossby of -1.

The tensor $\overline{\overline{F}}_2$ is in fact the velocity-gradient tensor in the y,z plane, and can be put under the form

$$\overline{\overline{F}}_2 : = \overline{\overline{S}}_{y,z} : + \frac{1}{2}\omega_1 \boldsymbol{x} \times \quad . \tag{33}$$

During the linear stage of evolution, DNS of [23] concerning an anticyclonic mixing layer of initial Rossby of -5 (at the inflexion point) show the growth of the longitudinal mode, with absolute vortex filaments in phase and inclined approximately 45^0 above the horizontal plane. This produces concentrations of longitudinal vorticity in the y,z plane. When applied to ω_n, the tensor $\overline{\overline{F}}_2$ will both deform it and rotate it about $\boldsymbol{x}$ in the sense of the sign of the longitudinal vorticity. Let us assume that a nonlinear regime is reached where longitudinal vorticity concentrations are strong enough to form vortices. The interior of these vortices will correspond to "elliptic" regions as defined by Weiss[24]: they are such that the eigenvalues λ of $\overline{\overline{F}}_2$ (or $-\overline{\overline{F}}_2|^t$) are imaginary. They are given by

$$\lambda^2 = -\frac{1}{2}Q \quad , \tag{34}$$

where Q has been defined by Eq. (25) in the more general 3D case, and concerns only here the tensor $\overline{\overline{F}}_2$. Remark that the "Q-criterion" does correspond in 2D to the elliptic regions of Weiss. No such result can be shown exactly in 3D when considering the eigenvalues of the velocity gradient. However, our simulations confirm that regions of high vorticity satisfying the Q-criterion are vortices.

Returning to the absolute vorticity, rotation will therefore dominate déformation in Eqs. (32,33), and the rotation of ω_n around $\boldsymbol{x}$ will imply an increase of the spanwise absolute-vorticity component (which is negative). The Rossby number (which was lower than -1) will increase also. We have here an interesting mechanism of self-reorientation of absolute-vorticity vector, possible only in a nonlinear regime.

6 CONCLUSION

We have presented the general framework of large-eddy simulations (LES) carried out in spectral space, with the plateau-peak type eddy-viscosity, derived from two-point closures of turbulence, and which permits to go beyond the scale-separation assumption inherent to the classical eddy-viscosity concept in physical space. We have verified for isotropic turbulence and with the aid of a double-filtering in spectral space that the plateau-peak does exist. We have shown how to implement the plateau-peak in physical space in terms of the combination of a regular eddy viscosity and an hyperviscosity. We have proposed also a modification of the plateau-peak to account for kinetic-energy spectra decaying differently from Kolmogorov at the cutoff.

This spectral-dynamic model has been applied to the incompressible turbulent channel flow with good results with respect to experiments and direct-numerical simulations. Compared with the latter at same Reynolds number, the LES reduces the computational cost by a factor of the order of hundred.

Returning to physical space, we have reinterpreted these models in terms of velocity-structure functions. We have applied in particular the filtered structure-function model to an incompressible spatially-growing mixing layer, with possibility of controlling the topology of the flow, depending upon the nature (quasi 2D or 3D) of the upstream perturbation. Another example of spatial mixing layer is the backstep flow, where we have applied the SSF model (Reynolds number 5100, expansion ratio 1.2). We have shown that fundamental Kelvin-Helmholtz vortices are shed behind the step, undergo helical pairing, transform into big staggered arch-like vortices which impinge the lower wall and are carried away downstream. We have determined three characteristic Strouhal numbers associated to the flow: the harmonic mode 0.23 corresponding to the shedding of Kelvin-Helmholtz vortices behind the step, a subharmonic 0.12 corresponding to helical pairings between the vortices, and a third one 0.07 associated to the recirculating bubble flapping.

Finally, we have shown by DNS and LES that, in rotating (free or wall-bounded) shear flows and if rotation Ω is not too fast, that anticyclonic shear layers organize to pick up a universal linear mean velocity profile of gradient 2Ω. These effects cannot be recovered by one-point closure modelling methods. We have proposed a theoretical interpretation of this phenomenon in terms of a nonlinear longitudinal self-reorientation of the absolute-vortex filaments.

7 Aknowledgements

We are indebted to O. Métais for numerous discussions, and P. Begou for the computational support. Most of the computating time used for the 3D calculations has been freely allocated by CNRS. Marcel Lesieur is supported by IUF.

References

1. Lesieur, M. & Métais, O., *Ann. Rev. Fluid Mech.* 28 (1996) 45-82.
2. Smagorinsky, J., *Mon. Weath. Rev.* 91, 3 (1963) 99-164.
3. Métais, O. & Lesieur, M. *J. Fluid Mech.* 239 (1992) 157-194.
4. Germano, M., U. Piomelli, P. Moin & W. Cabot, *Phys. Fluids A.* 3 (1991) 1760-1765.
5. Lesieur, M. *Turbulence in fluids, 3rd edition*, Kluwer Academic Publishers (1997).
6. Chollet, J.P. & Lesieur, M., *J. Atmos. Sci.* 38 (1981) 2747-2757.
7. Kraichnan, R.H., *J. Atmos. Sci.* 33 (1976) 1521-1536.

8. Chollet, J.P. & Lesieur, M., *La Météorologie*, 29 (1982) 183-191.
9. Herring, J.R., Schertzer, D., Lesieur, M., Newman, G.R., Chollet, J.P. & Larchevêque, M., *J. Fluid Mech.* 124 (1982) 411-437.
10. Lesieur, M. & Rogallo, R., *Phys. Fluids A* 1 (1989) 718-722.
11. Lesieur, M., Métais, O. & Rogallo, R., *C.R. Acad. Sci. Paris* Ser II 308 (1989) 1395-1400.
12. Siggia, E.D., 1981, J. Fluid Mech., **107**, pp 375-406.
13. Chollet, J.P., PhD, Grenoble University (1983)
14. Comte, P., Lesieur, M. & Lamballais, *Phys. Fluids A* 4 (1992) 2761-2778.
15. Piomelli, U., *Phys. Fluids A* 5 (1993) 1484-1490.
16. Lamballais, E., PhD, Grenoble University (1996).
17. Antonia, R.A., Teitel, M., Kim, J. & and Browne, L.W.B, *J. Fluid Mech.* 236 (1992) 579–605.
18. Métais, O., same volume.
19. Ducros, F., Comte, P. & Lesieur, M., *J. Fluid Mech.* 326 (1996) 1-36.
20. H. Le and P. Moin, Direct-numerical simulation of turbulent flow over a backward-facing step. Stanford University, Rep. TF-58 (1994).
21. Spalart, P., *J. Fluid Mech.*, 187 (1988) 61-98.
22. Yanase, S., Flores, C., Métais, O. & Riley, J., *Phys. Fluids* 5 (1993) 2725-2737.
23. Métais, O., Flores, C., Riley, J., Yanase, S. & Lesieur, M., *J. Fluid Mech.* 293 (1995) 47-80.
24. Weiss, J., *La Jolla Institute preprint* LJI-TN-121ss (1981). See also *Physica D.*, 48 (1991), 273.

THE PULSED WIRE ANEMOMETER REVIEW AND FURTHER DEVELOPMENTS

L.J.S. Bradbury
(University of Plymouth, England)

1. Introduction.

In spite of the efforts of about eighty years of fairly intensive scientific effort, our understanding of turbulent flows is far from complete and our ability to predict their behaviour is still very uncertain. There are no entirely rational theories of turbulence and all the models used to predict flow development rely on experimental data in one form or another to establish various empirical constants used in the theoretical models. Thus, the history of development of turbulence modelling has been inextricably linked to progress in turbulence measuring techniques.

In the 1930's, the only significant body of data on turbulent flow development consisted of mean velocity profiles in turbulent boundary layers and this enabled various simple momentum integral models of turbulent boundary layer development to be produced which relied on only one or two constants to enable them to be used practically. However, the predictive accuracy of these models was extremely limited and confined to situations not very different from the experimental arrangements that had been used to provide the empirical constants. With the development of the hot wire anemometer, more detailed measurements of the structure of turbulent flows became possible and higher order integral methods were developed and, with the advent of computers that could be used to solve sets of simultaneous partial differential equations, point momentum and energy equation methods were developed. However, in every case, experimental data had to be used to establish an ever enlarging set of empirical constants in the models. In many ways, the theoretical models could be viewed as a sophisticated fitting procedure to the experimental data which also ensured that an increasing hierarchy of conservation relationships were also being satisfied. However, an important drawback to the experimental data was that the hot wire anemometer could only be used in turbulent flows with comparatively low levels of turbulence relative to the local mean velocity and so most of the experimental data were still confined to boundary layer flows. However, the theoretical methods based on solutions of the Reynolds equations could be applied to flows without this restriction but, without experimental data on these flows, the predictive accuracy was unknown. There was therefore a requirement for an experimental technique which could be used to study highly turbulent flows.

Without doubt, the most important development in turbulence experimental techniques was the arrival of laser light scattering methods with Doppler difference anemometry being the most important variant. With this technique and the development of laser frequency shifting techniques, measurements could be made in turbulent flows without any restriction on turbulence levels -

although there were and are many practical and theoretical difficulties to be overcome in producing high accuracy reliable data. It is also an expensive technique and its proper application requires that the experimenter has a good understanding of lasers, optics, light scattering theory and sampling theory.

Another but far less well known technique that can be used in highly turbulent flows is the pulsed wire anemometer and the purpose of this paper is to review work that has been done on this technique and also suggest further developments that could be made in its range of application. At the outset, it should be made clear that the potential of pulsed wire anemometry is less than that of laser Doppler anemometry but, on the other hand, it has certainly enabled measurements to be made that would not have been possible previously and there is also additional scope for further developments in the technique.

There are three types of probe that have been used in pulsed wire anemometry. They are (i) the crossed wire velocity probe, (ii) the parallel wire wall shear stress probe and (iii) the parallel wire velocity probe. These will be discussed in turn.

2.0 The crossed wire velocity probe.

This is the probe configuration that has been most commonly used. The probe consists of three fine wires as shown in figure 1. The central wire is the pulsed wire and on either side of this are the sensor wires with their axes perpendicular to the pulsed wire. The principle of operation is very simple. The central wire - which is typically a 9 micron Tungsten wire of about 4 mm in length - is pulsed with a short duration voltage pulse of a few microseconds duration. The amplitude of the voltage pulsed will be discussed later but it is chosen to raise the temperature of the wire to several hundred degrees Centigrade. This causes a tracer of heated air to be released into the flow which is convected away with the velocity of the airstream passing the probe at that moment. The two sensor wires - which are usually of 2.5 micron diameter Tungsten wire - are operated as simple resistance thermometers and they are used to measure the time of arrival of the heat tracer at one or other of the two sensor wires. In an ideal situation, the time taken for the tracer to reach a sensor wire would be

$$t_c = \frac{s}{\left|\bar{U}\right| \cos\psi} \qquad (1)$$

where s is the spacing between the pulsed wire and the sensor wire, $\left|\bar{U}\right|$ is the magnitude of the velocity vector and ψ is the angle between the direction normal to the plane of the probe and the instantaneous velocity vector (see figure 1). The plane of the probe is here defined as the plane parallel to the

axes of all three wires in the probe. Thus, from the time of flight t_c, the magnitude of the velocity vector resolved at right angles to the plane of the probe can be obtained. The use of two sensor wires ensures that the flow direction is unambiguously determined; the only restriction is in the length of the wires, l, since arctan($l/2s$) gives the largest angular deviation of the flow that can be sensed. The most commonly used probes have a value of l/s of about 5 giving a yaw response up to about 70°.

In a turbulent flow, the probe is repetitively pulsed and an ensemble of velocity values is obtained from which both the mean velocity and the turbulent intensity can be deduced. Furthermore, the velocity and intensity in any direction can be obtained simply by aligning the probe in the appropriate direction. By making measurements at several angles, the flow direction can be obtained along with the normal and shear stresses. The ensemble of velocity values can be used to obtain probability estimates and, finally, by using a non-periodic sampling rate, it is also possible to obtain spectral information at frequencies above the normal Nyquist frequency.

Although the principle of the pulsed wire anemometer is very simple, its development into a useable technique involved overcoming a number of theoretical and practical problems. Most of these are covered in the early paper by Bradbury and Castro(1971) but these detailed problems will not be considered here. Castro (1992) published a comprehensive review of later developments in pulsed wire anemometry and this present paper uses some of the same examples described by Castro to illustrate the range of measurements that can be made with pulsed wire anemometry. However, the additional purpose of the present paper is to suggest some further developments in the technique.

2.1 Examples of velocity measurements with a crossed wire probe.

Before considering results of measurements with a pulsed wire anemometer, it is useful to look at typical probe calibrations. Figure 2 shows a velocity calibration. Because of the effects of thermal diffusion, the calibration of U against the reciprocal of the time of flight T is not exactly linear but a good fit to the data has been found to be given by the expression

$$U = \frac{A}{T} + \frac{B}{T^3} \qquad (2)$$

where A and B are constants found by least squares fitting to the experimental data.

Figure 3 shows a yaw calibration which according to the simple model should be a cosine law. The data fits the cosine law quite well and a yaw response is maintained up to an angle of about 70 degrees. It is shown by Bradbury and Castro (1971) that missing tracers that lie outside this angular range only have a small effect on the accuracy of turbulence measurements.

Some examples of measurements with a pulsed wire anemometer will now be considered.

The first example from Bradbury (1976) has been chosen simply to illustrate the use of the pulsed wire in a flow in which flow reversals occur and where, therefore, the turbulence levels are very high. The example also shows hot wire results to illustrate the errors that arise with this technique in such a flow. Figure 4 shows the mean velocity and turbulent intensity distributions in the wake of a normal flat plate, one plate width downstream within the reverse flow region.

The second example is a straightforward application of the pulsed wire anemometer to the study of the wake flow downstream of a model Ford Transit van - Watts (1982). Figure 5 shows contours of constant mean velocity in the wake of a model van. It shows the existence of a significant region of reverse flow and is an example of the sort of practical studies that can be undertaken with a pulsed wire anemometer.

The third example has been chosen to illustrate the use of the pulsed wire anemometer in a flow in which there are fluctuations in a foreign gas concentration - Hall (1979). The pulsed wire anemometer is a time-of-flight device and so, unlike the hot wire anemometer, is not sensitive to variations in foreign gas concentration provided the flow is sensibly isothermal. In figure 6, the mean velocity and turbulent intensity distributions are shown through a rough wall turbulent boundary layer into which a continuous heavy gas release has occured. The profiles are compared with the case when the gas release is absent. Although the turbulence levels are no higher than in an ordinary turbulent boundary layer, such results could not have be obtained with a hot wire because the presence of the foreign gas would have serious effects on the heat transfer rates from the hot wire.

Before considering other types of pulsed wire technique, it should also be mentioned that near wall measurements with a crossed wire pulsed wire probe can be made if a through wall probe is constructed. Figure 7 shows a photograph of such a probe used by Castro and Dianat (1990). In this probe, the two sensor wires are welded to electrodes flush in the wall and are mounted at right angles to the wall by being welded to an outer electrode as shown. The pulsed wire is mounted on a micrometer traversing gear and can be traversed up and down between the two sensor wires. The geometry is thus the same as that of a normal crossed wire probe but it enables measurements to be made in the very near wall region. Figure 8 shows a comparison between pulsed wire measurements and hot wire measurements in a conventional turbulent boundary layer. The hot wire measurement were confined to the outer region of the boundary but the agreement with the pulsed wire results is very good. However, very close to the wall in the sub-layer, the pulsed wire results deviate from the viscous sub-layer profile. Castro and Dianat (1990) showed that this was due the effect of thermal diffusion on the transport of the tracer and they developed a simple method for correcting for this effect. Figure 9 shows the velocity profile in the sub-

layer before and after their correction has been applied. With the correction, the agreement with the viscous sub-layer profile is now very good. Of course, the advantage of the pulsed wire probe is that it can be used in separating boundary layer flows. In addition to Castro and Dianat (1990), wall region measurements of this sort have also been made by Devenport, Evans and Sutton (1990),

2.2 Limitations of the pulsed crossed-wire probe.

It is important to stress the limitations of pulsed wire anemometry. The really significant limitations are as follows:-

(i) In order to achieve satisfactory sensor wire signals, it is generally necessary to use sensor wires of 2.5 micron diameter Tungsten. These wires are usually in the range from 3-5 mm in length and can easily be broken by mechanical shock. The probes are much more fragile than hot wire probes and an experimental environment free of significant mechanical shocks is necessary. On the other hand, this problem should not be over-exaggerated because, with experience, it is possible to use probes for a considerable period without breaking them. As an example, a probe that the author uses for checking the electronic processing circuitry has been in use for five years without breaking a wire.

The fragility of the pulsed wire probes would be greatly reduced if, instead of the 2.5 micron Tungsten wires, thin films on Quartz fibres were used for the sensor elements. The technology for doing this is certainly now available but it would no doubt require some development work in order to construct such a probe.

(ii) The velocity range over which the probe can be used is limited to a range from about 0.1-0.2 metres/sec up to about 8-10 metres/sec.. The lower limit comes from the need for the transport of the heat tracer to be dominated by convection rather than thermal diffusion. The upper limit arises from some restrictions in the signal processing circuitry and also that the single/noise ratio decreases with increasing velocity.

(iii) The flows must be isothermal. Clearly, if temperature fluctuations are present in the flow which are of the same order as the temperatures of the heat tracers then the individual heat tracer times-of-flight cannot be discerned.

3.0 The pulsed wire wall shear stress probe.

In the early period of developing the pulsed wire anemometer, Gaster (1969) suggested to the author that the technique might be used to develop a means of measuring wall shear stress that could be used in flows with large fluctuations in wall shear stress including reversals of stress direction. In the original idea, it was proposed to surface mount three parallel thin films with a geometry similar to that shown in the sketch in figure 10. The principle of

operation is very similar to the pulsed wire velocity probe in that the central film is pulsed with a short duration voltage pulse and the time for the resultant heat tracer to reach one or other of the two sensor films is measured. On the basis of simple dimensional analysis, the time of flight, t, is related to the instantaneous velocity gradient, $\partial u / \partial y$, the thermal diffusivity coefficient, κ, and the space between the pulsed and sensor films, h, by the simple functional relationship

$$\frac{\kappa t}{h^2} = function\ of\left(\frac{h^2}{\kappa}\frac{\partial u}{\partial y}\right) \qquad (3)$$

In the case of the wall probe, the transport of the heat tracer is through a combination of diffusion and convection. On the basis of a very simple argument, Bradbury and Ginder (1973) obtained a form for this relationship, namely

$$\frac{h^2}{\kappa t} = \frac{2}{3}\left(\frac{h^2}{\kappa}\frac{\partial u}{\partial y}\right)^{\frac{2}{3}} \qquad (4)$$

Experiments carried out with surface mounted thin film gauges in a laminar flow channel resulted in the calibration results shown in figure 10. Considering the simplicity of the argument behind equation (4), the agreement with its general form is very good. However, a major drawback with these surface mounted thin film results was that the signal levels were very low (typical sensor film amplitudes were of the order of a few microvolts) with a poor signal to noise ratio. In spite of various efforts to improve the situation, it proved impossible to use surface mounted thin films in a turbulent flow. In order to produce a useable wall shear stress probe, it was necessary to resort to the use of thin wires mounted close to but not touching the surface. The small air gap (typically 50 micron) avoided heat loss to the substrate and improved the signal to noise ratio dramatically. It should be added that a whole series of numerical solutions to the heat convection/conduction equation were carried out by Ginder (1971) and these confirmed the findings of the experimental observations about the effect of the substrate on reducing the signal levels.

The parallel wire wall shear stress probe (shown schematically in figure 11) has been used by several authors to study both mean and fluctuating wall shear stress in a variety of flows. Figure 12 shows some results of Ruderich and Fernholz (1986) of the mean and fluctuating wall shear stress on the splitter plate behind a normal fence.

Another example of the use of the wall shear stress probe was in the study of the flow beneath a simplified model of a tricone drilling bit. Tricone drilling bits are widely used in drilling oil wells and there is some interest in the distribution of wall shear stress produced by the three jets of drilling mud

used to remove rock particles from the drill face. White, Escudier and Gavignet (1987) carried out a study of the shear stress distributions in a simplified model of the drilling situation - see figure 13 - using air rather than mud for the jet flows. The flow around the drill bit is complex and three-dimensional and, in addition, to wall shear stress measurements with the pulsed wire probe, they also made a number of surface flow visualisation studies. Figure 14 shows an example of one of their flow visualisation results with vectors of the wall shear stress obtained from the pulsed wire probe superimposed on the flow pattern. The qualitative agreement is very good and, with the quantitative results given in the original report, is a good demonstration of the complex flows that can be studied with the pulsed wire wall shear stress probe.

The potential of the pulsed wire wall shear stress gauge seems to the author to be very significant and it has been therefore rather surprising that it has not found more widespread use - particularly in areas like the three dimensional flows over aircraft wings.

It is not possible in a short review article to cover all the facets of the pulsed wire wall shear stress probe but a more complete discussion of the technique is given by Castro, Dianat and Bradbury (1987).

3.1 Possible developments with wall shear stress measurements.

It was mentioned in section 3 that the initial idea for wall shear stress measurements was to use surface mounted thin films. The original work on these thin film gauges was included in this paper because this remains an attractive proposition. As has already been mentioned, the idea had to be abandoned originally because of the low signal to noise ratio of the surface sensor gauges. However, the signal to noise ratio would be significantly improved if, instead of using thin film gauges as resistance thermometers, thermo-electric gauges could be laid down by standard thin film vacuum deposition techniques. In principle, multi-junction thermo-couples could be produced in a thin film form and would result in a very robust probe that could be manufactured with a high degree of repeatability. In this way, individual probe calibrations might not be necessary.

4.0 Parallel wire velocity probe.

The first paper on pulsed wire anemometry was by Bauer(1965). In this paper, Bauer used a pulsed wire probe consisting of two parallel wires as shown in figure 15 . The drawback with this arrangement is that, in a turbulent flow, most of the tracer signals miss the sensor wires - which is the reason for developing the crossed wire probe discussed in section 2. On a number of occasions, this restricted angular response has been exploited by using a parallel wire probe as a yaw meter and, in particular, Almeida (1986) used such a probe in the study of a circular jet issuing into a cross flow. However, there is potential for such probes in highly turbulent flows as well.

Let us suppose that we have a parallel wire probe in a turbulent flow as shown in figure 16. It is assumed that the probe is pulsed a large number of times N and that sensor wire signals are obtained on n occasions. On each occasion that a trace is detected, we will have a velocity estimate q and, if we define an angle, $\delta\varphi$, as the angular range over which this estimate can be sensed, we may define an estimate of joint probability density function as

$$p(q,\varphi) = \frac{n}{N}\frac{1}{\delta q\,\delta\varphi}$$

where the true value is approached as $N \to \infty$ and δq and $\delta\varphi$ both tend to zero. $p(q,\varphi)$ is the probability of finding a velocity estimate in the velocity range from q to $q+\delta q$ and in the angular range from φ to $\varphi+\delta\varphi$. If this function can be measured, it enables any cross-products of the velocity fluctuations to be calculated since

$$u^a v^b = \iint (q\cos\varphi)^a (q\sin\varphi)^b\, p(q,\varphi)\, dq\, d\varphi$$

and this includes, of course, the normal and shear stresses and the turbulent diffusion term that appear in the turbulent energy equation.

The measurement of this joint probability is in principle possible with a parallel wire probe with the slight complication that the angular response of the probe is a function of the velocity q. In appendix A, the form of this function is discussed and it is shown that the angular 'window' decreases with increase in velocity due to the smaller diffusive spread of the wake.

In practice, it might be rather difficult to make such measurements but it is certainly worthy of investigation. In practice, a parallel wire probe would have to be calibrated in a steady stream so that a conventional velocity calibration could first be obtained. Then a series of yaw calibrations would have to be carried out at different velocities in order to determine the variation of the angular 'window' as a function of velocity. The analysis in appendix A should prove useful in establishing the form of this variation from a small number of yaw calibrations.

The main practical difficulty in a highly turbulent flow might be the very large number of samples that may be involved in obtaining reasonable estimates of the complete joint probability distribution. Due to the time constants of the wires, samples cannot be obtained at a rate greater than about 100 samples per second and, without doing any calculations, the author's intuition is that something like a 100,000 samples might be needed at twenty or thirty angles in order to obtain a reasonable estimate of the probability distribution. This would take something of the order of an hour of sampling for each spatial point in the flow. However, this is not entirely unreasonable and it would provide for the first time important information about the higher order cross-

products in a highly turbulent flow. Such information would no doubt provide useful data for turbulence modellers!

5.0 Concluding remarks.

This paper has reviewed briefly the various forms of pulsed wire technique that have so far been developed. It has been shown that the crossed wire technique can be used to make velocity and turbulence measurements in highly turbulent flows without any upper restriction on turbulence level and that these measurements can be extended to near wall regions as well. In addition, the parallel wire wall shear stress probe has been discussed and it has again been shown that wall shear stress measurements can be made without any upper restriction on the turbulence levels. The limitations of both the crossed wire probe and the wall shear stress probe have been discussed and a number of suggestions for improving both of them have been made.

Finally, some comments have been made on the potential of a parallel wire probe for use in highly turbulent flows that would enable higher order velocity cross-product terms to be measured. However, a programme of experiments is required to establish if this potential can be realised or not.

REFERENCES.

Almeida, H.M.D.S. 1986 Study of the Interaction of a Jet and a Uniform Stream using Pulsed Wire Anemometry. Ph.D.thesis. Aeronautics Department, Imperial College.

Bauer, A.B. 1965 Direct measurements of velocity by hot wire anemometry. AIAA J.,3,1189-1191.

Bradbury,L.J.S. Castro, I.P. 1971 A Pulsed Wire Technique for Turbulence Measurements. J. Fluid Mech., 49, 657-691

Bradbury, L.J.S. Ginder, R.B. 1973 A Preliminary Investigation of a Pulsed Gauge Technique for Skin Friction Measurement in Highly Turbulent Flow. Aeronautical Research Council paper FM4394, U.K.

Bradbury, L.J.S. 1976 Measurements with a Pulsed Wire and a Hot Wire Anemometer in the Highly Turbulent Wake of a Normal Flat Plate. J. Fluid Mech., 77, 473-497.

Castro, I.P. 1992 Pulsed Wire Anemometry.

Experimental Thermal and Fluid Science, 770-780. Elsevier Science Publishing Co.

Castro, I.P. Cheun, B.S. 1982. The Measurement of Reynolds Stresses with a Pulsed Wire Anemometer. J. Fluid Mech., 118, 41-58.

Castro, I.P. Dianat, M. 1990. Pulsed Wire Anemometry near Walls. Experiments in fluids, 8, 343-352.

Castro, I.P. Dianat, M. Bradbury, L.J.S. 1987. The Pulsed Wire Skin-Friction Measurement Technique. Turbulent Shear Flows Vol.5, 278-290. Ed.J.C.Andre et al. Springer, New York

Devenport, W.J. Evans, G.P. Sutton, E.P. 1990 A Traversing Pulsed Wire Probe for Velocity Measurement near a Wall. Experiments in Fluids, 8, 336-342

Gaster, M. 1968 Private communication.

Ginder, R.B. 1971 The Development of a Device to Measure Skin Friction in Highly Turbulent Flow. Ph.D.thesis, Aeronatics Dept., Imperial College.

Hall, D.J. 1979 Wind Tunnel Modelling of Heavy Gas Spills. Rep.LR432. Warren Spring Laboratory, Stevenage, U.K.

Ruderich, R. Fernholz, H.H. 1986 An Experimental Investigation of a Turbulent Shear Flow with Separation, Reverse Flow, and Reattachment. J. Fluid Mech., 163, 283-322.

Watts, N. 1982 Practical Road Vehicle Aerodynamics. Aerospace, 9, 12-14.

White, D.B. Escudier, M.P. Gavignet, A. 1987 Flow Patterns under a Rock Bit. Drilling and Pumping Journal - December no.4 21-34. Schlumberger Cambridge Research publication.

APPENDIX A.

THE RESPONSE OF A PULSED PARALLEL WIRE PROBE.

Ignoring the effects of longitudinal diffusion, the temperature distribution in the wake of a pulsed wire is given by

$$\frac{\theta(x,y,t)}{\theta_{pi}} = \frac{N_p}{2}\left(\frac{\pi}{P}\right)^{1/2} e^{-\frac{t-x/U}{T_p}} e^{-\frac{P}{4}\left(\frac{y}{x}\right)^2} H\left(\frac{x}{U}\right) \qquad (1A)$$

where $\theta(x,y,t)$ is the temperature in the wake of the pulsed wire, θ_{pi} is the temperature of the pulsed after the voltage impulse. N_p is the Nusselt number for heat transfer from the pulsed wire. T_p is the pulsed wire time constant. $P = Ux/\kappa$ is the Peclet number and $H(x/U)$ is a Heaviside step function at time $t = x/U$.

If a sensor wire is placed in this wake at position x, y, its temperature $\theta_s(t)$ is given by

$$\theta_s(t) = \frac{e^{-\frac{t}{T_s}}}{T_s}\int_0^t \theta(x,y,t)\, e^{\frac{t}{T_s}}\, dt \qquad (2A)$$

where T_s is the sensor wire time constant. Using equation (1A) in (2A) gives

$$\theta_s(t) = \frac{N_p}{2}\left(\frac{\pi}{P}\right)^{1/2} \frac{T_p}{T_p - T_s}\left(e^{-\frac{t-x/U}{T_p}} - e^{-\frac{t-x/U}{T_s}}\right) e^{-\frac{P}{4}\left(\frac{y}{x}\right)^2} H\left(\frac{x}{U}\right) \qquad (3A)$$

In the practical circuit, the sensor wire is differentiated with respect to time and it is this differential signal that is used to trigger the time-of-flight counter. This differential signal has a step-like behaviour at $t = x/U$ with an amplitude given by

$$\left(\frac{d\theta_s}{dt}\right)_{t=x/U} = \frac{N_p}{2}\left(\frac{\pi}{P}\right)^{1/2} \frac{e^{-\frac{P}{4}\left(\frac{y}{x}\right)^2}}{T_s} \qquad (4A)$$

If we assume for simplicity that Nusselt number varies like the square root of the Reynolds number, we find that

$$\left(\frac{d\theta_s}{dt}\right)_{t=x/U} \propto U^{1/2}\, e^{\frac{P}{4}\left(\frac{y}{x}\right)^2} \qquad (5A)$$

using the expression for the time constants given by Bradbury and Castro (1971). The angular window of the probe is defined by that value of y/x at which the amplitude of the differentiated signal falls below the trigger level. It can be shown from equation (5A) that this window narrows with increasing velocity. This is simply due to the narrowing of the wake as lateral diffusion diminishes with increasing velocity. There is a counter effect from the other terms in the equation for the differentiated signal but the overall effect is still to produce a narrowing of the 'window'.

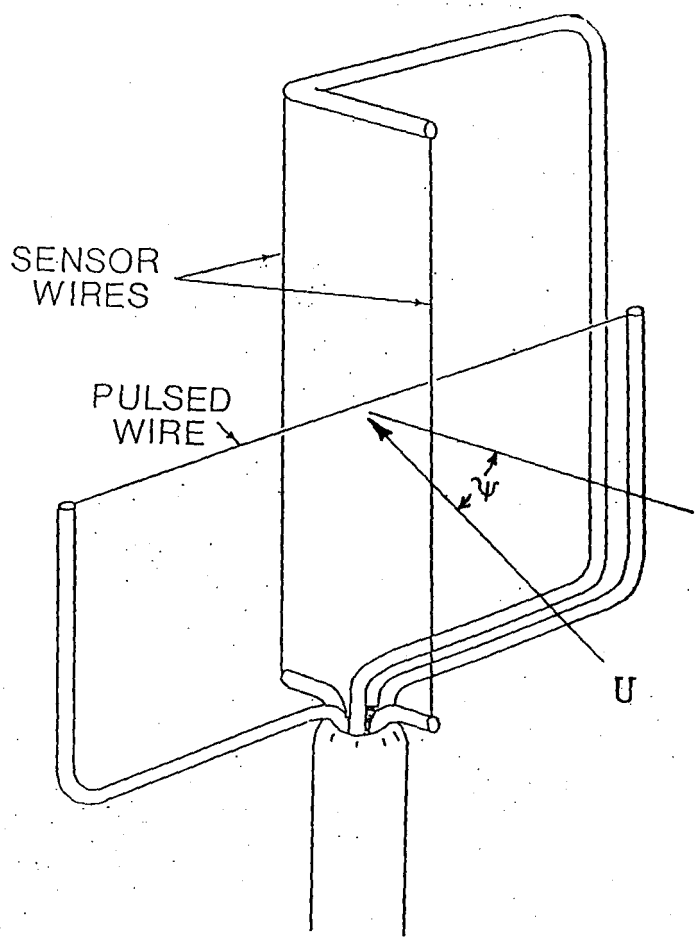

FIG. 1 SKETCH OF THE PULSED WIRE PROBE.

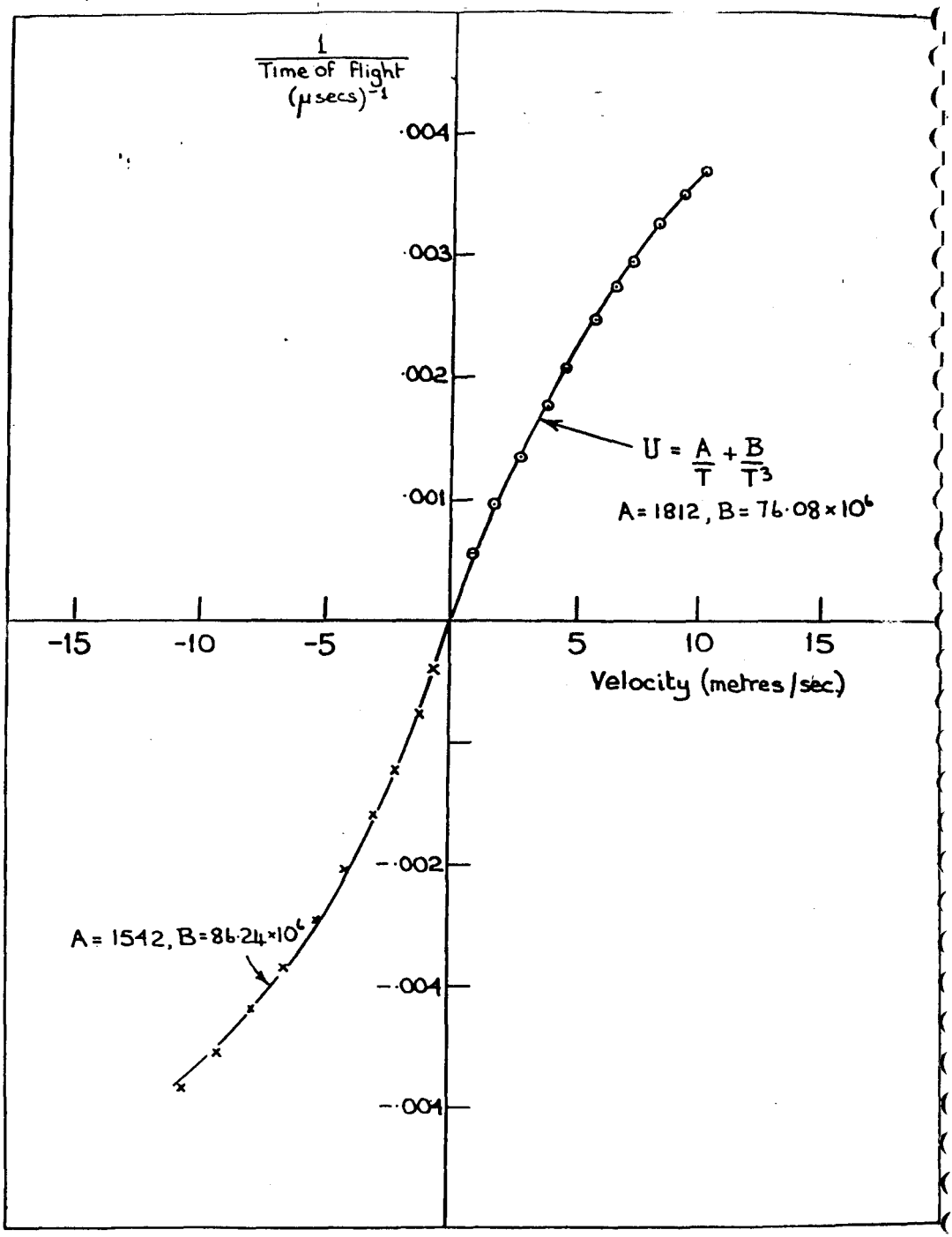

FIG. 2 A PULSED WIRE ANEMOMETER CALIBRATION.

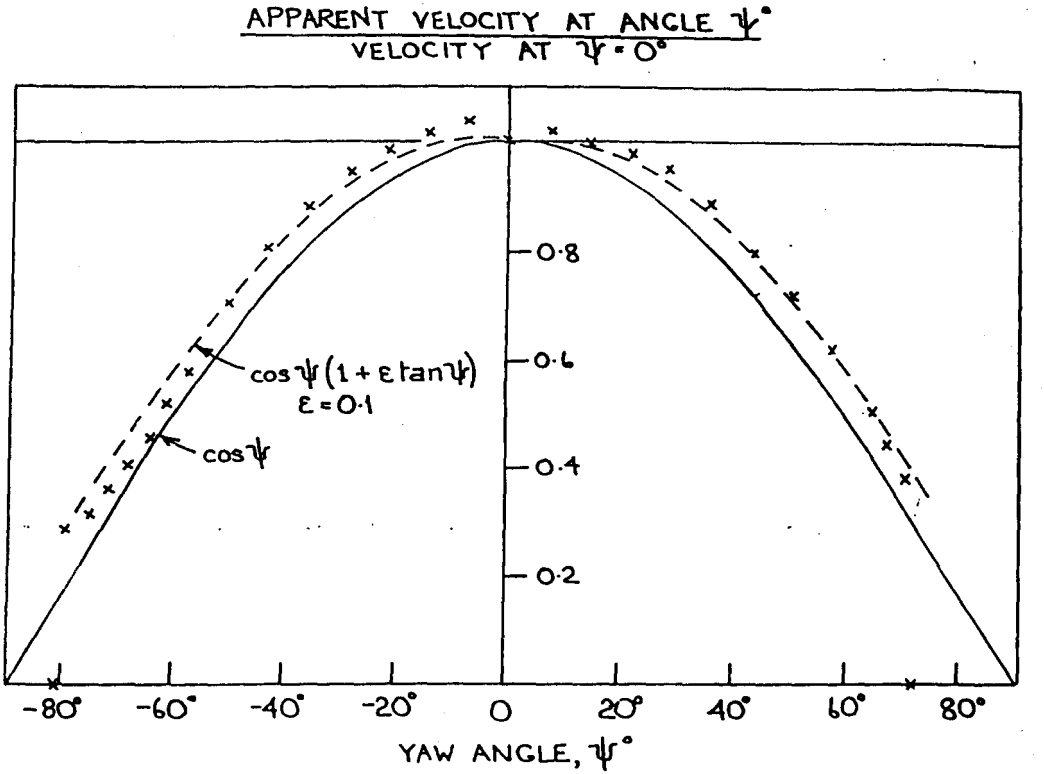

FIG. 3 YAW RESPONSE OF A PULSED WIRE ANEMOMETER.

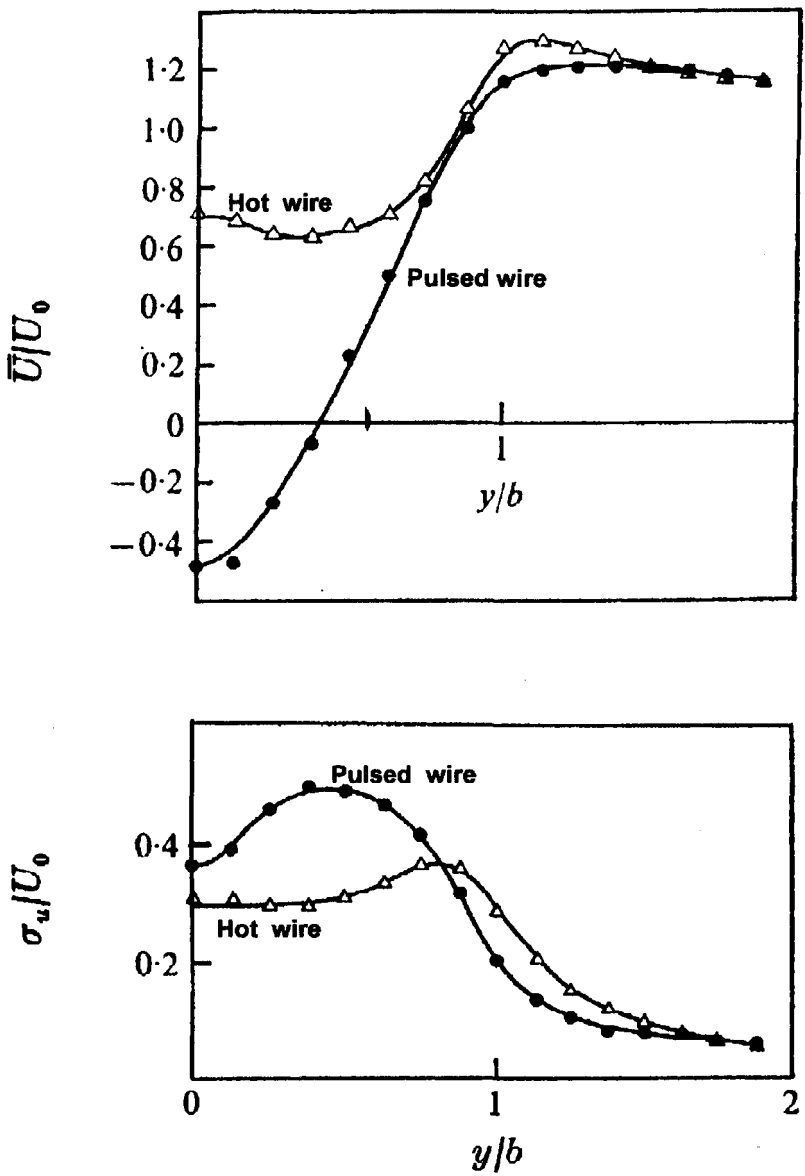

Fig.4 Mean and turbulent intensity profiles downstream of a normal flat plate - 1 plate width downstream.

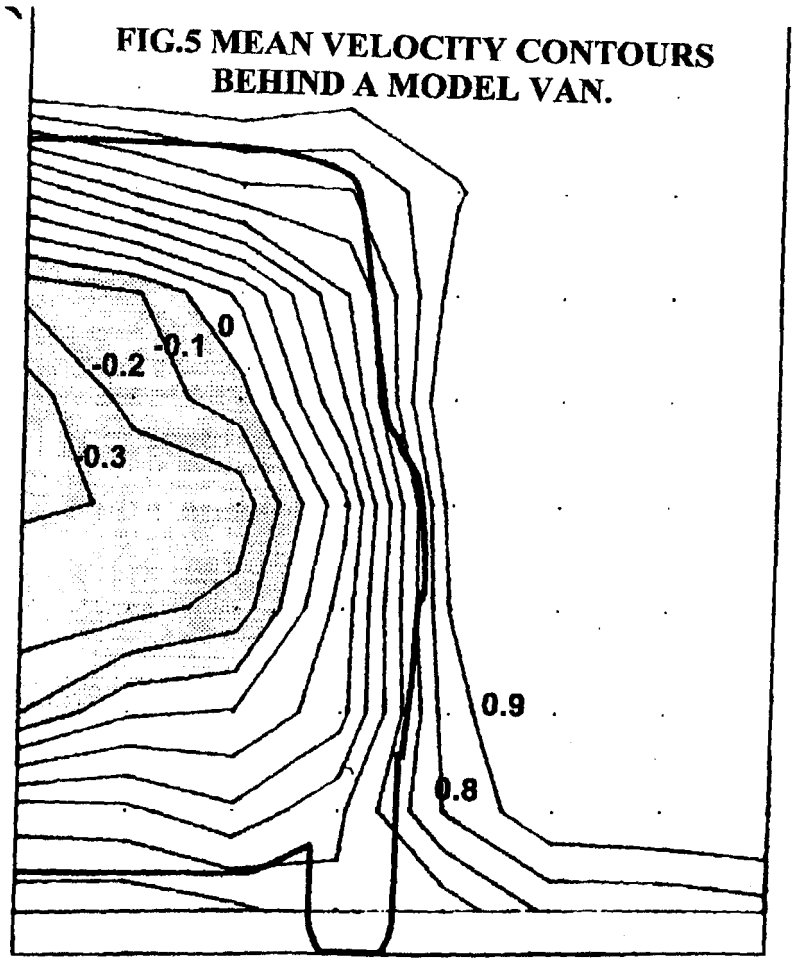

FIG.5 MEAN VELOCITY CONTOURS BEHIND A MODEL VAN.

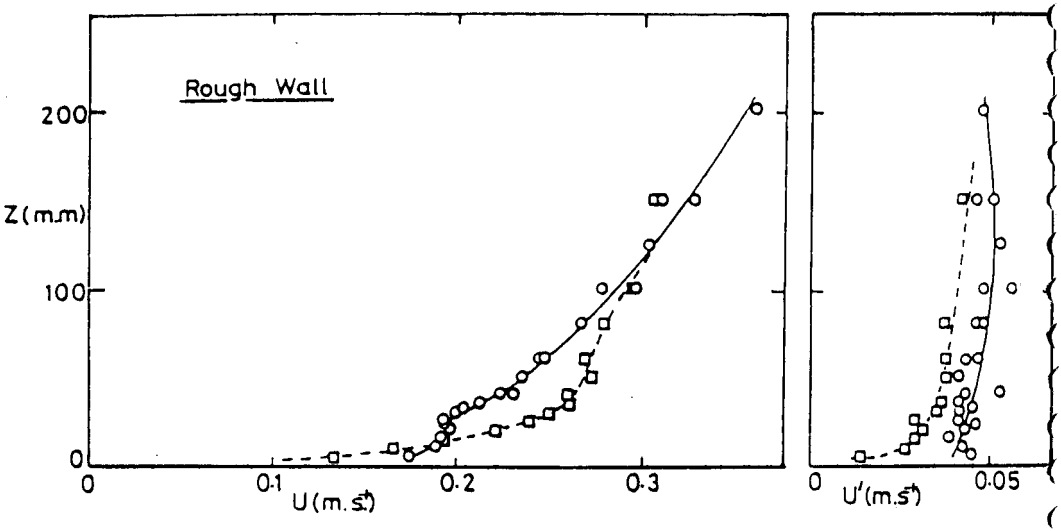

Fig.6 Mean and fluctuating velocity profiles through a continuous-release heavy gas cloud and through the undisturbed boundary layer at the same point.
Gas density=5.74xAir
Release rate=3000 cu cm/min
(○) - No gas plume
(□) - Gas plume

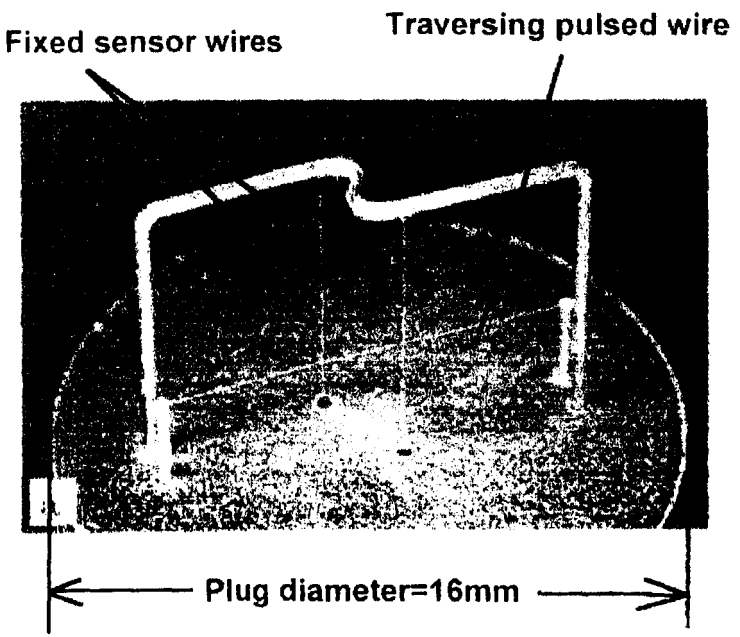

Fig.7 Crossed wire probe for near wall measurements.

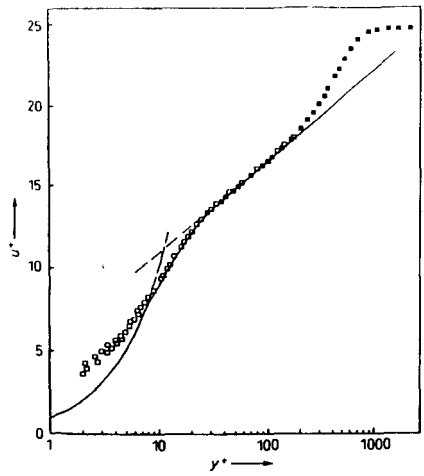

Fig.8 Turbulent boundary layer profile- $C_f \approx 0.0032$
(■) - Hot wire.
(□) - Pulsed wire (uncorrected)

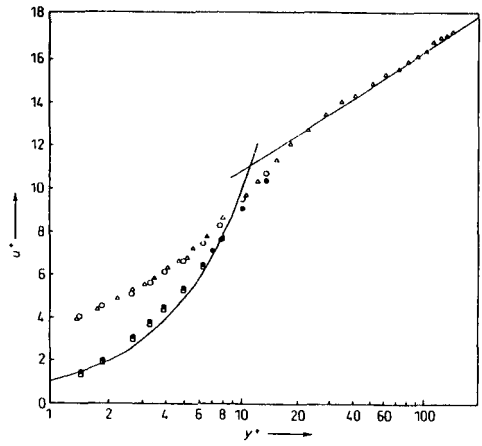

Fig.9 Turbulent boundary layer profile.
(△, ○) - Pulsed wire (uncorrected)
(□, ●) - Pulsed wire (corrected)

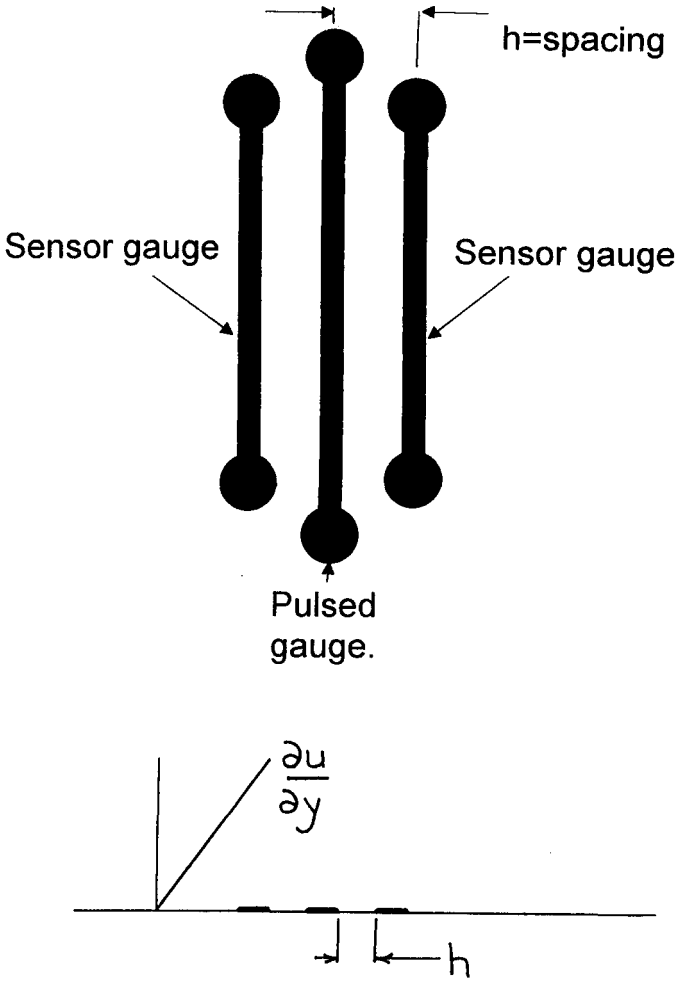

Fig.10 Sketch of a surface mounted pulsed thin film gauge for wall shear stress measurement.

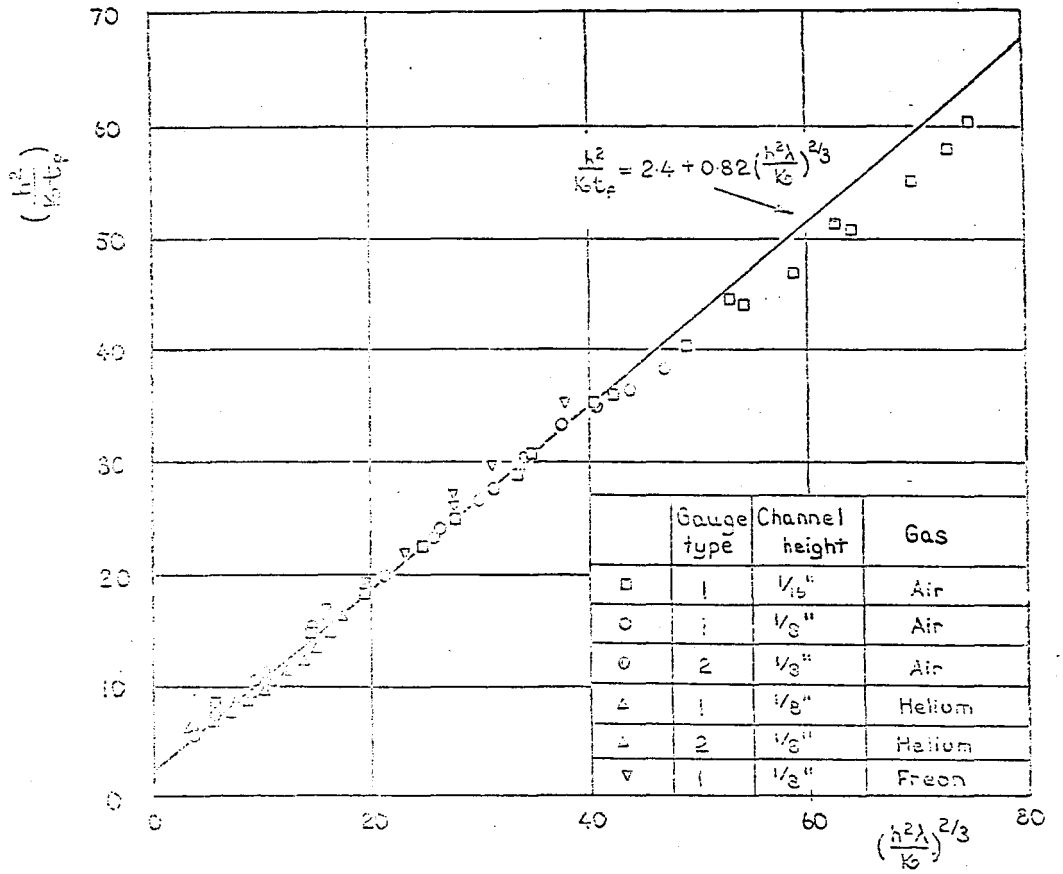

Fig 20 : Laminar calibration — $\left(\frac{h^2}{K t_f}\right)$ against $\left(\frac{h^2\lambda}{K_g}\right)^{2/3}$

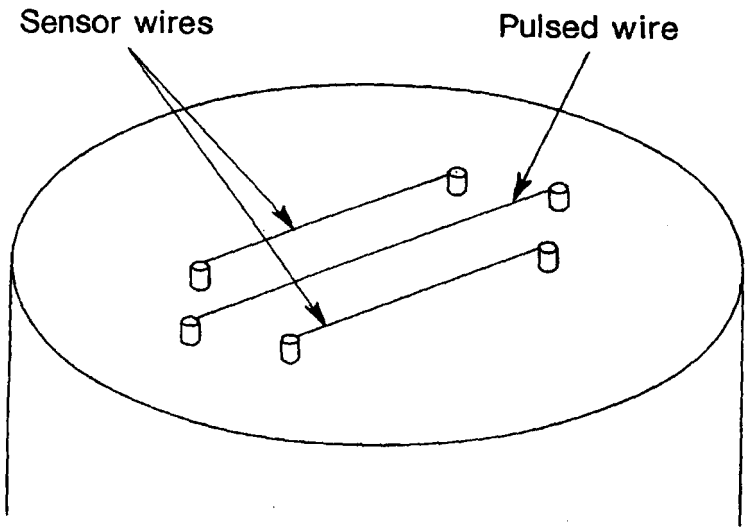

Fig.11 Sketch of a parallel wire wall shear stress gauge.

(Wire lengths approximately 3 mm)
(Height above wall approximately 50 micron.)

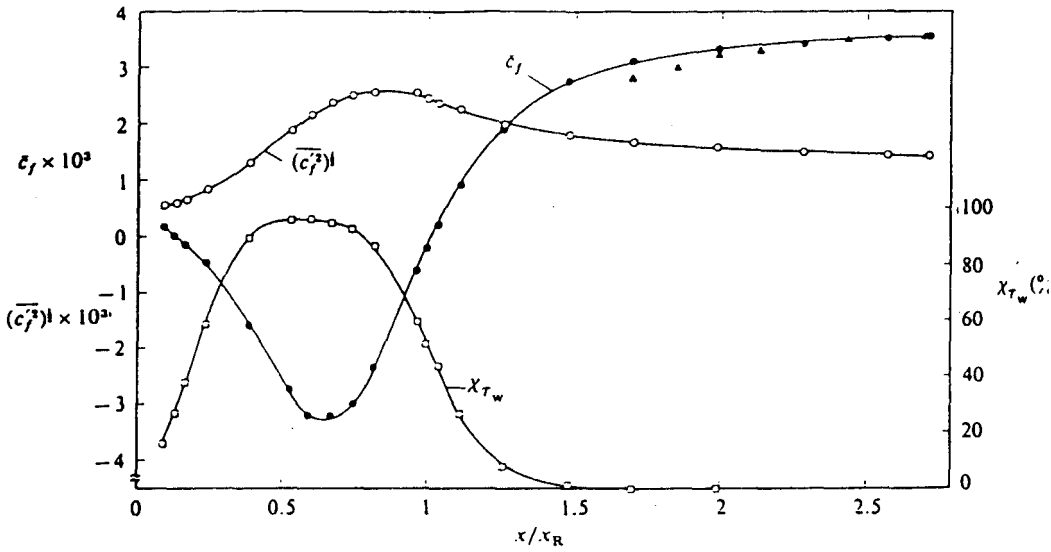

Fig.12 Mean skin friction, skin-friction intensity and skin friction reverse-flow parameter along a splitter plate downstream of a normal flat plate.

(▲) - Preston tube. X_R is length of reverse flow region.

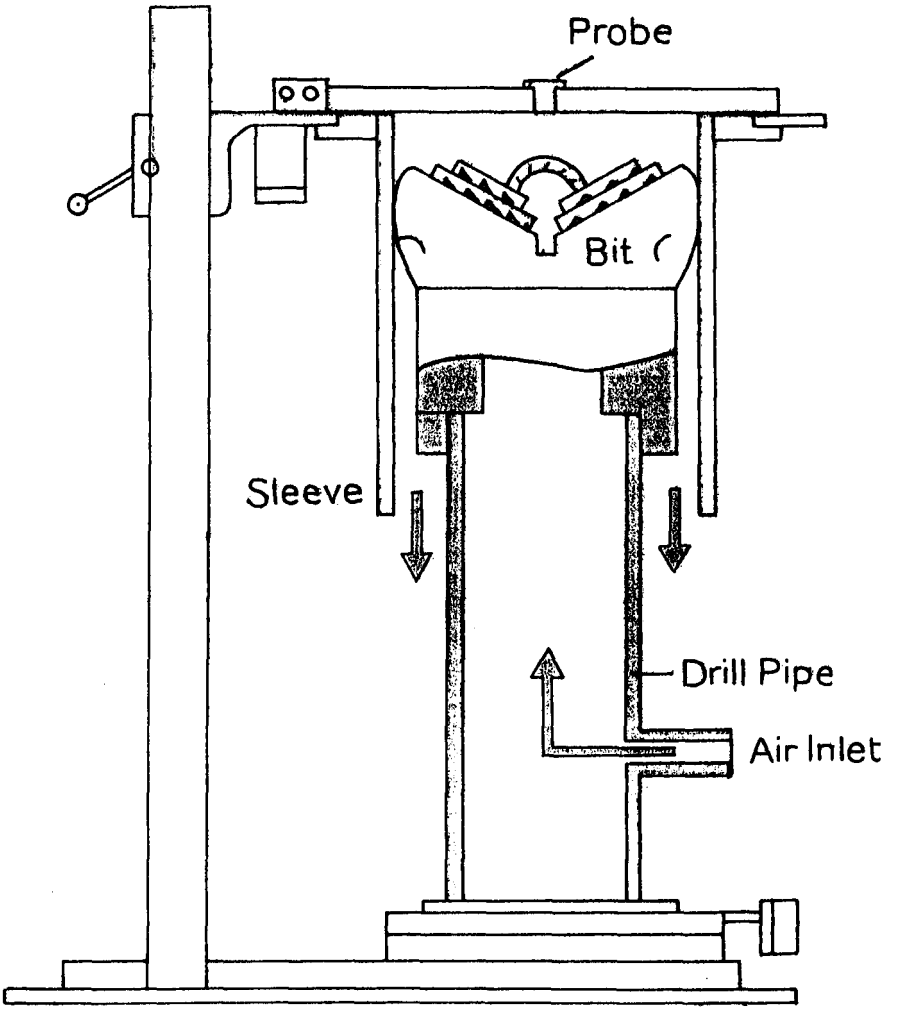

Fig.13 Tri-cone drilling bit test rig.

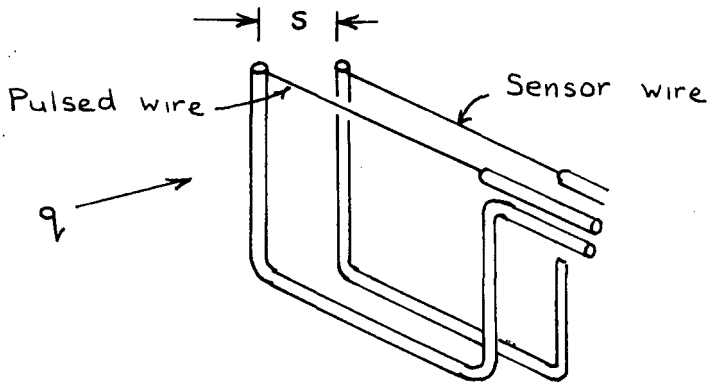

Fig.15 Sketch of a parallel wire probe.

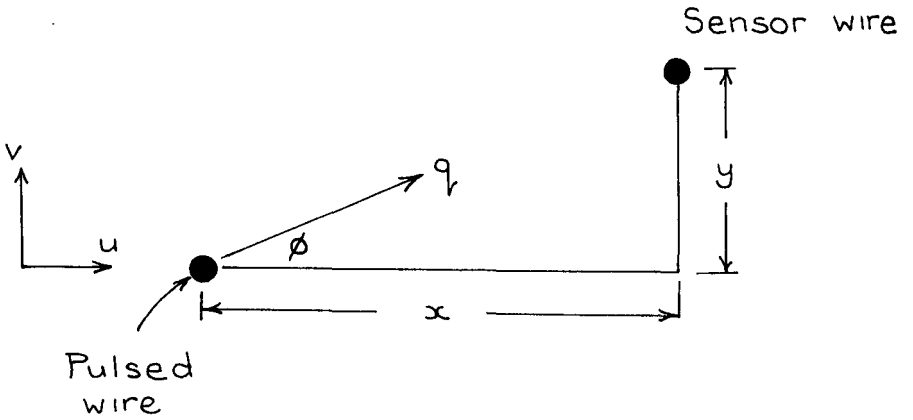

Fig.16 A parallel wire probe in a turbulent flow.

Interaction Entre Deux Panaches Turbulents d'un mélange Gaz-Liquide

Philippe P. M. Menut, Antonio E. dos Santos Ferreira & Jader R. Barbosa Jr.[†]

Programa de Engenharia Mecânica (PEM/COPPE/UFRJ),
C.P. 68503, 21945-970 – Rio de Janeiro – Brasil.
[†] Adresse actuelle: Department of Chemical Engineering, Imperial College of Science, Technology and Medecine,
Prince Consort Road, London – SW7 2BY – England – UK.

Résumé

Ce travail expérimental décrit la distribution de fraction locale de gaz dans un écoulement bi-phasique Gaz-Liquide obtenu par deux panaches de bulles de gaz adjacents. Les mesures de fraction locale de gaz sont réalisées par une sonde électro-résistive accouplée à un module conditionneur de signal. Le système comprend un réservoir d'eau cubique de $1m^3$ et des injecteurs d'air dont le débit peut varier entre 0.6 et 3.5 litres par minute. Si le numéro de Froude basé sur la demi distance entre les deux sources de gaz est élevé, les panaches présentent une déflection de leur axe par action de l'effet Coanda. Une brève analyse théorique basée sur l'hypothèse de Taylor est conduite afin de proposer un coefficient d'entrainement variable. Les distributions Gaussiennes existant pour les panaches uniques axisymmétriques ne sont plus valables si l'effet Coanda déflechit les panaches de bulle. Des photographies illustrent le phénomène pour diverses configurations d'ecoulement.

Mots Clefs:

Panaches de bulles, distribution de fraction de gaz, sonde électro-résistive, effet Coanda, coeficient d'entrainement.

I INTRODUCTION

Les mélanges tridimensionnels complexes en écoulements multi-phasiques sont très fréquemment rencontrés dans les procédés de production d'énergie ou dans les industries métalurgiques. Parmi les applications industrielles, l'agitation de métal liquide par injection de panaches de bulles de gaz constitue une phase décisive dans l'industrie métalurgique. Le mouvement vertical d'un gaz inerte provoque une forte agitation du métal liquide, résultant en une homogénéisation chimique et thermique du mélange, mais aussi en un regroupement d'inclusions non-métalliques dans une couche superficielle.

La qualité de l'homogénéisation dépend de la géométrie de l'installation et surtout de la manière dont le gaz est injecté. Le nombre d'injecteurs, leur position et leur débit influent fortement sur le degré d'agitation réalisé et, par conséquence, sur les propriétés de l'écoulement induit: temps de mélange, période de résidence et suppression des inclusions.

Les études rencontrées dans la littérature considèrent en général une seule source de gaz, supposée axissymétique. Il s'agit, en fait, d'une simplification obligatoire si une méthode intégrale est employée et si l'hypothèse d'entrainement est admise. En approche différentielle, des modèles de turbulence relativement généraux devraient être capables de détecter des assymétries de l'écoulement, et plusieurs sources de gaz pourraient alors être envisagées. Cependant, comme nous allons le voir, il en est autrement.

L'objectif de ce travail est de réaliser une étude expérimentale de la distribution de la concentration de gaz dans un écoulement produit par deux panaches ronds colatéraux. Ces panaches,

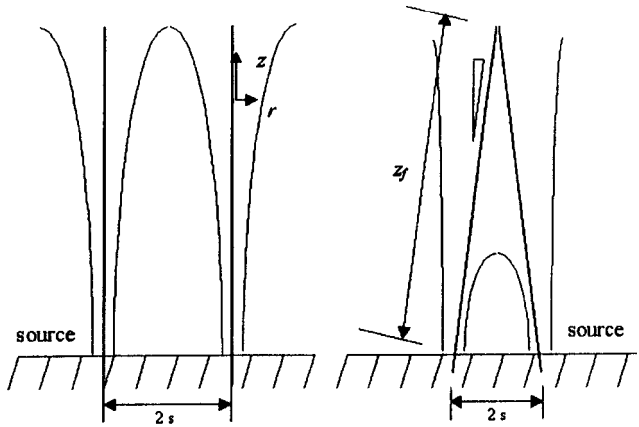

Figure 1: Deux sources circulaires de gaz (a) sans interaction et (b) avec inclinaison des panaches.

constitués d'un mélange de bulles de gaz et de liquide, s'attirent mutuellement et perdent leur caractère axisymmétrique. Après avoir étudié l'interaction d'un panache avec une paroi verticale (Menut et al., 1998), nous nous intéressons ici à l'influence de l'effet Coanda sur deux panaches adjacents. Cette configuration possède un nouveau degré de liberté: les deux panaches peuvent tourner sur un plan horizontal et quitter le plan vertical d'investigation. Cette rotation générale rend la campagne de mesure expérimentale plus difficile. Cependant, comme nous allons le détailler plus en avant, cette difficulté est contournée en réalisant une moyenne des mesures sur une période bien plus étendue que dans le cas d'un seul panache adjacent à un mur. Notons enfin que la configuration étudiée ici relève d'un grand intérêt dans l'industrie métalurgique.

La figure 1 présente la forme générale d'un écoulement à deux panaches de bulles d'air. La figure 1a montre le cas de deux sources suffisament éloignées pour ne pas interagir entre elles, tandis que la figure 1b montre l'influence d'une source sur l'autre et la conséquente déflection des panaches de leur ligne centrale initiale.

Le panache axisymmétrique est un écoulement largement étudié ces trois dernières décades, tant d'un point de vue théorique (Ditmars and Cederwall, 1974; Milgram, 1983; Brevik and Killie, 1996) que d'un point de vue expérimental (Milgram, 1983; Castillejos and Brimacombe, 1987a; Barbosa and Bradbury, 1996). Ces différents travaux ont couvert une large bande de conditions expérimentales, et n'ont cependant pas proposé de modèle unifié capable de simuler toutes ces conditions. En approche intégrale, l'écoulement a été divisé en trois régions distinctes régies par des effets dominants différents (Milgram, 1983). La région dominée par les effets de flottabilité est communément appelée "Zone d'écoulement établit". Il s'agit de la région étudiée ici.

La bibliographie traitant de plusieurs panaches est bien plus pauvre. Un travail relativement complet sur deux panaches adjacents a été recement publié (Joo and Guthrie, 1992). L'écoulement bi-phasique a été étudié expérimentalement à l'aide de la technique du traceur. Les auteurs quantifient le temps de mélange total qui, par définition, correspond à l'intervalle de temps nécessaire pour que 95 % des traceurs soient mélangés au liquide. Ils ont comparé les résultats de plusieurs conditions différentes avec des résultats de simulation numérique. Le code implémenté est basé sur le modèle κ-ϵ et l'action des bulles de gaz limitée aux termes de flottabilité. Les résultats numériques n'ont montré aucune inclinaison des panaches, quelque soit la configuration expérimentale. Des photos de l'expérience montrent, cependant clairement une déflection des

panaches. La simplicité du modèle numérique pour la phase gazeuse n'a pas permis de prendre en compte l'interaction entre les deux panaches. Les auteurs ont en fait simulé deux panaches ronds juxtaposés et indépendants.

Pera et Gebhart (1975) ont étudié l'interaction entre deux jets thermiques laminaires utilisant un interféromètre Mach-Zehnder. Ils ont développé un modèle simplifié afin de prendre en compte la déflection angulaire de l'axe central des jets. Pera et Gebhart ont noté que les jets plans subissent une inclinaison plus forte que les jets ronds. Nous avons cependant opté pour une configuration tridimensionnelle de panaches ronds afin de représenter de manière plus exacte les conditions industrielles rencontrées dans les bains d'acier liquide.

L'effet Coanda est, selon Reba (1966) , la tendance d'un fluide, gazeux ou liquide, à adhérer à une paroi proche de l'orifice qui injecte le fluide.

Il peut être vérifié expérimentalement que lorsque deux sources de flottabilité (ou de quantité de mouvement) sont juxtaposées, les deux panaches (ou jets) turbulents résultants ont tendance à se rapprocher l'un de l'autre. La courbure subie par les panaches n'est pas due, contrairement au cas des panaches laminaires (Pera and Gebhart, 1975), à une différence de pression. Si l'écoulement est turbulent, la déviation des panaches est due à une restriction de l'entrainement de fluide externe par l'écoulement moyen. En condition axisymmétrique, l'influence de la différence de pression est faible comparée à celle de l'entrainement turbulent. Bien que les types de force qui gouvernent chacun de ces phénomènes soient différents, certains auteurs considèrent les deux cas comme exemples de l'effet Coanda (Tritton, 1988).

Dans ce présent travail, les auteurs sugèrent que l'inclinaison des panaches ronds turbulents provient d'un déséquilibre du flux de quantité de mouvement lié à la restriction d'entrainement. Cette restriction est elle-même due à la présence du panache adjacent.

II ÉTUDE ANALYTIQUE

L'analyse qui suit a pour but d'expliciter les bases de l'hypothèse d'entrainement de Taylor (Morton et al., 1956) et d'établir les termes contenant l'influence de l'inclinaison des panaches à travers la variation locale du coefficient d'entrainement.

L'hypothèse d'entrainement a été proposée en premier lieu par Taylor en 1949 dans des notes non publiées. Plus tard, en 1956, Morton *et al.* présentent un travail en formulant cette hypothèse lors d'une conférence. Les auteurs, dans cet article, énoncent d'une manière simple:

"the rate of entrainment at the edge of the plume or cloud is proportional to some characteristic velocity at that height".

En d'autres termes, la vitesse moyenne v de la phase liquide traversant une section d'un écoulement turbulent est proportionelle à la vitesse locale maximum – ou vitesse moyenne – de la section. En termes de débit volumétrique, Q, on peut écrire

$$dQ = vdA = \alpha u_0 b d\theta dz \tag{1}$$

avec α le coefficient d'entrainement , u_0 la vitesse moyenne maximale de la phase liquide (sur l'axe du panache) et b le rayon du panache. Pour les panaches thermiques et les jets en géométrie axisymmétrique, les coefficients d'entrainement sont constants et ont pour valeurs respectives 0.083 et 0.054.

Les théories intégrales appliquées aux panaches de bulles sont basées sur une analogie avec les panaches thermiques. La théorie considère, en plus d'une nouvelle équation pour la seconde phase, un coefficient d'entrainement variable mais aussi un paramètre appelé paramètre d'amplification de quantité de mouvement (Milgram, 1983). Ces paramètres ont pour objectif de prendre en

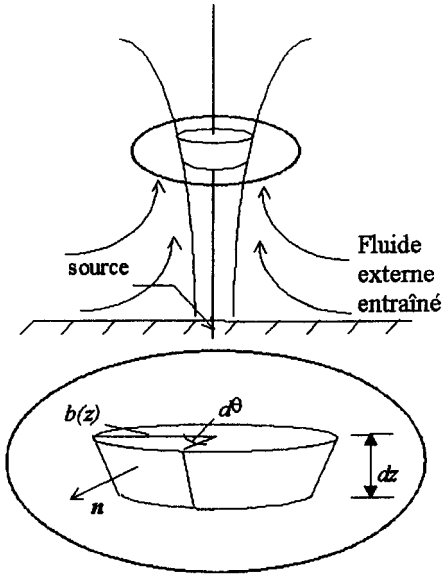

Figure 2: L'effet d'entrainement en geometrie axisymmétrique.

considération l'action des bulles sur la phase liquide. Les théories actuelles sont valides pour les panaches de bulles tant pour les petites échelles que pour les grandes échelles.

Dans cette analyse, la déflection de l'axe du panache est supposée provenir d'une restriction de l'entrainement due à la présence du panache voisin. Par conséquence, le coefficient d'entrainement dépend de la coordonnée angulaire θ et de la hauteur z.

L'angle de déflection du panache, ϕ, est défini géométriquement par (figure 1.b) $\sin\phi = s/z_f$. Santos et Silva Freire (1993) sugèrent que $\sin\phi$ est aussi égal au rapport entre la force qui doit être exercée pour incliner le panache et le moment moyenné sur la coordonnée z,

$$\begin{aligned} \sin\phi &= \frac{F}{\frac{1}{z_f}\int_0^{z_f} M(z)\,dz}, \\ &= \frac{\int_0^{z_f}\int_0^{2\pi} \rho_l\,\alpha^2\,u_0^2\,b\,d\theta dz}{\frac{1}{z_f}\int_0^{z_f}\int_0^{\infty} 2\pi\,\rho_l\,(1-c)\,u_l^2\,r\,dr dz}, \end{aligned} \tag{2}$$

avec ρ_l la densité de la phase liquide, $c = c(r,z)$ la distribution de fraction de gaz et $u_l = u_l(r,z)$ le profil de vitesse de la phase liquide.

L'équation 2 établit une relation pour l'évaluation du coefficient d'entrainement si les autres inconnues, ϕ, u_0 et b, sont déterminés expérimentalement.

Notons cependant qu'il est important de déterminer le type de dépendence fonctionnelle de α sur les autres paramètres de l'écoulement. Une analyse dimensionnelle fournit les paramètres suivants:

$$\phi = f\left[\frac{q^2}{g\,s^5}, \frac{\Delta\rho\,q^2}{\sigma\,s^3}\right] \tag{3}$$

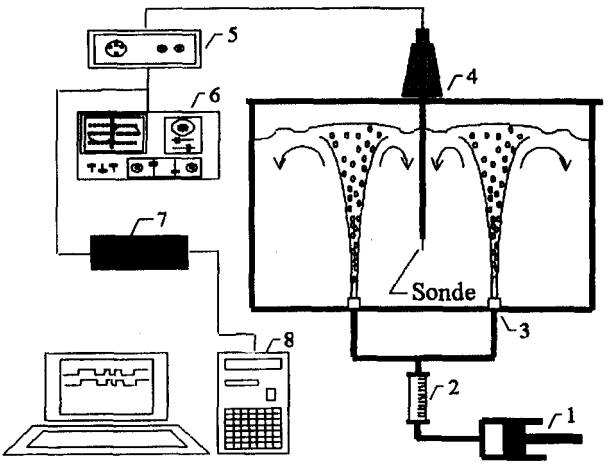

COMPOSANTS

1. Compresseur à air
2. Débimètre
3. Injecteurs
4. Positionneur 2D
5. Module conditionneur
6. Oscilloscope
7. Carte interface
8. Micro-ordinateur

Figure 3: Installation expérimentale.

avec g l'accélération de la pesanteur, q le débit de gaz de chaque source, σ la tension superficielle et $\Delta\rho$ la différence de densité entre les deux phases. Les quantités entre crochets sont, respectivement, le numéro de Froude modifié, F_r, et le numéro de Weber modifié, W_e, basés sur la demi distance entre les deux sources.

III CONFIGURATION EXPÉRIMENTALE

Les propriétés de l'écoulement ont été mesurées à l'aide d'une sonde électro-résistive. Ce type de sonde, réalisé à partir de fines aiguilles, a été développé simultanément par Neal et Bankoff (1963) et par Nassos (1963) . Ces études préliminaires sont spécialement dédicacées à la présentation de la technique expérimentale plutôt qu'à une étude profonde de l'écoulement. Neal et Bankoff ont travaillé dans un mélange Nitrogène–Mercure, tandis que Nassos a utilisé un mélange air–eau. Serizawa *et al.* (1975a, 1975b, 1975c) et Herringe et Davis (1976) ont contribué de manière significative à la compréhension de la structure turbulente des écoulements internes bi-phasiques. Chesters *et al.* (1980) furent les premiers à utiliser avec succès des sondes électro-résistives en milieu non confiné. Ils ont combiné ces résultats à des mesures d'anémométrie laser-Doppler (ALD) afin de décrire les caractéristiques des phases liquides et gazeuses dans un panache de bulles. Tacke *et al.* (1985) ont utilisé des sondes électro-résistives dans des mélanges air-eau, Hélium-eau et Nitrogène-Mercure afin d'étudier le procédé de fabrication de l'acier par mélange de gaz. Castillejos et Brimacombe (1987a, 1987b) , pour une application industrielle identique, ont développé une instrumentation complète basée sur cette technique. En 1988, Teyssedou *et al.* ont présenté un nouveau système AC ainsi qu'une analyse de l'effet de la géométrie de la sonde et d'autres paramètres sur les performances de l'instrumentation. Plus récemment, Kocamustafaogullari et Wang (1991) , Leung *et al.* (1992) et Liu et Bankoff (1973) ont utilisé ce type de sondes afin de déterminer la fraction moyenne locale de gaz, la vitesse et la longueur percée des bulles en écoulement interne. Mazumdar et Guthrie (1995) ont publié une récente révision sur le procédé de fabrication de l'acier par mélange de gaz. Smith et Milelli (1998) ont présenté une analyse numérique d'un panache confiné et réalisé une comparaison avec des résultats expérimentaux.

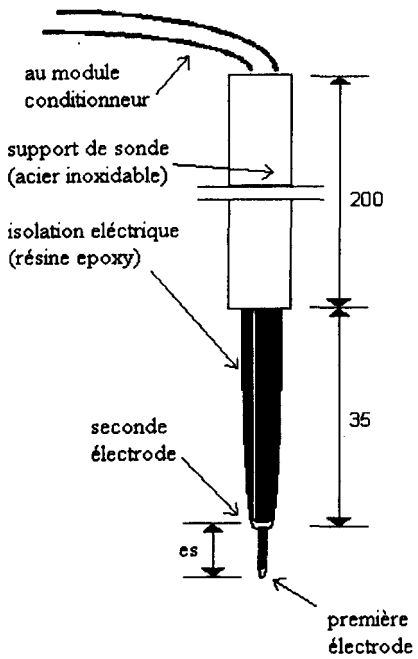

Figure 4: Sonde électro-résistive (valeurs en mm).

Enfin, Sun *et al.* (1998) ont mesuré les caractéristiques d'un panache de bulles d'air. Les deux derniers ont combiné des mesures par sonde électro-résistive et par anémométrie laser-Doppler.

Le principe de la technique électro-résistive est de reconnaître la phase entourant la sonde en comparant sa conductivité avec une valeur de référence. Un circuit électronique associé à la sonde réagit par une brusque variation de tension lors du passage d'une interface. Pour de plus amples renseignements techniques, le lecteur est invité à lire la publication de Barbosa et Bradbury (1996),

L'installation expérimentale est présentée à la figure reffig:instal. Elle comprend un réservoir d'eau, un système d'injection d'air, un positionneur 2D et un système d'acquisition et d'analyse de données.

Le réservoir vitré mesure 1m x 1m x 1m et contient 300 milligrammes par litre de solution de chloride de sodium (brine). Les deux canaux du système d'injection d'air sont composés de compresseurs à air, d'un débimètre massique et d'un injecteur. L'air est introduit depuis le fond du réservoir par deux injecteurs identiques. Le système d'acquisition et de traitement de données comprend: une sonde électro-résistive double, un module de conditionnement du signal, un oscilloscope, une interface et un micro-ordinateur.

La figure reffig:sonde présente la sonde électro-résistive utilisée; un fin cable d'acier inoxidable de 0.2 mm de diamètre est logé dans un tube hypodermique de caractéristiques 0.4 mm OD 0.2 mm ID. Les deux conducteurs sont électriquement isolés, mutuellement et par rapport à l'extérieur, excepté à leurs extrémités. Les parties non isolées ont une longueur approximative de 0.1 mm. Les deux électrodes sont séparées d'une distance de 1.5 mm.

La sonde est placée en position verticale. La profondeur de l'eau est conservée constante et égale à 0.85 cm. Environ 15 minutes sont nécessaires pour garantir des conditions stationnaires. Les conditions expérimentales réalisées sont répertoriées dans le tableau 1. Les mesures sont réalisées pour différentes distances entre les sources de gaz et pour différents débits de gaz. La sonde est déplacée sur un axe horizontal passant exactement à la verticale des deux sources. les injecteurs ont un diamètre de sortie de 3.2 mm.

Table 1 - Conditions expérimentales.

Test	s [cm]	q [l/min]	F_r	W_e
a	3.25	2.4	4.50 e-3	1.1638
b	6.4	2.4	1.52 e-4	0.1524
c	9.05	2.4	2.69 e-5	0.0539
d	3.25	1.2	1.12 e-3	0.2910
e	6.4	1.2	3.80 e-5	0.0381
f	9.05	1.2	6.72 e-6	0.0135

La fraction de gaz mesurée en un point $c(r, z, t)$ est une moyenne dans le temps obtenue par,

$$c(r, z, t) = \frac{1}{T} \int_0^T I(r, z, t) dt \tag{4}$$

avec T le temsp total de mesure et I la sortie digitale provenant du module conditionneur. Le signal de sortie, I, consiste en une série de pulses correspondant au passage des bulles d'air par la sonde. De plus amples détails concernant le signal de sortie sont disponibles dans le travail de Barbosa et Bradbury, 1996.

La fréquence d'aquisition est fixée à 3.3 kHz. 50 blocs de 10,000 données sont enregistrées pour chaque point de mesure afin de décrire l'écoulement de manière correcte. Les profils de quatre stations verticales, $z = 10, 30, 50, 70cm$, sont obtenues pour chaque configuration (s, q). Entre 40

et 50 points sont nécessaires pour décrire un profil. La calibration du système de mesure, réalisée dans un tube vertical, a montré que la fraction de gaz est obtenue avec une précision de 10%.

IV RESULTATS

La forme moyenne de l'écoulement est présentée figure 4. Les conditions expérimentales sont listées au tableau 1. Les photographies ont été réalisée avec plusieurs temps d'exposition afin d'obtenir différentes perceptions de la structure des panaches de bulles. Les photographies obtenues avec un temps d'exposition élevé montrent clairement la déformation et le format des panaches. Il est interessant de noter que les déflections angulaires sont parfaitement visibles et détectables à l'oeil nu. Lorsque la distance qui sépare les deux sources augmente, les panaches se redressent; les deux panaches se concentrent pour n'en former plus qu'un dans le cas $s = 3.25cm$.

La figure 5 présente les profils de fraction de gaz obtenus à différentes positions verticales. Les profils proches des injecteurs de gaz présentent une forme Gaussienne, concordant avec les résultats de Mazumdar et Guthrie (1995) pour des panaches axisymmétriques. Les autres profils ne proposent pas la même courbure, ils sont déformés par la présence du panache voisin. Les points de fraction de gaz maximale sont aussi définis sur la figure. Des études précédentes ont montré que ces points correspondent aussi aux points de vitesse de phase liquide maximale. Ils seront pris par la suite comme référence pour définir la position de l'axe des panaches.

La déflection des panaches est présentée à la figure 6 pour plusieurs débits de gaz et trois différentes séparations entre les sources. Le graphique est représenté en coordonnées dimensionnelles. Cette figure montre que la plupart des trajectoires peuvent être raisonnablement approchées de manière rectiligne. Lorsque les deux plumes sont fortement écartées, cette tendance est particulièrement marquée.

Pour chaque cas testé, deux angles de déflection sont calculés, un par panache. L'angle ϕ utilisé dans les figures suivantes est la moyenne des deux angles. L'angle de déflection des panaches ainsi défini peut être présenté en fonction du nombre de Froude et du nombre de Weber. Ces graphiques sont représentés à la figure 7. Ils montrent que l'angle de déflection ϕ augmente de manière logarithmique avec F_r et W_e. Ces courbes, similaires à celles obtenues avec un panache proche d'une paroi (Menut, 1998), pourraient être approchées par des droites rectilignes.

L'évolution de l'angle de déflection en fonction de la distance séparant les deux sources et en fonction du débit de gaz est tracée à la figure 8. Les conclusions déduites du panache proche d'une paroi sont ici aussi vérifiées. Aucune tendance générale ne peut être relevée depuis ces graphes, particulièrement ceux de q. A débit constant, les résultats pour s montrent que l'angle de déflection a tendance à diminuer lorsque la distance entre les deux sources augmente. Les figures 7 et 8 montrent clairement la pertinence du choix des paramètres F_r et W_e pour décrire le phénomène.

En résumé, si l'angle de déflection d'un panache peut être établi à l'aide de l'équation (2), alors le coefficient d'entrainement α est une fonction des nombres de Weber et de Froude locaux. La prochaine étape consiste à mesurer les caractéristiques de la phase liquide afin de proposer une corrélation pour α. Ces informations sont obtenues par visualisation et traitement d'image dans une étude en cours de réalisation.

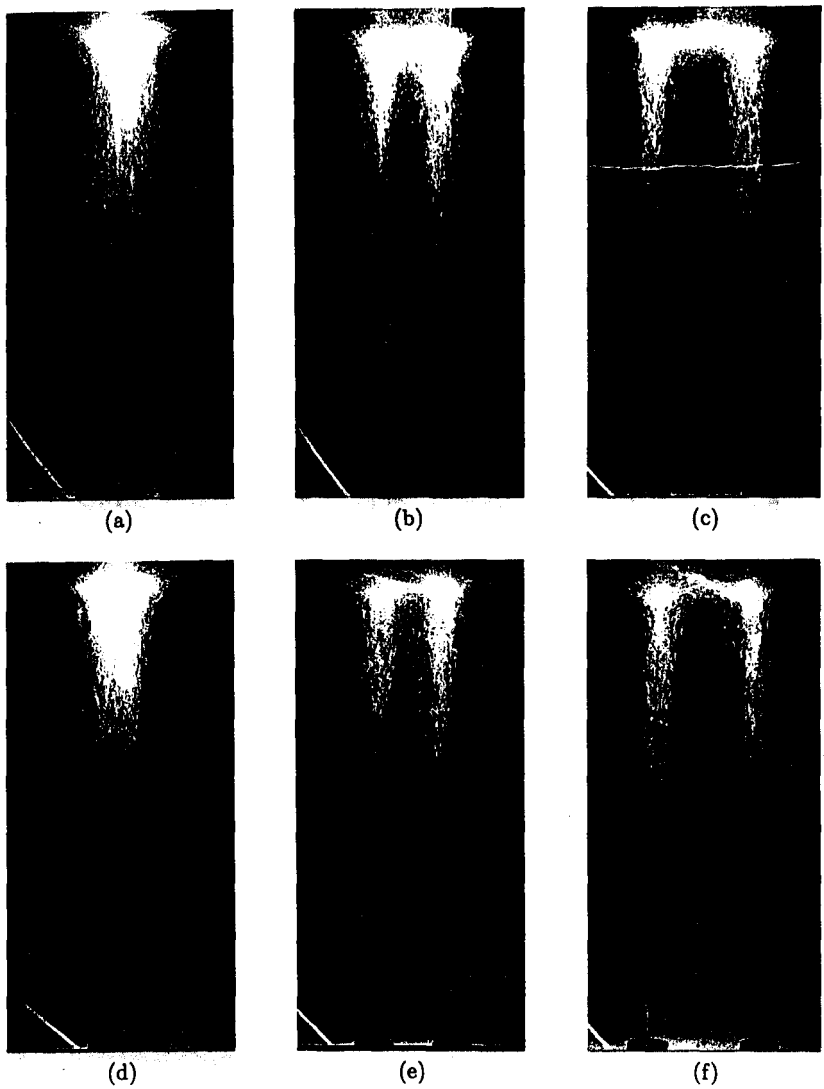

Figure 5: Forme moyenne de l'écoulement. Les conditions expérimentales sont définies au tableau 1.

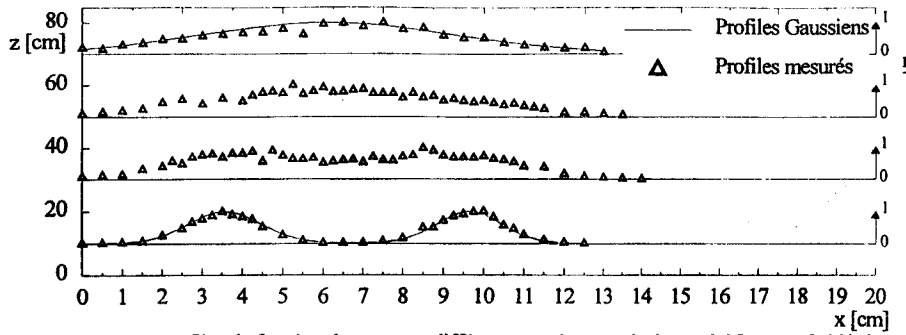

Figure 6: Profiles de fraction de gaz pour différentes stations verticales, s=3.25 cm, q=2.4 l/min.

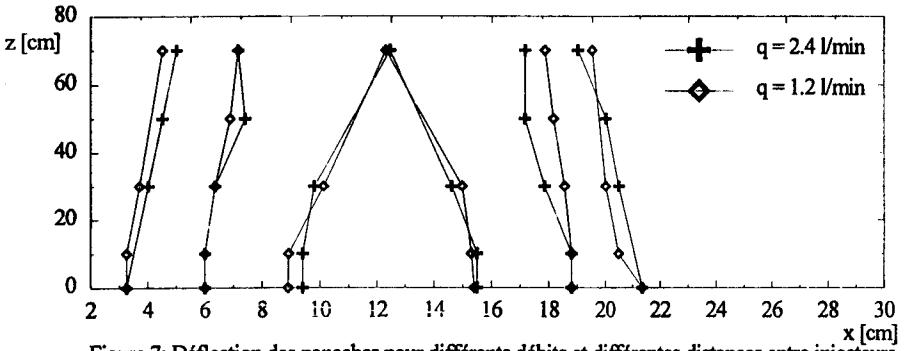

Figure 7: Déflection des panaches pour différents débits et différentes distances entre injecteurs.

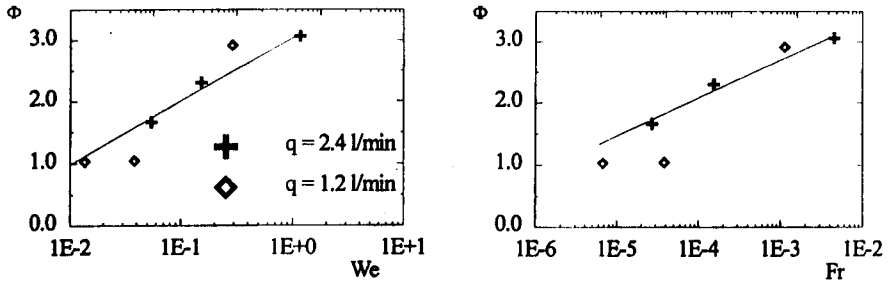

Figure 8: Angle de déflection en fonction du nombre de Weber et du nombre de Froude.

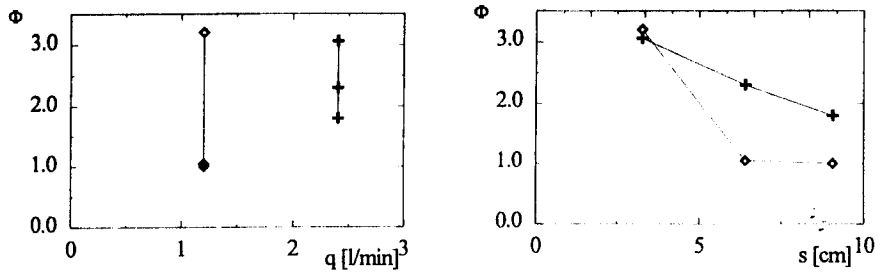

Figure 9: Angle de déflection en fonction du débit et de la demi distance entre les sources.

V CONCLUSION

Le présent travail a établi une corrélation forte entre l'angle de déflection d'un panache de bulles et les valeurs des numéros de Froude et de Weber modifiés. Il initie une nouvelle banque de données sur une configuration de panaches de bulles d'air largement rencontrée dans l'industrie. Ces résultats doivent permettre de modéliser le coefficient d'entrainement par une corrélation avec les deux paramètres définis ici. C'est l'objectif d'une étude en cours de réalisation.

Remerciements. Les auteurs veulent ici remercier Leslie J. S. Bradbury pour avoir projeté, confeccionné et réalisé l'instrumentation utilisée dans cette étude. Les deux premiers auteurs remercient le CNPq pour son aide financière sous forme de bourses No 831024/98-4 et 15007/97-3 respectivement. Le travail a reçu un support financier du CNPq à travers une bourse No 350183/93-7.

REFERENCES

Barbosa, J. R. J. and Bradbury, L. J. S., 1996,. Experimental investigations in round bubble plumes. In *Proc. 6th ENCIT/LATCYM*, Florianopolis.

Brevik, I. and Killie, R., 1996,. Phenomenological description of the axisymmetric air-bubble plume. *Int. J. Multiphase Flow*, 22(3).

Castillejos, A. H. and Brimacombe, J. K., 1987a,. Measurement of physical characteristics of bubbles in gas-liquid plumes: Part i. an improved electroresistivity probe technique. *Metall. Trans. B*, 18B.

Castillejos, A. H. and Brimacombe, J. K., 1987b,. Measurement of physical characteristics of bubbles in gas-liquid plumes: Part ii. local properties of turbulent air-water plumes in vertically injected jets. *Metall. Trans. B*, 18B.

Chesters, A. K., van Dorrn, M., and Goossens, L. H. J., 1980,. A general model for unconfined bubble plumes from extended sources. *Int. J. Multiphase Flow*, 6.

Ditmars, J. D. and Cederwall, K., 1974,. Analysis of air-bubble plumes. In *Proc. Coastal Engng Conf.*, volume 128.

Herringe, R. A. and Davis, M. R., 1976,. Structural development of gas-liquid mixture flows. *J. Fluid Mech.*, 73.

Joo, S. and Guthrie, R. I. L., 1992,. Modelling flows and mixing in steelmaking ladles designed for single- and dual-plug bubbling operations. *Metall. Trans. B*, 23B.

Kocamustafaogullari, G. and Wang, Z., 1991,. An experimental study on local interfacial parameters in horizontal two-phase bubbly flow. *Int. J. Multiphase Flow*, 17.

leung, W. H., Revankar, S. T., Ishii, Y., and Ishii, M., 1992,. Axial development of interfacial area and void concentration profiles measured by double-sensor probe method. *Int. J. Heat Mass transfer*, 38(3).

Liu, T. J. and Bankoff, S. G., 1993,. Structure of air-water bubbly flow in a vertical pipe – ii. void fraction, bubble velocity and bubble size distribution. *Int. J. Heat Mass transfer*, 36(4).

Mazumdar, D. and Guthrie, I. L., 1995,. The physical and mathematical modelling of gas-stirred ladle systems. *ISIJ International*, 35(1).

Menut, P. P. M., Jr., J. R. B., and Freire, A. P. S., 1998,. On the inteaction between a gas-liquid bubble plume and a wall. In *ENCIT 98*, Rio de Janeiro.

Milgram, J. H., 1983,. Mean flow in round bubble plumes. *J. Fluid Mech.*, 133.

Morton, B. R., Taylor, G. I., and Turner, J. S., 1956,. urbulent gravitational convection from maintained and instantaneous sources. In *Proc. R. Soc. Lond.*, volume A 234.

Nassos, G. P., 1963,. Development of an electrical resistivity probe for void fraction measurements in air-water flow. Technical Report 9, Argonne Report ANL – 6738.

Neal, L. G. and Bankoff, S. G., 1963,. A high resolution resistivity probe for determination of local void properties in gas-liquid flow. *AlChE J.*, 9.

Pera, L. and Gebhart, B., 1975,. Laminar plume interactions. *J. Fluid Mech.*, 68.

Reba, I., 1966,. Applications of the coanda effect. *Sci. Am.*, 214.

Santos, L. C. C. and Freire, A. P. S., 1993,. On round bubble plumes subject to cross flow. In *Proc. 12th COBEM*, Brasilia.

Serizawa, A., Kataoka, I., and Michiyoshi, I., 1975a,. Turbulence structure of air-water bubbly flow – i measuring techniques. *Int. J. Multiphase Flow*, 2.

Serizawa, A., Kataoka, I., and Michiyoshi, I., 1975b,. Turbulence structure of air-water bubbly flow – ii local properties. *Int. J. Multiphase Flow*, 2.

Serizawa, A., Kataoka, I., and Michiyoshi, I., 1975c,. Turbulence structure of air-water bubbly flow – iii transport properties. *Int. J. Multiphase Flow*, 2.

Smith, B. L. and Milelli, M., 1998,. An investigation of confined bubbles plumes. In *Third Int. Conf. on Multiphase Flow*, Lyon.

Sun, K. X., Zhang, M. Y., and Chen, X. J., 1998,. Mesurement of physical characteristics of bubbles in gas-liquid plumes. In *Third Int. Conf. on Multiphase Flow*, Lyon.

Tacke, K. H., Schubert, H. G., Weber, D. J., and Schwerdtfeger, K., 1985,. Characteristics of round vertical gas bubble jets. *Metall. Trans. B*, 16B.

teyssedou, A., Tapucu, A., and Lortie, M., 1988,. Impedance probe to measure local void fraction profiles. *Rev. Sci. instrum.*, 59(3).

Tritton, D. J., 1988,. *Physical Fluid Dynamics*. Oxford University Press, Oxford.

Numerical Study of Turbulent Boundary Layer Flow over a Surface with Step Change in Roughness – A Comparison with Experimental Data

Mila R. Avelino‡
Mechanical Engineering Program (COPPE/UFRJ),
C.P. 68503, 21945-970 Rio de Janeiro, Brazil.

Abstract

A theory for the description of turbulent boundary layer flows is considered for the computation of the effects of a surface step change in roughness. The theory resorts to the concept of displacement in origin to specify a wall function boundary condition for k–ϵ model. An approximate algebraic expression for the displacement in origin is obtained from the experimental data by using the chart method of Perry and Joubert(1963). This expression is subsequently included in the near wall logarithmic velocity profile, which is then adopted as a boundary condition for a k–ϵ modelling of the external flow. The results are compared with the lower atmospheric observations made by Bradley(1968) as well as velocity profiles extracted from a set of wind tunnel experiments carried out by Avelino et al.(1998). The measurements were found to be in good agreement with the theoretical computations. The skin-friction coefficient was calculated according to the chart method of Perry and Joubert(1963) and to a balance of the integral momentum equation. In particular, the growth of the internal boundary layer thichness obtained from the numerical model is compared with predictions of the experimental data calculated by two methods, the "knee" point method and the "merge" point method.

Keywords
Turbulence, Boundary Layer, Surface Roughness, Atmospheric Flows, κ–ϵ model.

1. Introduction

A complete understanding of the effects that a step change in surface roughness has on the properties of a turbulent boundary layer has been the object of several experimental and theoretical investigations in recent years, specially in micrometeorology. Most air flows of pratical interest occur in situations where the roughness, the elevation and the temperature of the terrain is changing. Unfortunately, these conditions often occur at the same time, giving rise to complex flow configurations, in which necessarily a large number of parameters to describe the roughness is required.

The present work is concerned with atmospheric flows that develop over flat terrain with changing surface conditions. In particular, we will be looking at flows which present abrupt changes in surface conditions from one extensive uniform surface to another; the theory to be developed here is, therefore, expected to account for these effects. Here, we will use the κ–ϵ model to describe the properties of the atmospheric boundary layer in the surface layer. The model will use a wall function to represent the velocity profile near the wall so that a local analytical solution for the inner region will be used as a boundary condition for the outer solution. For this reason, this inner solution must

‡ Also: Department of Mechanical Engineering, Rio de Janeiro State University, Rua São Francisco Xavier, 524, Sala 5023, Bloco A, CEP 20550-013, Rio de Janeiro, Brazil.

take into account for local changes in the flow such as those provoked by the changes on the surface roughness. The local changes are here accounted for by logarithmic profiles that take as a characteristic length the displacement in origin; this has been evaluated experimentally by the present author in Avelino et. al.(1998).

The present work is, therefore, an despite its title, twofold. It will show the reader how the κ–ϵ model stands for flows over step changes in surface roughness, and will present some new experimental data specially obtained for the validation of the numerical simulation. Four geometrical configurations will be considered, uniformly smooth and rough surfaces, and surfaces with smooth to rough and rough to smooth changes.

Next, we will present a short review of the work recently published on the subject.

The understanding of the effects that changes on the surface nature have on the flow properties has rested mainly upon field experiments. A difficulty with most studies is the absence of reliable measurements of surface flux. One of the few field studies that has overcome this difficulty has been that of Bradley(1968), who made some simultaneous measurements of both velocity profiles and surface shear stresses in a neutral flow at several positions relative to a discontinuity separating surfaces made of grass, of tarmac and of spikes. Bradley's data are ideal for comparison with theoretical and numerical results. The velocity profiles were compared with the computation of Rao et al.(1974), whereas the surface shear stresses were compared with the theories of Peterson(1969) and of Panofsky and Townsend(1964).

Other atmospheric observations are those based on the bushel-basket experiments over the ice of Lake Mendota in the USA (Stearns(1964) and Lettau(1963)), the studies on the modification of the low level wind profiles based on the Riso Tower observations (Panofsky and Petersen(1972) and Petersen and Taylor(1973)), and a study of flows downwind of a wheat crop leading edge (Munro and Oke(1975)).

In more controlled conditions, in a laboratory environment, detailed measurements have been made about the turbulence over rough surface changes, involving both zero and adverse pressure gradient conditions (Antonia and Luxton(1971 and 1972), Antonia and Wood(1975), Schofield(1975) and Mulhearn(1976, 1978)). All these experiments have concentrated on the development of the internal boundary layer and its internal mean and turbulent structure. Wind tunnel observations can also be found in Krogstad et al.(1992), Krogstad and Antonia(1994) and Shafi and Antonia(1997).

The results obtained in the laboratory for boundary layers have frequently been extended to describe the properties of atmospheric boundary layers with good agreement. However, the inhomogeneity of the earth's surface greatly complicates the application of results and theories established for uniform surfaces. To overcome this difficulty, most information comes from studies of the coastal boundary layer, where extentions of the small-scale approach to the mesoscale, specifically the internal boundary layer (IBL) at the coast, have been discussed by Venkatran(1986) and Shao et al.(1991).

The experiments of the last thirty years have been accompanied by a great deal of theoretical effort. Much of this work is discussed in a recent review by Garratt(1990). Here, we will mention a few.

The atmospheric boundary layer and the problem of surface heterogeneity can be considered on several scales, where different characteristics are attained. For a neutrally stable boundary layer, the flow is normally separated into two regions. On the smallest scale there exists an inner layer, where the effects are confined to the surface layer and the velocity profile is observed to have a logarithmic form; in this case of small-

scale flow and of a neutral IBL responding to changes in surface roughness, analytical solutions were provided in studies by Elliott(1958), Taylor(1968, 1969), Panofsky and Townsend(1964), Plate and Hidy(1967) and Mulhearn(1977). For non-neutral flows, the IBL response to a change in surface roughness has been presented in an analytical solution (Townsend(1965, 1966)). Numerical approaches to the problem include those of Venkatran(1976, 1985), of Peterson(1969), of Shir(1972), of Rao et al.(1974) and of Beljaars et al.(1987).

For more stable or unstable flows, the velocity profile deviates from its logarithmic behaviour. For this kind of problems, where many characteristic scales can be found, asymptotic techniques can be evoked to show that in most situations the velocity profile assumes a logarithmic form for distances sufficiently close to the wall.

A good review text on turbulent boundary layers subjected to sudden perturbations is the article of Smits and Wood(1985); a review of the relevant work on the internal boundary layer is given by Garratt(1990). In the review of rough-wall turbulent boundary layers by Raupach et al.(1991) the effect of the roughness on the mean velocity is reported, considering wind tunnel experiments over rough surfaces as well as natural vegetated surfaces in the atmosphere.

2. Experimental Conditions

The experiments were performed in the low-turbulence wind tunnel of the Laboratory of Turbulence Mechanics of the Mechanical Engineering Department of COPPE/UFRJ. The tunnel is an open circuit wind tunnel with 0.15% of turbulence intensity, with an working section 0.3m wide, 0.3m high, and 2m long. A 3:1 contraction section feeds the working section, which has an ajustable roof, to permit the control of the longitudinal pressure gradient.

To avoid any undesirable adverse pressure gradient, the first (or last) roughness element was always depressed below the smooth surface, its crest being aligned with the smooth surface. The roughn surface configurations are described below. In Case I, two 1.0 m long aluminium sheets were used to provide a long uniform smooth surface. In Case II, the 1.0 m long downstream smooth surface was placed following an aluminium sheet consisting of transversally grooved surfaces with rectangular slats of dimensions 3mm high, 12mm wide, and pitch of 24mm. In Case III, the converse to Case II was realized; the upstream sheet was now smooth, followed by a rough sheet. Case IV was configured by two 1.0 m long aluminium rough sheets, resulting in a uniform rough surface. The present roughness elements characterize a roughness of the type k with $w = 3k$, where w is the cavity width. This geometry is slightly different from those of Perry and Joubert(1963), Perry et al.(1969), Antonia and Luxton(1971), Antonia and Luxton(1972) and Bandyopadhyay(1987).

The roof of the wind tunnel was carefully adjusted to assure a constant pressure. The mean velocity at the center-line of the working section was close to 5.5m/s in all cases, and the measurements were made at distances 0.2m, 0.4m, 0.6m, 0.8m, 1m, 1.05m, 1.1m, 1.15m, 1.2m, 1.3m, 1.4m, 1.6m and 1.8m from the beggining of the working section.

The mean velocity profiles were obtained using a Pitot static probe and a Mensor Pressure Gauge. The mean velocity was also measured with a boundary layer hot-wire operated by a linealized constant temperature anemometer.

Mean velocity profiles and turbulence intensity levels were obtained using a DANTEC hot-wire system series 56N. The boundary layer probe was of the type 55P15. The mean velocity data had a precision of 0.6%.

A detailed description of the experimental set up can de found in Avelino et al.(1998).

3. Two Types of Roughness

Nikuradse(1933) investigated the effects of sand-roughened surfaces on the mean velocity profile in pipes, and found that, at high Reynolds number, the near wall flow becomes independent of viscosity, and is a function of the roughness scale, K, of the pipe diameter, D, as well as of Reynolds number, R. From dimensional arguments and comparison with Prandtl's law of the wall, Nikuradse described the velocity profile in the region near the wall as

$$\frac{u}{u_\tau} = \frac{1}{k} \ln \frac{y}{K} + B\left[\frac{Ku_\tau}{\nu}\right], \tag{1}$$

where u_τ is the friction velocity, k is the von Kármán constant(=0.41), and B is a function of the surface roughness.

Equation (1) was written in an alternative form by Clauser(1954), who cast it as

$$\frac{u}{u_\tau} = \frac{1}{k} \ln \frac{yu_\tau}{\nu} + A - \frac{\Delta u}{u_\tau}\left[\frac{Ku_\tau}{\nu}\right]. \tag{2}$$

Hama(1954) showed that

$$\frac{\Delta u}{u_\tau} = \frac{1}{k} \ln \frac{Ku_\tau}{\nu} + C, \tag{3}$$

which immediately shows that equations (1) and (2) are just the same but written in a different form.

Flows that follow the behaviour set by equations (1) to (3) are said to occur over surfaces of the type "K". Flows, on the other hand, which are apparently insensitive to the characteristic scale K, but depend on other global scale of the flow are termed flows over surfaces of the "D" type. In the latter case, the roughness is geometrically characterized by a surface with a series of closely spaced grooves within which the flow generates stable vortical configurations. To describe the part of the velocity profile that deviates from the logarithmic law in the defect region, we consider that, in the flow region above the rough elements, the mean motion is independent of the characteristic scales associated with the near wall flow. Thus equation (2) may be re-written as

$$\frac{u}{u_\tau} = \frac{1}{k} \ln \frac{yu_\tau}{\nu} + A - \frac{\Delta u}{u_\tau}\left[\frac{Du_\tau}{\nu}\right]. \tag{4}$$

In principle, there is no physical reason why the functions appearing in equations (2) and (4) should have the same form. In fact, the distinct length scales used in the representation of the "K" and "D" type rough wall flows may suggest that a single framework for the description of both types of roughness cannot be devised. However, Moore(1951) showed that a similarity law can be written in a universal form provided

the origin for measuring the velocity profile is set some distance below the crest of the roughness elements.

Writing an expression in a more general form, valid for both types of roughness

$$\frac{u}{u_\tau} = \frac{1}{k} \ln \frac{(y_T + \epsilon)u_\tau}{\nu} + A - \frac{\Delta u}{u_\tau}, \tag{5}$$

where,

$$\frac{\Delta u}{u_\tau} = \frac{1}{k} \ln \frac{\epsilon u_\tau}{\nu} + C_i, \tag{6}$$

and $C_i, i = K, D$; is a constant characteristic of the roughness.

Having worked out an expression for the representation of the velocity profile in the near wall region (expression (5)), let us now argue about its domain of validity and how it relates to the classical asymptotic structure of the turbulent boundary layer.

From an asymptotic point of view, one the important factors in the determination of the flow structure is the correct assessment of the order of magnitude of the fluctuating quantities. For the velocity field, a classical result is that, for flow over a smooth surface, both the longitudinal and the transversal velocity fluctuation components scale with the friction velocity, u_τ. The direct implication of this result is that the fully turbulent region is limited by the scales $(u_\tau^2/U_\infty^2)L$ and ν/u_τ.

All these arguments can easily be formalized through application of the single limit concept of Kaplun(1967). Indeed, an application of the theory of Kaplun (Silva Freire and Hirata(1990)) to the equations of motion, shows that the flow structure consists of two distinct regions determined by specific regions of validity obtained through passage of the single limiting process. The domains defined by the limits quoted above are just the overlap domains of the inner and the outer regions.

For flows over rough surfaces, we have seen that the lower bound of the overlap regions must change, being now a function of the surface geometry. Indeed, in this situation, the viscosity becomes irrelevant for the determination of the inner wall scale because the stress is transmitted by pressure forces in the wakes formed by the crests of the roughness elements. We have also seen that the characteristic length scale for the near wall region must be the displacement in origin. It is also clear that, in either case, roughness of the type "K" or roughness of the type "D", the roughness elements penetrate well into the fully turbulent region so that the new origin for the velocity profile will always be located in the overlap fully turbulent region. Therefore, concerning the κ-ϵ model, it appears that an adequate description of the flow can be given provided the wall boundary condition is written according with equation (5).

4. The Numerical Scheme

The present theory was numerically implemented through the computer code CAST (Computer Aided Simulation of Turbulence, Peric and Scheuerer(1989)). This program has the same structure of other existing fluid flow prediction schemes such as TEAM and TEACH. It is thus a conservative finite-volume method in primitive variables. Differences from those codes arise in the co-located variable arrangement, the discretization scheme, the solution algorithms for the linear equation systems resulting form the discretization, and in the pressure coupling which is adopted to the co-located variable storage

For turbulent flow, the code solves the Reynolds averaged Navier-Stokes equations in connection with the κ–ϵ differential turbulence model of Launder and Spalding(1974). The five empirical constants appearing in the code take on the standard values. Since CAST uses the wall function method for specification of the boundary conditions at the wall, an extension of the program to our case of interest was a relatively straightforward affair. Changes were basically made in the momentum and energy balances at the adjacent to the wall control volumes. Here, we will spare the reader the main implementation details. We just point out that the concept of a turbulent Prandtl number was used.

In all flow simulations, the major modification in the code relied entirely on the manner in which the boundary condition was implemented. The concept of displacement in origin was incorporated to the original code, with a carefully chosen expression for its description. We will discuss that in more detail next.

5. The Displacement in Origin

The determination of the displacement in origin, ϵ, is crucial for the evaluation of the properties of the flow over a rough surface, including all local and global parameters such as the skin-friction coefficient. All graphical methods for its determination, however, assume the existence of a logarithmic region, which may not occur near to a step change in roughness.

An initial estimate of ϵ can be made based on the physics of the problem. For rough surfaces of the k-type, the type of surface studied here, the ratio $\epsilon/k \rightarrow 1.0$ according to the relation (Bandyopadhyay, 1987)

$$\epsilon = const.\ x^m, \qquad m = 0.72. \tag{6}$$

The asymptotic value of ϵ was observed by this author to be reached at a distance of about $1000k$ downstream of the point of surface change.

Here, the values of ϵ were calculated according to the method of Perry and Joubert(1963). Systematically adding an arbitrary displacement in origin to the original profiles, the least square method could be applied to the near wall points to search for the best straight line fit. As mentioned by other authors, this method is extremely sensitive, as small departures in the true value of ϵ will give large differences in the calculated values of C_f.

The estimated values of ϵ are shown in Figures 1 and 2 compared with equation (6). In opposition to the results of Bandyopadhyay(1987), we have found here different values for the exponent in the power law. For the uniformly rough case we found $m = 1.04$, whereas for the smooth-to-rough case we found $m = 0.81$. In the present experiments, the asymptotic value of ϵ was reached at about $x = 400$.

The result is that in the numerical computations the following expressions were used to represent ϵ:

Case uniformly rough.

$$\epsilon = 0.00124\ x^m, \qquad m = 1.04. \tag{7}$$

Case smooth to rough.

$$\epsilon = 0.0118\ x^m, \qquad m = 0.81. \tag{8}$$

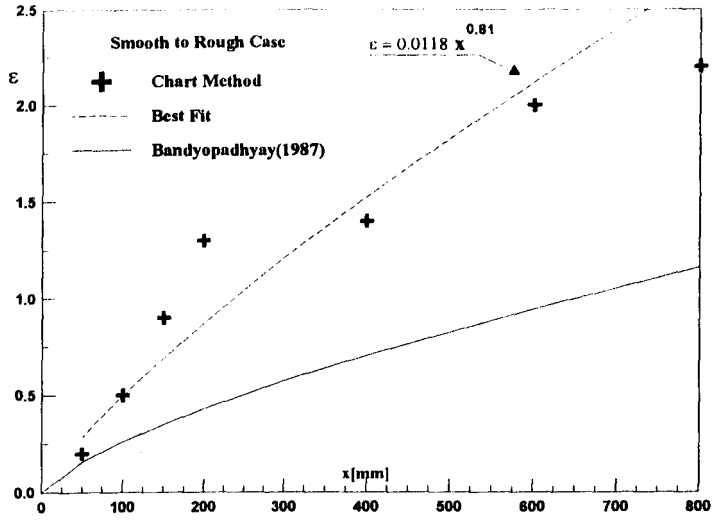

Figure 1. Displacement in origin for the smooth to rough case.

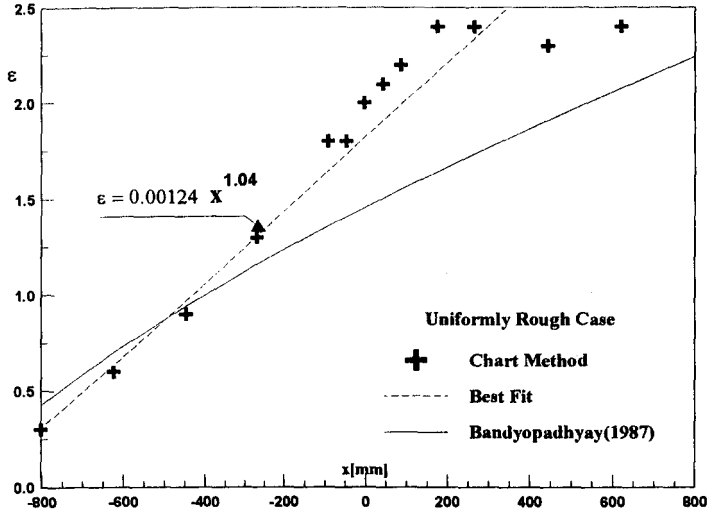

Figure 2. Displacement in origin for the uniformly rough case.

6. Mean Velocity Profiles

The computed mean velocity profiles are shown in Figures 3 to 4 in dimensional coordinates and in a semi-logarithmic form. As expected, both the angular and the linear coefficients of the straight lines are observed to decrease as the flow progresses. In Figure 3, the linear regions cease to exist after the change in surface roughness at $x = 0$. The most interesting feature of this figure, indeed, is the large distortion in the velocity profile at $x = 0$. At this point, no logarithmic behaviour of the velocity profile can be noted. In fact, at the would be logarithmic region a strong "kink" in velocity can be seen. In the rough-to-smooth case (not shown here) the level of the velocity curves were observed to decrease until $x = 0$; at that point, the velocity started to recover to its undisturbed conditions, raising the values of the linear coefficients to the values of the reference uniformly smooth surface curve. Figure 4 displays the flow behaviour for the uniformly rough surface case.

The two figures just introduced must now be presented in non-dimensional form. Here, our problems start.

In principle, Clauser's chart method can be used to evaluate C_f for flows over a smooth surface. In fact, if the classical formulation for the law of the wall is assumed to hold and if the von Karman constant, κ, is really considered constant and equal to 0.41, then the wall shear stress can be estimated directly from the slopes of the straight lines defined in mono-logarithmic graphs. With the values of C_f, the value of the additive "constant", A, in the law of the wall can then be determined. The resulting $A's$ are not constant for some flow conditions but vary with x.

For the flows over rough surfaces, on the other hand, the task of evaluating C_f is much more complex for two parameters, the displacement in origin and the roughness function are previously unknown (Perry and Joubert(1963), Perry, Schofield and Jouber(1969)). If the flow is in a near state of energy equilibrium condition, the chart method of Clauser can be extended to calculate C_f (Perry and Joubert, 1963). The difficulties are many. The most serious one is that the value of C_f is confirmed only by the slope of the logarithmic line and not by its position. In some of our experiments, however, the flow in the vicinity of the point of change in surface roughness is not in equilibrium condition. Thus, any method which presumes the existence of a logarithmic region and searches for values of C_f by distorting the measured velocity profile into a logarithmic curve must be seen with caution.

Due to the uncertainties of the chart method, at least one alternative estimate of C_f had to be provided; this method was based on the application of the momentum integral equation

$$\frac{C_f}{2} = \frac{\theta}{U_\infty}(2 + H)\frac{dU_\infty}{dx} + \frac{d\theta}{dx},$$

where θ is the momentum thickness and $H = \delta_1/\theta$. This equation was used considering the normal stress difference gradients negligible.

Figures 5 and 6 were prepared with the numerical and the experimental data in mono-logarithmic form. The agreement provided by the computations was very reasonable showing that the κ-ϵ model responses well for the law of the wall formulation of expression (6).

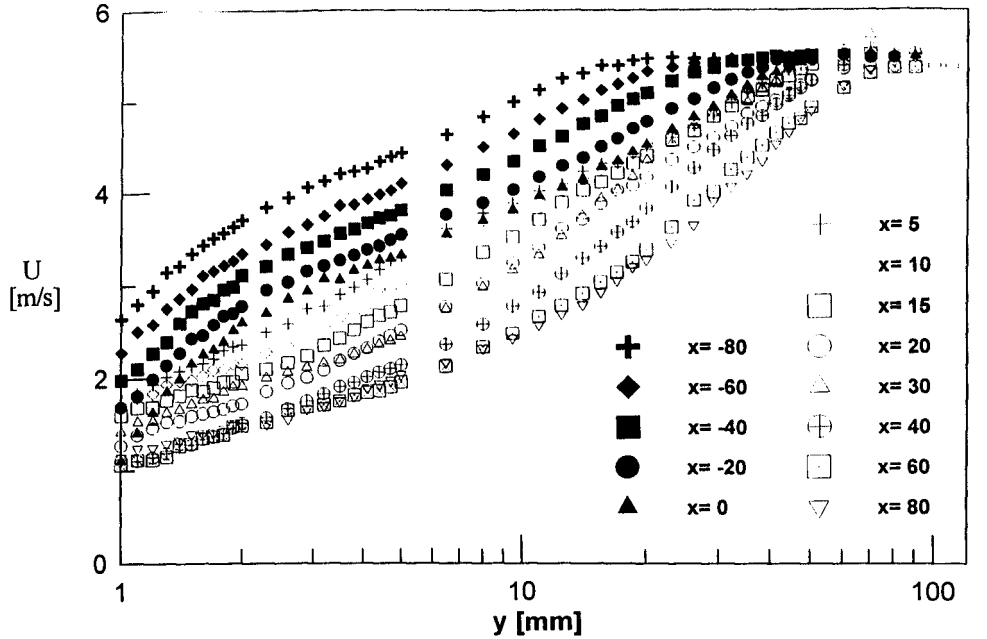

Figure 3. Velocity profiles for the smooth to rough case.

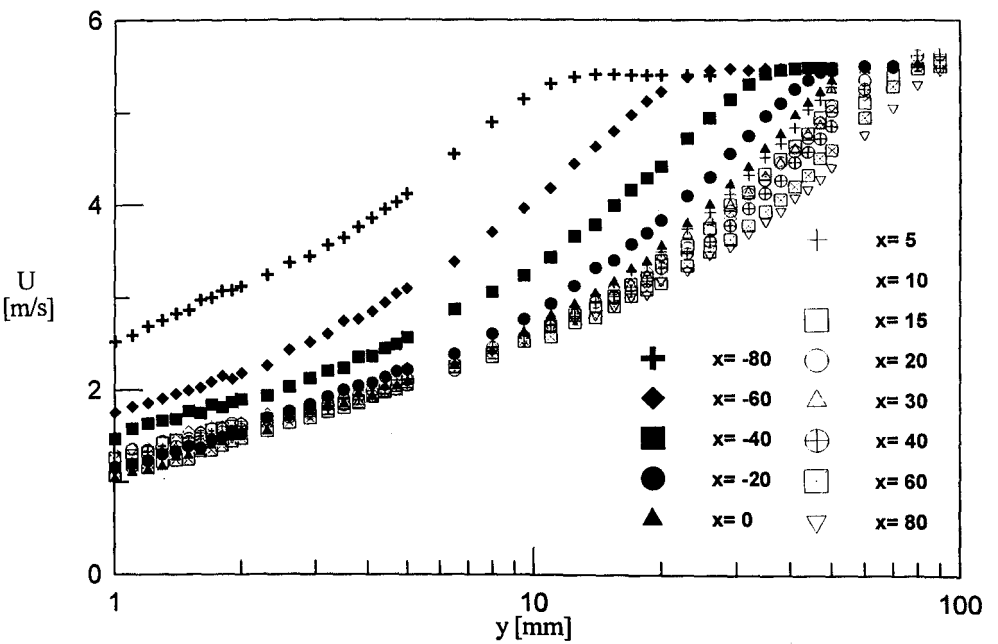

Figure 4. Velocity profiles for the uniformly rough case.

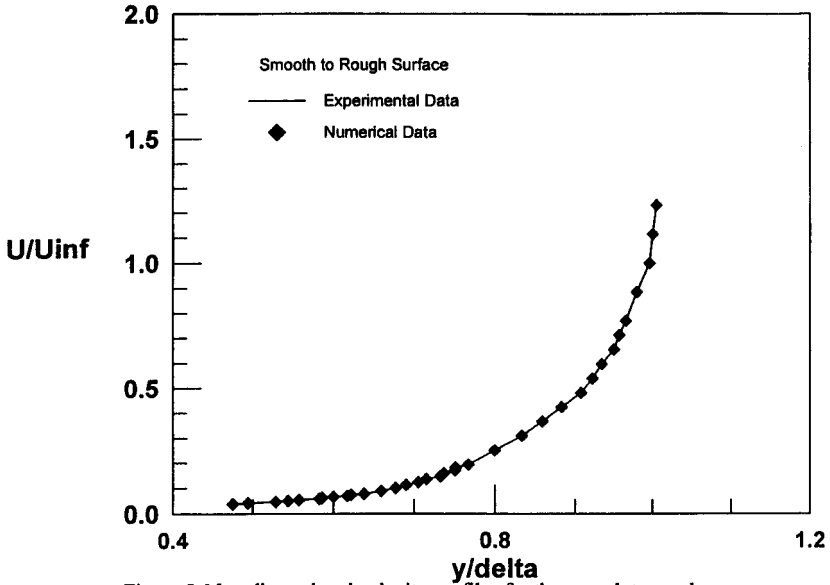

Figure 5. Non-dimensional velocity profiles for the smooth to rough case.

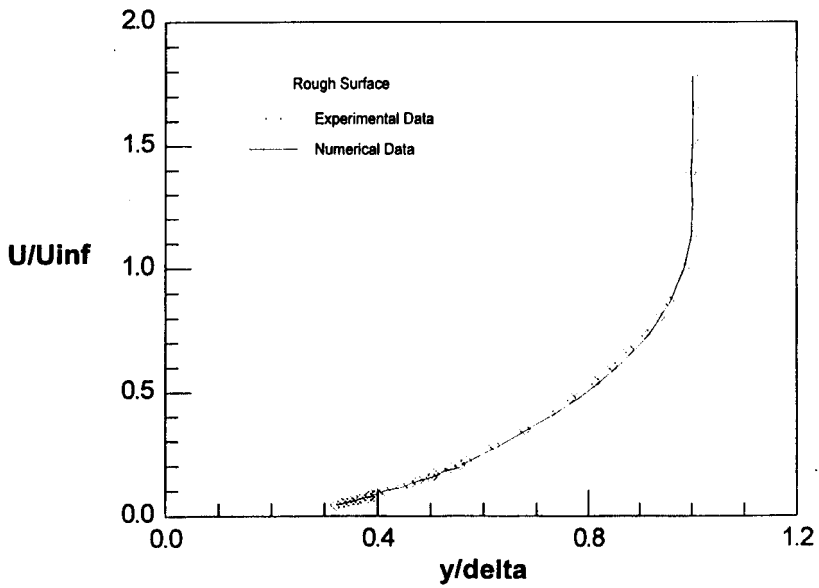

Figure 6. Non-dimensional velocity profiles for the uniformly rough case.

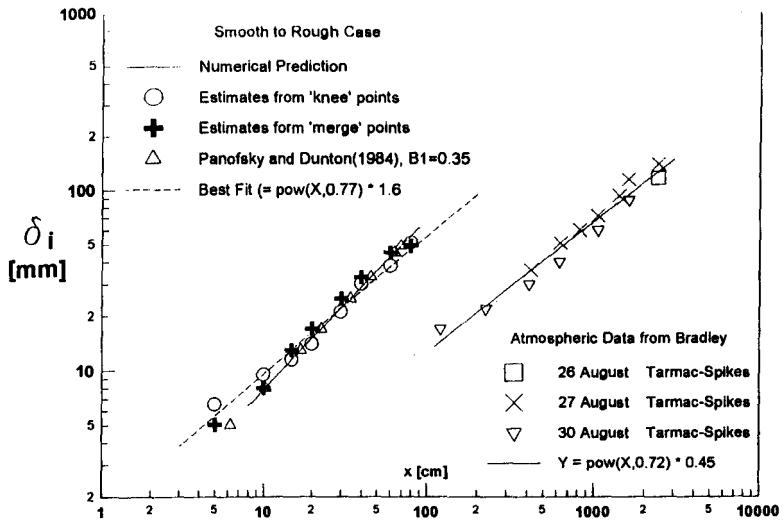

Figure 7. The internal boundary layer thickness, uniformly rough case.

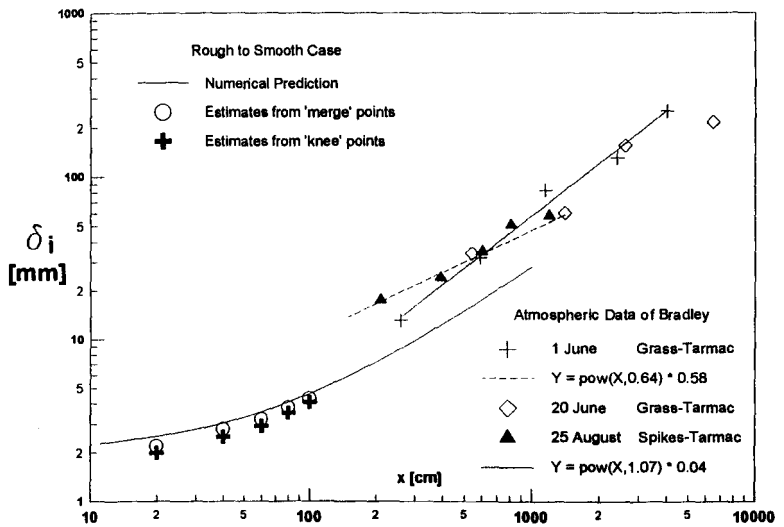

Figure 8. The internal boundary layer thickness, smooth to rough case.

7. The Internal Layer

In addition to the velocity profiles, we want to show how the numerical predictions for the wind-tunnel data can be used to estimate some atmospheric data. To this end, we will compare de present results with the atmospheric data of Bradley(1968).

In literature, several methods have been proposed to determine δ_i. Here, two methods will be used (Antonia and Luxton, 1971). In the first method, δ_i is inferred from the position of merging between two consecutive mean velocity profiles. The resulting points closely coincide with the merging of the turbulence intensity profiles yelding a physically realistic procedure. In the second method, the velocity profiles are ploted against $y^{1/2}$. Under these coordinates, two distinct linear regions appear with different slope coefficients. The intersection of the two straight lines defines the edge of the internal layer.

Considering the diffusive character of the growth of the internal layer and a logarithmic expression for the mean velocity profile, Panofsky and Dutton(1984) derived a logarithmic expression for the growth of δ_i. The resulting numerical values of δ_i are shown in Figures 7 and 8 compared with logarithmic and power-law expressions and the data of Bradley(1968). The physical evidence is that for the rough-to-smooth case the growth rate is much slower than that observed for the smooth-to-rough case. For the rough-to-smooth surface, estimates from the "knee" point method and from the "merge" point method furnished respectively $n = 0.41$ and 0.43. For the smooth-to-rough case, we found $n = 0.77$ and 0.87. In this case, to apply Panofsky and Dutton equation we replaced z_2 by ϵ.

Overall the agreement shown by the computations was very good.

8. Conclusion

A comparison of the present numerical computation with the data of Avelino et al.(1998) and with the data of Bradley(1986) shows that, apparently, the κ-ϵ model can be used to provide predictions of wind-tunnel data as well as atmospheric data over terrains with changing surfaces. Overall, the present data are consistent with the data of other authors; the values of C_f , of ϵ and of δ_i are of the order of the data of Perry and Joubert(1963), of Perry et al.(1969) and of Antonia and Luxton(1971, 1972). Currently, the κ-ϵ model is being put under further escrutiny by the present author in order to demonstrate its capabilitity of predicting flows over rough surfaces.

Acknowledgements. The author is grateful to Prof. A. P. Silva Freire for the enlightning discussions undertaken during the course of the present work. Prof. P. P. M. Menut was very helpful in helping with the experiments.

9. References

Antonia,R. A. and Luxton, R. E., The response of a turbulent boundary layer to a step change in surface roughness Part 1. Smooth to Rough. J. Fluid. Mech., vol 48, pp. 721-761, 1971.

Antonia,R. A. and Luxton, R. E.The response of a turbulent boundary layer to a step change in surface roughness Part 2. Rough to Smooth. J. Fluid. Mech., vol 53, pp. 737-757, 1972.

Antonia,R. A. and Wood,D. H., Measurements in a turbulent boundary layer over a d-type surface roughness, J. Appl. Mech., pp 591–596, 1975.

Avelino, M.R., Menut, P. P. M. and Silva Freire, A. P.; Experimental Characterization of a Turbulent Boundary Layer Subjected to a Step Change in Surface Roughness, Proceedings of the 7th Brazilian National Meeting on Thermal Sciences, November, 1998.

Bandyopadhyay, P.R., Rough-wall turbulent boundary layers in the transition regime. J. Fluid Mech., vol 180, pp. 231-266, 1987.

Bradley, E. F.; A Micrometeorological Study of Velocity Profiles and Surface Drag in the Region Modified by a Change in Surface Roughness. *Quart. J. Roy. Meteor. Soc.*, vol. 94, pp 361-379.

Clauser, F. H.; Turbulent Boundary layers in Adverse Pressure Gradients. *J. Aero. Sci.*, vol. 21, pp 91, 1954.

Elliott, W. P. The Growth of th Atmospheric Internal Boundary Layer. Trans. Amer. Geophys. Un. 39, pp. 1048–1054, 1958.

Hama, F. R.; Boundary Layer Characteristics for Smooth and Rough Surfaces. *Trans. Soc. Nav. Arch. Mar. Engrs.*, vol. 62, pp 333, 1954.

Kaplun, S.; Fluid Mechanics and Singular Perturbations, *Academic Press*, 1967.

Krogstad,P.-A., Antonia,R.A. and Browne,L.W.B., Comparison between rough- and smooth-wall turbulent boundary layers, J. Fluid Mech., 245, 599-617. 1992.

Krogstad P.-A. and Antonia,R.A., Structure of turbulent boundary layers on smooth and rough walls, J. Fluid Mech., 277, 1-21, 1994)

Moore, W. L.; An Experimental Investigation of the Boundary Layer Development Along a Rough Surface. *Ph. D. Thesis*, State University of Iowa, 1951.

Mulhearn, P. J. A Wind-Tunnel Boundary-Layer Study of the Effects of a Surface Roughness Change: Rough to Smooth. Boundary Layer Meteorol. 15, pp. 3–30, 1978.

Nikuradse, J.; Stromungsgesetze in Rauhen Rohren. *V. D. I. Forshungsheft* No 361, 1933.

Panofsky, H. A and Dutton, J. A. Atmospheric Turbulence, Wiley-Interscience, N.Y.,1984.

Peric, M. & Scheuerer, G.; CAST - A Finite Volume Method For Predicting Two-Dimensional Flow and Heat Transfer Phenomena, *GRS- Technische Notiz Srr-89-01*, 1989.

Perry, A. E. & Joubert, P. N.; Rough-Wall Boundary layers in Adverse Pressure Gradients. *J. Fluid Mechanics*, vol. 17, pp 193-211, 1963.

Perry, A. Schofield, W.H. and Joubert, P.N., Rough-wall turbulent boundary layers J. Fluid Mech., vol 37, pp.383-413, 1969.

Rao, K. S., Wyngaard, J. C. and Coté, O. R. The Structure of Two-Dimensional Internal Bondary Layer over a Sudden Change of Surface Roughness. J. Atmos. Sci. 31, pp. 738–746, 1974.

Schofield, W. H. Measurements in Adverse-Pressure-Gradient Turbulent Boundary Layers with a Step Change in Surface Roughness. J. Fluid Mech., vol 70, part 3, pp. 573–593, 1975.

Shao, Y. ,Hacker, J. M. & Schwerdtfeger, P.; The Structure of Turbulence in a Coastal Atmospheric Boundary Layer. it Quart. J. Roy. Meteorol. Soc., vol. 117, pp 1299–1324., 1991.

Silva Freire, A. P. & Hirata, M. H.; Approximate Solutions to Singular Perturbation Problems: the Intermediate Variable Technique. *J. Math. Analysis and Applications*, vol. 145, pp 241-253, 1990.

Smits, A. J. and Wood, D. H. The Response of Turbulent Boundary Layers to Sudden Perturbations. Ann. Rev. Fluid Mech. 17, pp. 321–58, 1985.

Townsend, A. A. The Flow in a Turbulent Boundary Layer after a Change in Surface Roughness. J. Fluid Mech., vol. 26, part 2, pp. 255–266, 1966.

Townsend, A. A. The response of a Turbulent Boundary Layer to Abrupt Changes in Surface Conditions. J. Fluid Mech., vol. 22, part 4, pp. 799–822, 1965.

Venkatram, A. A Model of Internal Boundary-Layer Development. Boundary Layer Meteorol. 11, pp. 419–437, 1977.

Venkatran, A. An Examination of Methods to Estimate the Height of the Coastal Internal Boundary Layer. Boundary Layer Meteorol. 36, pp. 149–156, 1986.

Walmsley, J. L. Internal Boundary-Layer Height Foermulae - A Comparison with Atmospheric Data. Boundary Layer Meteorol. 47, pp. 251–262, 1989.

Interação entre Distribuição de Fases e Estrutura de Turbulência em Escoamentos Bifásicos com Bolhas - Uma Revisão

A. C. R. Castro e Jian Su

Programa de Engenharia Nuclear - COPPE/UFRJ
Caixa Postal 68509 - Rio de Janeiro
CEP. 21945-970

1. Introdução

Escoamentos bifásicos de líquido-gás têm papel importante nos equipamentos e processos industriais de engenharia nuclear, mecânica, química, metalúrgica e petrolífica, tais como trocadores de calor, geradores de vapor, tubulações de misturas bifásicas de líquido-gás, etc. Há um interesse especial devido à análise de segurança de reatores refrigerados à água leve pressurizada (PWR). Portanto, é de extrema importância entender fenômenos físicos em sistemas de escoamentos bifásicos, tais como regimes de escoamento, distribuição de fases e a estrutura do campo de turbulência e prever comportamentos multidimensionais de escoamentos bifásicos com precisão.

Os fenômenos multidimensionais em escoamentos bifásicos são os problemas mais interessantes, desafiantes e difíceis. Infelizmente, devido às complexidades envolvidas, pouco progresso tem sido obtido na análise precisa de escoamento bifásico multidimensional.

Os escoamentos bifásicos apresentam vários padrões de escoamento, tais como escoamentos com bolhas, escoamentos anulares, etc. Sendo que estes padrões são determinados pelas condições da pressão, da velocidade do escoamento, do fluxo de calor e da geometria do canal.

O objetivo do presente trabalho é realizar uma revisão bibliográfica direcionada à escoamentos bifásicos com bolhas na direção vertical para cima, verificando os modelos utilizados na solução de tais problemas. São discutidos, na seção 2, os mecanismos físicos desta interação baseados nos trabalhos experimentais e teóricos. Na seção 3, é apresentada a formulação matemática usualmente utilizada. Os modelos de turbulência são apresentados na seção 4.

2. O Estado da Arte

A maioria dos modelos analíticos são desenvolvidos para fenômenos unidi-

mensionais. Os mais sofisticados destes modelos são baseados na formulação do modelo de dois-fluidos no qual as equações de conservação de cada fase são resolvidas junto com condições apropriadas para o fechamento do problema. O fechamento de tais sistemas é conseguido por postular leis de transferência interfacial e de transferência na parede sólida, que procuram recuperar algumas físicas perdidas durante o processo de média temporal/espacial ou estatística. A abordagem do modelo de dois-fluidos pode ser estendida a escoamentos multidimensionais e tem sido adotada em quase todos os códigos avançados de simulação (RELAP, TRAC, PHOENICS). Infelizmente, há consideráveis incertezas quanto à própria formulação das leis de transferência interfacial, principalmente quanto à distribuição de fases e à estrutura de turbulência.

As equações gerais para escoamentos bifásicos têm recebido muita atenção e tem sido desenvolvidas de várias maneiras. Um desenvolvimento rigoroso de equações de conservação de média temporal para escoamentos bifásicos tridimensionais, chamado de modelo de dois-fluidos, foi feita por Ishii (1975). Além das tensões de Reynolds, essas equações de conservação contêm termos novos de transferência interfacial resultantes do processo de média. Portanto, antes da solução numérica das equações do modelo de dois-fluidos, é necessário constituir as tensões de Reynolds e as forças interfaciais para o fechamento do equacionamento. Os avanços recentes no assunto foram revistados por Lahey (1990) e Lopez de Bertodano et al. (1994).

Uma teoria para descrever os processos de transferência de momento e de calor em escoamentos bifásicos com bolhas em canais verticais foi proposta por Sato et al. (1981). Nesta análise a tensão cisalhante turbulenta e o fluxo de calor turbulento são subdivididos em duas componentes, uma devido a turbulência inerente do líquido e a outra devido a turbulência adicional causada pela agitação das bolhas. É utilizada a hipótese de que as bolhas de gás podem ser tratadas como meros vazios, isto é, que nenhuma transferência de momento acontece na fase gasosa, assim somente o conhecimento das propriedades do escoamento na fase líquida é suficiente para descrever o escoamento.

As tensões resultantes dos dois tipos de turbulência são relacionadas às difusividades turbulentas. Os perfis da velocidade do líquido e da fração de vazio são obtidos experimentalmente. Na região central, distante da parede, os resultados mostram-se válidos através de comparação com dados experimentais, no entanto o mesmo não ocorre para a região próxima à parede.

Considerando escoamentos com altos números de Reynolds de modo que o movimento turbulento plenamente desenvolvido ocorra a uma certa distância da parede enquanto existe uma subcamada viscosa na vizinhança da mesma, as expressões para as difusividades turbulentas são examinadas de modo que descrevam todo o campo do escoamento, desde a vizinhança da parede até a região central do canal. Deste modo, conseguem prever teoricamente a distribuição de velocidade do líquido e o gradiente de pressão friccional quando o perfil da fração de vazio é conhecido.

Utilizando a analogia com escoamento monofásico, a descrição acima para transferência de momento é aceita para ser estendida a problemas de transferência

de calor. O resultado desta análise conduz a cálculos teóricos da distribuição de temperatura do líquido e do coeficiente de transferência de calor, mostrando que as difusividades turbulentas para transferência de calor são iguais àquelas para transferência de momento.

A validade da teoria é testada para ambas as transferências, de momento e de calor, examinando-se a situação para escoamento turbulento com bolhas plenamente desenvolvido em tubo circular, através da comparação dos resultados com dados experimentais. Destas comparações concluem que a teoria para transferência de momento é válida para descrever escoamentos bifásicos com bolhas. Já para a transferência de calor, observam que a concordância dos resultados não é tão boa e supõem ser devido às dificuldades técnicas de medição da temperatura. Assim verificam a necessidade de outros experimentos para validar a teoria relativa à transferência de calor.

Um dos primeiros trabalhos sobre modelagem de turbulência junto com um modelo multidimensional de dois-fluidos foi publicado por Drew e Lahey (1982) que aplicam a teoria de comprimento de mistura para analisar a distribuição de fases em escoamentos com bolhas em tubos circulares. Tratam de um escoamento em especial, que é o escoamento turbulento permanente plenamente desenvolvido de uma mistura axissimétrica adiabática de ar-água. Devido às hipóteses utilizadas, a área da seção transversal é naturalmente dividida em três regiões. Na camada limite na parede, as tensões viscosas, as tensões turbulentas e as forças flutuantes combinam para determinar os perfis de vazio e de velocidade. Perto da linha de centro, verificam que a teoria clássica do comprimento de mistura superestima o efeito da turbulência. Assim, usam uma teoria modificada do comprimento de mistura para esta região. No restante da seção transversal, a teoria padrão do comprimento de mistura é utilizada.

As soluções construídas para cada região requerem pouca informação sobre a estrutura de turbulência e predizem propriamente o efeito observado da orientação do escoamento. Eles conseguem simular qualitativamente o efeito de pico de fração de vazio próximo à parede em escoamento vertical para cima e a concentração de bolhas no centro do tubo em escoamentos para baixo. Assim, mostram que a turbulência pode ser um mecanismo dominante na distribuição de fases lateral.

Cálculos mais elaborados foram realizados por Lee et al. (1989) que adaptam o modelo de duas equações k-ϵ para escoamentos com bolhas. Lopez de Bertodano et al. (1990) estendem esse trabalho para o modelo de tensões de Reynolds para modelar o efeito de anisotropia. O modelo das tensões de Reynolds é mais detalhado, pois substitui as equações para a energia cinética turbulenta por um conjunto acoplado de equações diferenciais para as componentes individuais do tensor de Reynolds. Como consequência, a anisotropia é automaticamente prevista. No entanto, encontram dificuldades computacionais com a baixa velocidade de escoamento. Posteriormente, um modelo novo de tensões de Reynolds foi proposto para contornar as dificuldades (Lopez de Bertodano, 1992).

Serizawa (1974) obteve medidas da distribuição lateral de vazio e das flutuações turbulentas do líquido para escoamento para cima com bolhas num tubo vertical. Alguns dados típicos são mostrados na Figura 1. Pode-se ver um pico na parede para

escoamento com baixos títulos ($< x >$), enquanto o vazio no centro evolui com o aumento do título, e então ocorre *slug flow*.

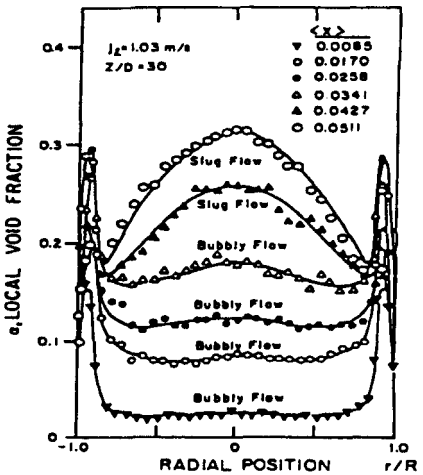

Figura 1 - Distribuição radial de vazio (escoamento para cima)

Uma investigação experimental detalhada do fenômeno de distribuição de fases num tubo foi realizada por Wang et al. (1987). Foram utilizadas sondas especiais de

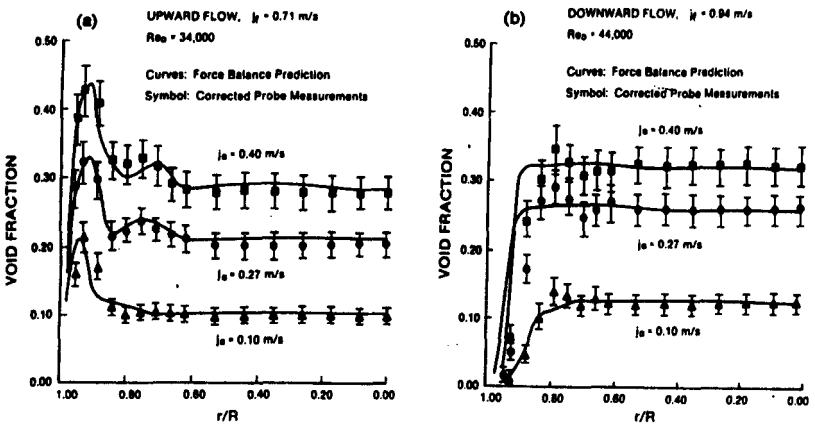

Figura 2 - Perfis de fração de vazio

um único elemento cilíndrico, e de três elementos cônicos para medir a distribuição lateral de vazio tanto quanto todos os componentes do tensor das tensões de Reynolds para ambos os escoamentos, com bolhas subindo e com bolhas descendo. Dados típicos são mostrados nas Figuras de 2 a 5.

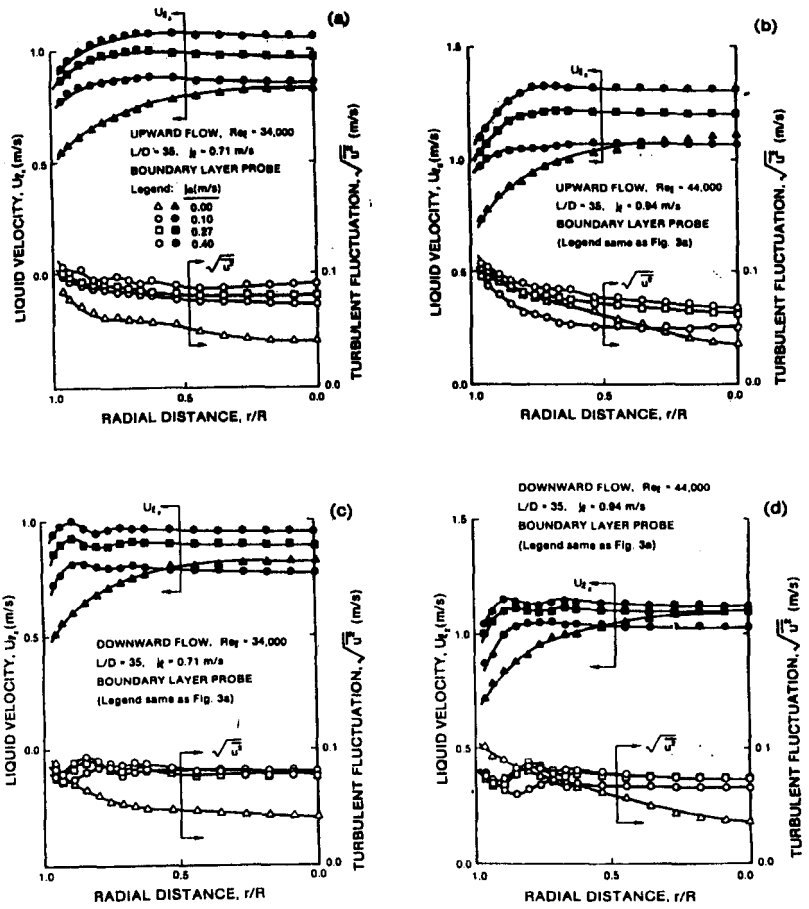

Figura 3 - Velocidade Axial do Líquido e Flutuações Turbulentas

Pode ser visto que, como esperado, a distribuição lateral de vazio é fortemente influenciada pela direção do escoamento. Também pode ser visto pela Figura 3 que, para escoamento bifásico, a velocidade média da fase líquida pode ter um máximo fora da linha de centro para ambos escoamentos, para cima e para baixo. Adicionalmente,

nota-se que as flutuações da velocidade turbulenta bifásica do líquido na direção axial podem estar abaixo daquelas correspondentes a escoamentos monofásicos para grandes números de Reynolds da fase líquida. Isto implica que para tais condições o mecanismo de supressão de turbulência excede os mecanismos de produção de turbulência induzida pelas bolhas. Dados similares foram obtidos por Serizawa (1974).

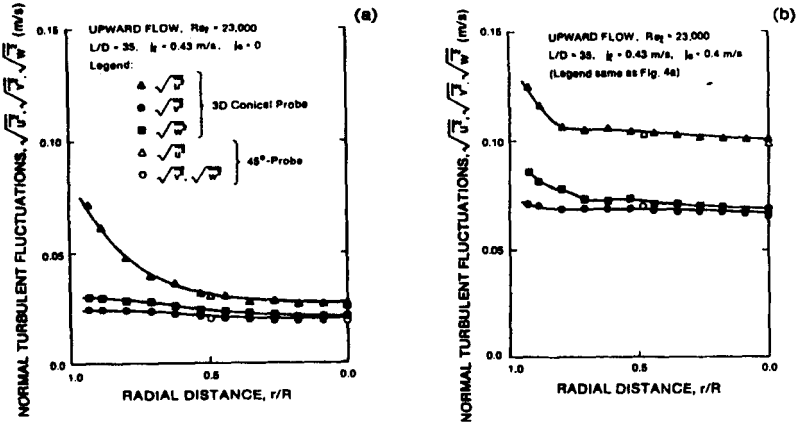

Figura 4 - Flutuações Turbulentas Normais

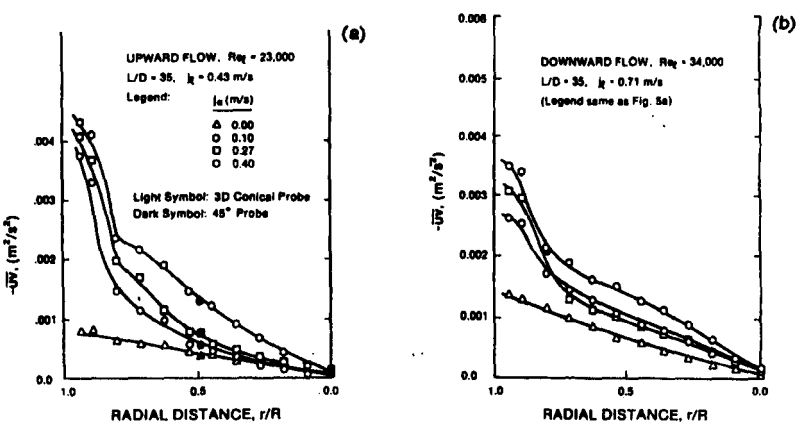

Figura 5 - Medidas de Tensões de Reynolds

Pelas Figuras 4 e 5, é interessante notar algumas medidas típicas das tensões de Reynolds. Vemos na Figura 4 que a estrutura da turbulência é anisotrópica para ambos os escoamentos, monofásico e bifásico. A Figura 5 mostra as tendências das

tensões cisalhantes para escoamentos com bolhas para cima e para baixo. Além disso, pode ser visto que medições redundantes usando sondas diferentes (i.e., uma sonda cônica 3-D e uma sonda cilíndrica a 45°) fornecem essencialmente os mesmos resultados para as várias componentes do tensor de Reynolds.

As distribuições laterais de vazio recentemente foram resumidas em um mapa de *regimes de escoamentos* por Serizawa et al. (1987). Este mapa é mostrado na Figura 6. Pode ser visto que quando a velocidade superficial da fase líquida (j_l) é aumentada, o pico de vazio se afasta da parede. Além disso, quando se aproxima das condições de *slug flow*, vazio no centro é observado.

Do trabalho de Sekogushi et al. (1974), observa-se que o movimento da bolha parece estar relacionado com a distorção da bolha, o local do ponto de injeção, e o número de Reynolds do líquido. Significantemente, é verificado que todas as bolhas esféricas e as bolhas distorcidas maiores que cerca de 3mm de diâmetro não se juntam perto da parede em escoamentos para cima. Enquanto a influência do tamanho da bolha e da distorção na distribuição lateral de fase não é ainda compreendida nos escoamentos bifásicos de importância prática, assume-se que o tamanho da bolha é de grande importância. Portanto, os modelos que devem ser válidos para uma grande variedade de condições devem incluir os efeitos do tamanho da bolha.

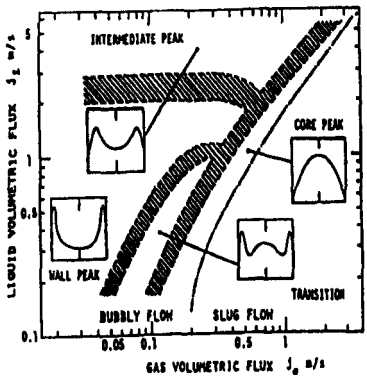

Figura 6 - Um modelo simples de padrões de distribuição de fase

Lahey (1990) utiliza a hipótese que a turbulência é subdividida em duas componentes, uma devido à turbulência inerente do líquido e a outra devida a agitação das bolhas. Aplica o modelo $\tau - \epsilon$ e utiliza a lei da parede como condição de contorno. Os resultados obtidos apresentam boa concordância com os dados de Wang et al. (1987) e de Serizawa et al. (1974). O modelo ainda apresenta a capacidade de predizer ambos os escoamentos, para cima e para baixo. O mesmo modelo é aplicado para a análise de separação de fases.

Um fenômeno particular de supressão de turbulência em escoamento bifásico com bolha foi discutido por Serizawa e Kataoka (1990) baseado em observações expe-

rimentais e em desenvolvimentos teóricos das equações de balanço da energia turbulenta. Definem neste trabalho o fenômeno de supressão da turbulência como sendo a redução local da turbulência no escoamento bifásico. Concluem que a energia turbulenta local da fase líquida pode ser transformada em uma energia requerida para manter a estrutura da superfície e vice-versa. Esta energia relaciona a dissipação de energia turbulenta com o processo de fragmentação dos turbilhões.

O efeito de bolhas no campo de turbulência é muito importante devido a interação entre a distribuição de bolhas e o campo de turbulência. Lance e Bataille (1991), que mediram a turbulência gerada por grades em escoamento bifásico, observaram que a energia cinética da turbulência monofásica gerada por grades e a turbulência induzida por bolhas podem ser linearmente sobrepostas para as condições experimentais realizadas. Theofanous e Sullivan (1982) fizeram a mesma observação para a medida no centro de um tubo a baixa vazão de líquido. No entanto, Serizawa et al. (1986) e Wang et al. (1987), que mediram as tensões de Reynolds e a distribuição de fases em escoamentos com bolhas em tubos, tem observado que à alta velocidade da fase líquida, o nível de turbulência na região central do tubo pode ser mais baixo do que em escoamentos monofásicos, isto é, foi observada a supressão da turbulência. Lopez de Bertodano (1992) obteve dados de turbulência e de distribuição de fases para um duto triangular para demonstrar melhor capacidades multidimensionais do modelo de dois-fluidos.

Um outro aspecto crucial em simulação numérica usando modelo de dois fluidos são as forças interfaciais. A força de arrasto em bolhas tem sido amplamente investigada. Outras como a força de massa virtual e a força de sustentação podem ser deduzidas a partir de princípios básicos para escoamentos não viscosos (Drew e Lahey, 1987, 1990). Em particular, a força de sustentação ou qualquer outra força que atua em direção lateral é muito importante para analisar a distribuição de fases. O comportamento destas forças em escoamentos viscosos turbulentos ainda não é bem entendido.

3. Formulação Matemática para Escoamento Bifásico Médio

A distribuição radial da velocidade média da fase líquida pode ser prevista através da solução das equações de conservação básicas do escoamento bifásico. Para escoamento bifásico, permanente, adiabático, incompressível, plenamente desenvolvido de gás-líquido se movendo verticalmente para cima, as equações de conservação de massa e momento de ambas as fases podem ser dadas por:

$$\frac{D_k}{Dt}\epsilon_k + \epsilon_k \nabla \cdot \overline{u}_k = 0, \quad (k = L, G)$$

$$\epsilon_k \rho_k \frac{D\overline{u}_k}{Dt} = \nabla \cdot \epsilon_k (\overline{T}_k + \tau_k^{re}) + \rho_k g + M_k, \quad (k = L, G)$$

onde, desprezando as tensões viscosas, o tensor de tensões para a fase k é dado por

$$\overline{T}_k + \tau_k^{re} = -p_k I - \rho_k \overline{u_k' u_k'}, \quad (k = L, G)$$

A relação de salto interfacial, desprezando a tensão superficial, é

$$M_G = -M_L = M.$$

As forças interfaciais podem ser decompostas em força de arrasto (M^d) e outras forças (M^{nd}) (Lahey, 1990),

$$M = M^d + M^{nd}.$$

Já que o interesse aqui é no regime de escoamento com bolhas, a força de arrasto interfacial é dada por:

$$M^d = \frac{1}{8}\rho_L C_D |\bar{u}_G - \bar{u}_L|(\bar{u}_G - \bar{u}_L)A_i,$$

onde A_i é a área interfacial e C_D o coeficiente de arrasto. Para escoamentos com bolhas, tendo somente um tamanho de bolha, este parâmetro é dado por:

$$A_i = \frac{6\alpha}{D_b},$$

onde D_b é o diâmetro da bolha.

Para resolver a formulação matemática de modelo de dois-fluidos, é necessário constituir as forças interfaciais e o tensor de tensões de Reynolds, para escoamentos turbulentos com bolhas. Alguns modelos de turbulência propostos para o fechamento de tensões de Reynolds em escoamentos bifásicos serão apresentados a seguir.

4. Modelos de Turbulência

4.1 Modelo Algébrico

Kataoka e Serizawa (1993) em seu trabalho desenvolvem uma correlação teórica do coeficiente de dispersão das bolhas baseados na hipótese de que a difusão das bolhas é devida às colisões entre bolhas e turbilhões líquidos turbulentos, os quais têm tamanhos comparáveis ao tamanho da bolha. Essa correlação concorda com dados experimentais e é dada por:

$$D = \frac{1}{3} d_b v_l'$$

onde D, d_b e v_l' denotam o coeficiente de dispersão das bolhas, o diâmetro da bolha e a velocidade turbulenta do líquido, respectivamente.

Acompanhando tal difusão da bolha está o transporte da fase líquida na direção radial. Como resultado, a tensão turbulenta sobre a fase líquida é induzida pelo movimento da bolha. Baseados neste mecanismo, desenvolveram uma correlação para a difusividade turbulenta da fase líquida induzida pelas bolhas, a qual é dada por:

$$\epsilon_b = \frac{1}{3}\alpha d_b v_l'$$

A tensão turbulenta na fase líquida é composta da tensão induzida pelas bolhas e da tensão turbulenta, a qual é intrinsíca da fase líquida (turbulência da parede).

Como um modelo mais simples, assumiram que a tensão turbulenta intrísica à fase líquida é a mesma do escoamento monofásico. Assumiram, ainda, que a difusividade turbulenta do escoamento bifásico, ϵ_{mtp}, é simplesmente dada pela soma da difusividade turbulenta induzida pelas bolhas e da difusividade turbulenta intrísica da fase líquida.

$$\epsilon_{mtp} = \epsilon_{sp} + \epsilon_b$$

$$\epsilon_{sp} = l_{sp} v_l'$$

onde ϵ_{sp} é a difusividade turbulenta e l_{sp} é o comprimento de mistura do escoamento monofásico.

Baseados nas equações acima, dão a difusividade turbulenta do líquido como sendo

$$\epsilon_{mtp} = \left[l_{sp} + \left(\frac{1}{3}\right) \alpha d_b \right] v_l'$$

Essa equação indica que o comprimento de mistura no escoamento bifásico, l_{tp}, é dado por:

$$l_{tp} = l_{sp} + \left(\frac{1}{3}\right) \alpha d_b$$

Baseando-se na difusividade turbulenta e no comprimento de mistura desenvolvidos anteriormente, previram a distribuição radial da velocidade média da fase líquida através das equações básicas de conservação do escoamento bifásico. Para escoamento bifásico permanente desenvolvido de gás-líquido se movendo verticalmente para cima, as equações de conservação de massa e momento de ambas as fases são dadas por:

$$\frac{\partial}{\partial z}(\alpha_k V_k) = 0 \qquad (k = g, l)$$

$$-\alpha_k \frac{\partial P_k}{\partial z} - \frac{1}{R-y} \frac{\partial}{\partial y}[(R-y)\alpha_k \tau_k] + \alpha_k \rho_k g + M_k^D = 0$$

onde α_k é a fração de vazio e M_k^D é a força de arrasto interfacial, as quais satisfazem as seguintes relações:

$$\alpha_g + \alpha_l = 1$$

$$M_g^D + M_l^D = 0$$

Assumem que os gradientes de pressão de ambas as fases são iguais, isto é,

$$\frac{\partial P_g}{\partial z} = \frac{\partial P_l}{\partial z}$$

e que o momento da fase gasosa é desprezível comparada com o da fase líquida. Baseados nestas hipóteses reduzem as equações de conservação em uma equação diferencial ordinária para a velocidade da fase líquida, tendo a fração de vazio α

e a tensão turbulenta cisalhante τ_l como parâmetros. Deste modo, as equações de conservação são dadas como:

$$\frac{\partial}{\partial z}(\alpha V_l) = 0$$

$$-\alpha\frac{\partial P}{\partial z} - \frac{1}{R-y}\frac{\partial}{\partial y}[(R-y)\alpha\tau_l] + \alpha\rho_l g + M_l^D = 0$$

Com as seguintes condições de contorno:

$$V_l = 0 \qquad y = 0$$

$$\frac{\partial V_l}{\partial y} = 0 \qquad y = R$$

Utilizando analogia com escoamento monofásico e baseando-se na correlação da difusividade turbulenta do líquido, ϵ_{mtp}, a tensão turbulenta cisalhante é dada por:

$$\tau_l = C_0\left[l_{sp} + \left(\frac{1}{3}\right)\alpha d_b\right]v_l'\frac{\partial V_l}{\partial y}$$

onde C_0 é um coeficiente de amortecimento da difusão turbulenta, l_{sp} é o comprimento de mistura e v_f é a velocidade friccional do líquido. C_0 e l_{sp} são dados por:

$$C_0 = 1 - exp\left(\frac{yv_f}{26\nu_l}\right)$$

$$l_{sp} = 0,4y$$

Deste modo a tensão cisalhante turbulenta no escoamento com bolhas é dada pela equação abaixo:

$$\tau_L = C_0\epsilon_{mtp}\frac{\partial V_L}{dy} = C_0\{l_{sp} + (\frac{1}{3})\alpha d_b\}v_L'\frac{\partial V_L}{dy}.$$

Verificam que a aplicabilidade da equação acima é limitada ao caso de escoamento de líquido relativamente baixo, isto é, de aproximadamente 1 m/s. As distribuições radiais da fração de vazio e da velocidade turbulenta utilizadas são dadas por valores experimentais.

4.2 Modelo de Uma Equação

Kataoka e Serizawa (1993) obtêm a distribuição radial das velocidades turbulentas da fase líquida em escoamento turbulento permanente e desenvolvido com bolhas baseando-se na equação de conservação básica da velocidade turbulenta e usando as correlações da difusidade turbulenta e do comprimento de mistura do líquido.

Os autores desenvolvem uma equação de conservação simplificada da energia cinética turbulenta da fase líquida, $k = v_l'^2$, para escoamento permanente e desenvolvido, a qual é dada por:

$$\frac{1}{R-y}\frac{\partial}{\partial y}\left[(R-y)(1-\alpha)\left(\frac{\nu_l}{2}+\beta_2\sqrt{k}\;l_{tp}\right)\frac{\partial k}{\partial y}\right]+\beta_1\sqrt{k}\;l_{tp}(1-\alpha)\left(\frac{\partial V_l}{\partial y}\right)^2$$

$$-\gamma_1(1-\alpha)\frac{(\sqrt{k})^3}{l_{tp}}+K_1\frac{3}{4d_b}\alpha C_D U_T^3=0$$

onde U_T é a velocidade terminal de uma única bolha e C_D é o coeficiente de arrasto de uma bolha. Nesta equação, o primeiro, segundo e terceiro termos representam difusão, geração e dissipação de turbulência, respectivamente. O último termo representa o termo fonte de turbulência devido ao movimento da bolha, e é chamado de termo de geração de turbulência induzida por bolhas. O coeficiente K_1, reflete os efeitos de várias simplificações e aproximações no transporte turbulento na interface gás-líquido.

Como coeficiente de arrasto das bolhas a correlação de Ishii e Chawla foi usada, e é dada por:

$$C_D=\frac{2}{3}d_b\sqrt{\frac{g\Delta\rho}{\sigma}}\left[\frac{1+17,67(1-\alpha)^{1,3}}{18,67(1-\alpha)^{1,5}}\right]^2$$

Para os coeficientes β_1, β_2, γ_1 e K_1 os seguintes valores foram utilizados

$$\beta_1=0,4;\qquad \beta_2=0,15;\qquad \gamma_1=0,15;\qquad K_1=0,05$$

sendo que para β_1, β_2 e γ_1 os valores do escoamento turbulento monofásico foram adotados como uma primeira aproximação. Já o valor de K_1 foi obtido através de tentativa, tal que a predição da distribuição da energia cinética turbulenta concordasse com os dados experimentais.

Fisicamente, as condições de contorno mais rigorosas são dadas por:

$$k=0 \qquad\qquad y=0$$

$$\frac{\partial k}{\partial y}=0 \qquad\qquad y=R$$

Contudo, como na região próxima á parede do tubo, há pouco conhecimento sobre o comportamento da turbulência do escoamento bifásico tanto experimental quanto teoricamente. Assim, como um primeiro passo, a velocidade turbulenta medida, em $y/R = 0,1$, no experimento dos autores foi utilizada como a condição de contorno na parede no lugar da equação da condição de contorno em $y = 0$.

A distribuição radial da fração de vazio é obtida experimentalmente. Os resultados obtidos mostram a importância do termo de geração de turbulência induzida por bolhas na determinação da estrutura de turbulência, principalmente na região central do canal.

4.3 Modelo de Tensões de Reynolds

Lahey (1990) utiliza o modelo de tensões de Reynolds para analisar a distribuição lateral e a separação de fases em escoamentos bifásicos. Nesse estudo, assume propriedades constantes, e assim as pressões das fases são iguais, $p_G = p_L = p$. O coeficiente de arrasto C_D utilizado é o proposto por Wallis (1969):

$$C_D = \frac{6.3}{Re_b^{0.385}}, \qquad Re_b = \frac{D_b|\bar{u}_G - \bar{u}_L|}{\nu_L}.$$

A força lateral de sustentação foi desenvolvida por Drew e Lahey (1987), e é dada para escoamento axissimétrico em canais por:

$$M^{nd} = -C_L \rho_l \alpha (\bar{u}_G - \bar{u}_L) \frac{d\bar{u}_L}{dr}.$$

Pode ser mostrado que o coeficiente de sustentação C_L para uma única bolha em escoamentos não viscosos é 0.5 e pode ser tão pequeno quanto 0.01 para escoamentos muito viscosos. O valor utilizado neste trabalho foi de $C_L = 0.05$.

Para os escoamentos bifásicos nos quais o número de Reynolds da fase contínua indica condições laminares, a turbulência induzida por bolhas pode ocorrer. Tal fenômeno não viscoso pode causar tensões cisalhantes turbulentas induzidas por bolhas da seguinte forma:

$$\tau_l^T = \alpha_G \rho_l [C_1 |\bar{u}_G - \bar{u}_L|^2 I + C_2 (\bar{u}_G - \bar{u}_L)(\bar{u}_G - \bar{u}_L)],$$

onde:

$$C_1 = \frac{3}{20} \quad \text{e} \quad C_2 = \frac{1}{20}.$$

Um modelo $\tau - \epsilon$ foi desenvolvido por Launder et al. (1975) para escoamento monofásico. O procedimento básico utilizado foi fazer o produto da equação de momento com a velocidade e tirar a média temporal da equação da energia mecânica resultante. Aplicando o mesmo método para escoamento bifásico, o conjunto resultante de equações para a fase líquida é:

$$\alpha_l \frac{D}{Dt}(\overline{u'u'}) = \nabla \cdot \alpha_l [\nu_l (\overline{u'u'}) - (\overline{u'u'u'})] + \alpha_l (P + \phi - 2\epsilon I + S_i).$$

onde o tensor P é o tensor de produção de turbulência, ϕ é o tensor deformação da pressão que atua trocando energia cinética entre os vários componentes do tensor de Reynolds, o parâmetro ϵ é a dissipação da turbulência da fase líquida e S_i é um tensor único para escoamentos bifásicos que representa a fonte de turbulência induzida pelas bolhas.

O tensor de produção de turbulência é obtido de um rigoroso desenvolvimento matemático das equações das tensões de Reynolds:

$$P = -(\overline{u'u'}) \cdot [\nabla(\bar{u}_l) + \nabla(\bar{u}_l)^t],$$

onde a quantidade no colchetes é duas vezes o tensor de deformação.

A outra fonte de turbulência é devida às próprias bolhas. Uma bolha se movendo através de um líquido desenvolve um escoamento transiente em torno dela mesma que induz flutuações na fase líquida. As tensões de Reynolds induzidas por bolhas que ocorrem podem ser aproximadas por:

$$(\overline{u'u'}) = \begin{pmatrix} \frac{4}{5} & 0 & 0 \\ 0 & \frac{3}{5} & 0 \\ 0 & 0 & \frac{3}{5} \end{pmatrix} \frac{1}{4}\alpha|\bar{u}_G - \bar{u}_L|^2.$$

Já que o modelo de turbulência desenvolvido é não linear, ele não pôde somente adicionar esta expressão às tensões calculadas pelo modelo $\tau - \epsilon$. Ao invés disto, as introduziu como um termo fonte nas equações de $\tau - \epsilon$. Para efetuar este procedimento dividiu a equação acima por uma apropriada constante temporal que foi escolhida como,

$$\Omega_i = \frac{1}{C_i} \frac{D_b}{|\bar{u}_G - \bar{u}_L|}.$$

Assim a fonte interfacial de turbulência torna-se:

$$S_i = \begin{pmatrix} \frac{4}{5} & 0 & 0 \\ 0 & \frac{3}{5} & 0 \\ 0 & 0 & \frac{3}{5} \end{pmatrix} C_i \frac{1}{4} \frac{\alpha|\bar{u}_G - \bar{u}_L|^3}{D_b},$$

onde $C_i = 0.02$.

O tensor de deformação da pressão foi modelado como:

$$\phi = -\frac{C_1}{\tau_t}\left\{\left((\overline{u'u'}) - IK\right) - \gamma\left(P - \frac{2}{3}I\bar{P}\right) - \gamma\left(S_i - \frac{2}{3}I\bar{S}_i\right)\right\},$$

onde a constante temporal da turbulência média e a energia cinética turbulenta são dadas, respectivamente, por:

$$\tau_t \equiv C_s \frac{K}{\epsilon}, \qquad K = \frac{1}{2} \text{ Trace } (\overline{u'u'})$$

e os termos associados à produção da energia cinética turbulenta são:

$$\bar{P} = \frac{1}{2} \text{ Trace } P, \qquad \bar{S}_i = \frac{1}{2} \text{ Trace } S_i.$$

A correlação do termo do produto triplo foi dada por:

$$(\overline{u'u'u'}) = -\tau_t(\overline{u'u'})\nabla(\overline{u'u'}),$$

essa equação é uma simplificação da equação de transporte exata de $(\overline{u'u'u'})$.

A dissipação de turbulência foi modelada como:

$$\alpha_l \frac{D\epsilon}{Dt} = \nabla \cdot \alpha_l\left(\nu_l \nabla\epsilon - (\overline{u'\epsilon'})\right) + \alpha_l(P_\epsilon - \epsilon_\epsilon + S_{i\epsilon}),$$

onde $(\overline{u'\epsilon'})$ é o transporte turbulento de dissipação, P_ϵ é a produção de dissipação e ϵ_ϵ é o termo fonte de dissipação. Os modelos de fechamento utilizados para estes termos foram:

$$(\overline{u'\epsilon'}) = C_\epsilon \frac{\epsilon}{K}(\overline{u'u'}) \cdot \nabla\epsilon, \qquad P_\epsilon = C_{\epsilon 1}\frac{\epsilon}{K}\bar{P},$$

$$\epsilon_\epsilon = C_{\epsilon 2}\frac{\epsilon^2}{K}, \qquad S_{i\epsilon} = C_{\epsilon 3}\frac{\epsilon}{K}S_i.$$

As constantes utilizadas no modelo $\tau-\epsilon$ bifásico assumem os conhecidos valores do escoamento monofásico:

$$\gamma = 0.6, \qquad C_S = 0.25, \qquad C_1 = 1.5,$$

$$C_\epsilon = 0.15, \qquad C_{\epsilon 1} = 1.44, \qquad C_{\epsilon 2} = 1.92, \qquad C_{\epsilon 3} = 1.92.$$

As condições de contorno na parede, que são uma parte essencial deste modelo, são dadas por velocidades normais nulas e velocidades tangenciais dadas pela 'lei da parede'. As condições de contorno para as equações de $\tau - \epsilon$ são:

$$(\overline{u'u'}) = C u_*^2,$$

onde, para escoamentos axissimétricos em canais,

$$C = \begin{pmatrix} 5.1 & 0 & 1.0 \\ 0 & 2.3 & 0 \\ 1.0 & 0 & 1.0 \end{pmatrix}.$$

Para a dissipação na parede foi utilizada:

$$\epsilon = \frac{1}{k}\frac{u_*}{y}u_*^2,$$

onde, k é a constante de von Karman ($k = 0.435$).

Conclusão

Neste trabalho, foi feita uma revisão sobre os trabalhos que tratam da distribuição de fases e da estrutura da turbulência em escoamentos bifásicos com bolhas. Foi visto que um dos mais importantes e difíceis aspectos do escoamento bifásico com bolhas é a relação entre o mecanismo de distribuição lateral de fase, a estrutura de turbulência e a estrutura interfacial, que são muito sensíveis ao tamanho da bolha e às formas de distribuição. É esta relação que descreve o campo local do escoamento em termos de interações muito complexas entre estas três estruturas. A fim de minimizar a complexidade do problema, os efeitos da estrutura interfacial são ignorados na determinação da distribuição de fase multidimensional, nos trabalhos analisados. Porém, como pode ser visto na Figura 7, a estrutura interfacial produz uma força

de arrasto que aumenta a turbulência induzida pelas bolhas, modificando o campo de turbulência que tem papel fundamental na determinação da distribuição de fase. Deste modo, verifica-se que mais pesquisas teóricas e experimentais são necessárias para se chegar ao completo entendimento do fenômeno de distribuição de fase no escoamento bifásico com bolhas.

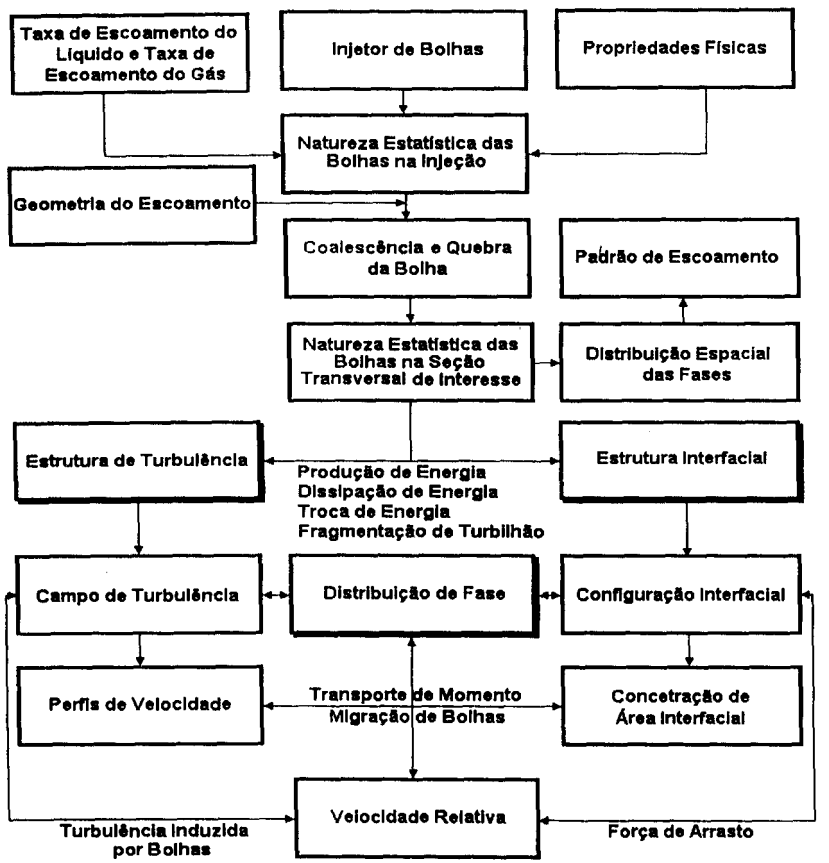

Figura 7 - Apresentação física do escoamento de gás-líquido

Referências Bibliográficas

Drew, D.A. & Lahey, R.T. Jr (1990) Some supplemental analysis concerning the virtual mass and lift force on a rotating and straining flow. *Int. J. Multiphase*

Flow, **16**, 1127-1130.

Drew, D.A. & Lahey, R.T. Jr (1982) Phase-distribution mechanisms in turbulent low-quality two-phase flow in a circular pipe. *J. Fluid Mech.* **117**, 91-106.

Drew, D.A. & Lahey, R.T. Jr (1987) The virtual mass and lift force on a sphere in rotating and straining flow. *Int. J. Multiphase Flow*, **13**, 113-121.

Ishii, M. (1975) *Thermo-fluid Dynamic Theory of Two-Phase Flow.* Eyrolles.

Lahey, R.T. Jr (1990) The analysis of phase separation and phase distribution phenomena using tow-fluid models. *Nucl. Engng. Design* **122**, 17-40.

Lance, M. & Bataille, J. (1991) Turbulence in the liquid phase of a uniform bubbly air-water flow. *J. Fluid Mech.* **222**, 95-118.

Lee, S.-J., Lahey, R, T. Jr & Jones, O. C. Jr (1989) The prediction of tow-phase turbulence and phase distribution phenomena using a k-ϵ model. *Jap. J. Multipahse Flow* **3**, 335-368.

Lopez de Bertodano, M., Lee, S.-J., Lahey, R.T. Jr & Drew, D.A. (1990) The prediction of tow-phase turbulence and phase distribution using a Reynolds stress model. *J. Fluids Engng* **112**, 107-113.

Lopez de Bertodano, M. (1992) Turbulent bubbly tow-pahse flow in a triangular duct. Ph.D. Thesis, Rensselaer Polytechnic Institute, Troy, NY.

Lopez de Bertodano, M., Lee, S.-J., Lahey, R.T. Jr & Jones, O.C. (1994) Phase distribution in bubbly two-phase flow in vertical ducts. *Int. J. Multiphase Flow* **20**,

Sato, Y., Sadatomi, M., & Sekogushi, K. (1981) Momentum and heat transfer in two-phase bubble flow - I. *Int. J. Multiphase Flow*, **7**, 167-177.

Sato, Y., Sadatomi, M., & Sekogushi, K. (1981) Momentum and heat transfer in two-phase bubble flow - II. *Int. J. Multiphase Flow*, **7**, 179-190.

Sekogushi, K., Sato, T. & Honda, T., (1974) Two-phase bubble flow (First report). *Trans. Japan Soc. Mech. Engng.* **333**, 1395-1403.

Serizawa, A. (1974) Fluid dynamic characteristics of two-phase flow. Ph.D. Thesis, Kyoto Univ., Japan.

Serizawa, A., Kataoka, I. & Michiyoshi, I. (1974) Turbulent struture of air/water bubbly flow. *Int. J. Multiphase Flow 2*

Serizawa, A., Kataoka, I. & Michiyoshi, I. (1986) Phase distribution in bubbly flow. *Proceedings of the Second International Workshop on Two-Phase Flow Fundamentals*, Data Set No. 24.

Serizawa, A. & Kataoka, I. (1987) Phase distribution in two-phase flow. *Proc. ICHMT Conf. on Transport Phenomena in Multiphase Flow*, Dubrovnik, Yugoslavia.

Serizawa, A. & Kataoka, I. (1990) Turbulence supression in bubbly two-phase flow. *Nuclear Engineering and Design* **122**, 1-16.

Theofanous, T.G. & Sullivan, J. (1982) Turbulence in two-phase dispersed flows. *J. Fluid Mech.* **116**, 343-362.

Wallis, G.B. (1969) One dimensional two-phase flow. *McGraw-Hill, New York*

Wang, S.K., Lee, S.J., Jones, O.C. Jr & Lahey, R.T. Jr (1987) 3-D turbulence structure and phase distribution measurements in bubbly two-phase flows. *Int. J. Multiphase Flow*, **3**, 327-343.

Estudo Comparativo de Camada Limite Turbulenta Compressível Usando Modelo Algébrico e k-ϵ

Wagner Machado Brasil* e Jian Su†
*Departamento de Engenharia Mecânica e de Materiais - IME
Praça General Tibúrcio 80, Praia Vermelha, Rio de Janeiro, RJ, CEP22290-270
†Programa de Engenharia Nuclear - COPPE/UFRJ
Caixa Postal 68509, Rio de Janeiro, RJ, CEP 21945-970

Abstract

É desenvolvido um estudo comparativo de modelagem de camada limite compressível turbulenta através de modelo de turbulênica algébrico de Cebeci-Smithe e do modelo de duaas equações de Chien. As equações diferenciais de camada limite compressível e de transporte para as quantidades turbulentas são resolvidoas através do método de diferenças finitas, com esquema totalmente implícito e malha numérica adaptativa, num processo de marcha ao longo do escoamento principal. Simulou-se escoamento com gradiente de pressão nulo, favorável e adverso. Os resultados computacionais foram comparados com dados experimentais bem estabelecidas na literatura. Pelo estudo comparativo, conclui-se que os dois modelos de turbulência predizem o escoamento com gradiente de pressão nulo; o modelo de Chien apresenta melhores resultados para gradiente de pressão favorável enquanto o de Cebeci-Smith para gradiente de pressão adverso.

Palavras-chave

Camada Limite, Escoamento Compressível, Escoamento Turbulento, Modelo de Turbulência, Método de Diferenças Finitas

1 Introdução

O crescente progresso da indústria aeronáutica e espacial e o desenvolvimento de foguetes e mísseis tem continuamente estimulado o estudo de camada limite compressível, a qual é caracterizada por grandes variações de massa específica e temperatura, resultado de efeitos de compressibilidade, dissipação viscosa e transferência de calor com a superfície sólida. Essas variações por sua vez influenciam propriedades do fluido como viscosidade e condutibilidade térmica que, diferentemente da camada limite incompressível, passam a ser incógnitas do problema, fazendo-se necessário solucionar o problema térmico e com isso acoplando as equações de Navier-Stokes e da conservação da energia.

No escoamento turbulento o fluxo ou taxa de transporte de quantidade de movimento e calor são mais elevadas que em camada limite laminar devido aos mecanismos de transporte associados com flutuações aleatórias de variáveis como velocidade, temperatura e pressão.

A complexidade do problema de camada limite compressível turbulenta está longe de ser um assunto esclarecido, principalmente com relação aos efeitos da compressibilidade e validação de modelos de turbulência. Revistando o estado da arte em escoamento compressível turbulento, *Bradshaw* [1] afirma que não se conhece como a estrutura da turbulência é alterada pela compressibilidade e que a única certeza em modelagem da turbulência é que nenhum dos modelos existentes irão dar resultados de acurácia satisfátória para solucionar todos os escoamentos de interesse da engenharia. Entre as tentativas ao este problema, *Ristorcelli* [7] argumenta que a média da flutuação da velocidade de Favre pode ser entendida como uma medida dos efeitos da compressibilidade através de varições na massa específica, chegando numa representação matemática para aquela variável.

Este trabalho tem por objetivo estudar a modelagem de camada limite turbulenta compressível, realizando um estudo numérico comparativo entre o modelo de turbulência algébrico de Cebeci-Smith e o modelo de duas equações $\kappa - \varepsilon$ para baixo número de Reynolds

de Chien, junto com a equação algébrica de *Ristorcelli* [7] para a flutação de Favre de velocidade. As equações diferenciais parciais são resolvidas numericamente usando um método de diferenças finitas com malha adaptativa. Serão analisados escoamentos externos com gradiente de pressão nulo, favorável e adverso sobre placa plana e com parede adiabática, fazendo-se uma comparação dos resultados com dados experimentais disponíveis na literatura.

2 Equações de Governo

As equações de governo para camada limite turbulenta compressível, bidimensional, permanente, de um fluido newtoniano são esritas na seguinte forma:

$$\frac{\partial}{\partial x}\left(\overline{\rho}\tilde{u}\right) + \frac{\partial}{\partial y}\left(\overline{\rho}\tilde{v}\right) = 0 \tag{1}$$

$$\frac{\partial}{\partial x}\left(\overline{\rho}\tilde{u}\tilde{u}\right) + \frac{\partial}{\partial y}\left(\overline{\rho}\tilde{u}\tilde{v}\right) = \frac{\partial}{\partial y}\left[\left(\mu + \mu_T\right)\frac{\partial \tilde{u}}{\partial y}\right] - \frac{\partial \overline{p}}{\partial x} + \frac{\partial}{\partial y}\left(\mu\frac{\partial \overline{u''}}{\partial y}\right) \tag{2}$$

$$\frac{\partial}{\partial x}\left(\overline{\rho}\tilde{u}c_p\tilde{T}\right) + \frac{\partial}{\partial y}\left(\overline{\rho}\tilde{v}c_p\tilde{T}\right) = \frac{\partial}{\partial y}\left[\left(\frac{\mu}{Pr} + \frac{\mu_T}{Pr_T}\right)\frac{\partial}{\partial y}\left(c_p\tilde{T}\right)\right] + \\ + \tilde{u}\frac{\partial \overline{p}}{\partial x} + \mu\frac{\partial \tilde{u}}{\partial y}\frac{\partial \tilde{u}}{\partial y} + \overline{u''}\frac{\partial \overline{p}}{\partial x} + 2\mu\frac{\partial \tilde{u}}{\partial y}\frac{\partial \overline{u''}}{\partial y} \tag{3}$$

onde são introduzidas a viscosidade turbulenta, a difusividade térmica turbulenta e o número de Prantdl turbulento através das seguintes definições:

$$-\overline{\rho u''v''} = \mu_T\frac{\partial \tilde{u}}{\partial y} \tag{4}$$

$$-c_p\overline{\rho v''T''} = k_T\frac{\partial \tilde{T}}{\partial y} \tag{5}$$

$$Pr_T = \frac{c_p\mu_T}{k_T} \tag{6}$$

Suponha-se que o fluido satifaça a equação de estado de gás ideal:

$$\overline{p} = \overline{\rho}R\tilde{T} \tag{7}$$

Em escoamentos de número de Prantdl constante entre 0.7 a 1.0, sobre parede adiabática, a equação de energia3 pode ser substituida pela seguinte relação entre a temperatura e a velocidade[4, p. 27]:

$$\frac{\tilde{T}}{T_\delta} = 1 + r\frac{\gamma - 1}{2}M_\delta^2\left[1 - \left(\frac{\tilde{u}}{u_\delta}\right)^2\right] \tag{8}$$

3 Modelos de Turbulências

O modelo de *Cebeci-Smith* [2] é um modelo algébrico de duas regiões, com μ_T sendo determinado por expressões diferentes em cada região.

Na região interna, próxima ao contorno sólido, conhecida como *região de parede*, a viscosidade turbulenta é determinada pela seguinte expressão:

$$\mu_{T_i} = \rho l_{mix}^2\frac{\partial \tilde{u}}{\partial y} \tag{9}$$

$$l_{mix} = \kappa y \left[1 - e^{\left(-y^+/A^+\right)}\right] \tag{10}$$

onde $\kappa = 0.40$ é a *constante de von Kármám* e A^+ é definida como:

$$A^+ = 26 \left[1 + y \frac{dP/dx}{\rho u_\tau^2}\right]^{-1/2} \tag{11}$$

com

$$y^+ = \frac{\overline{\rho} u_\tau y}{\mu} \qquad u_\tau = \sqrt{\frac{\tau_w}{\overline{\rho}}} \qquad \tau_w = \left[\mu \frac{\partial \tilde{u}}{\partial y}\right]_w \tag{12}$$

Na região externa, afastada do contorno sólido, conhecida como *região de esteira*, a viscosidade turbulenta é determinada pela seguinte expressão:

$$\mu_{T_o} = 0.0168 \rho \tilde{u}_\delta \delta_v^* F_{Kleb} \tag{13}$$

A função F_{Kleb} é a *função de intermitência de Klebanoff*, $\tilde{u}_\delta$ é a velocidade média no contorno externo da camada limite e δ_v^* é a *espessura de velocidade*. A função de Klebanoff e a espessura de velocidade são definidos como:

$$F_{Kleb} = \left[1 + 5.5 \left(\frac{y}{\delta}\right)^6\right]^{-1} \qquad \delta_v^* = \int_0^\infty \left(1 - \frac{\tilde{u}}{\tilde{u}_e}\right) dy \tag{14}$$

No código computacional desenvolvido neste trabalho, μ_T é calculado para as duas regiões; se $\mu_{T_i} < \mu_{T_o} \Rightarrow \mu_T = \mu_{T_i}$ caso contrário $\mu_T = \mu_{T_o}$.

O modelo de *Chien* [3] é um modelo de duas equações para baixo número de Reynolds, onde a viscosidade turbulenta é função de duas variáveis determinadas por equações diferenciais de transporte; κ ou energia cinética turbulenta e ε ou dissipação de energia cinética turbulenta.

As equações de κ e de ε para camada limite bidimensional são:

$$\frac{\partial}{\partial x}\left(\overline{\rho}\kappa\tilde{u}\right) + \frac{\partial}{\partial y}\left(\overline{\rho}\kappa\tilde{v}\right) = \frac{\partial}{\partial y}\left[\left(\mu + \frac{\mu_T}{\sigma_\kappa}\right)\frac{\partial \kappa}{\partial y}\right] + \\ + \left(\mu_T \frac{\partial \tilde{u}}{\partial y}\right)\frac{\partial \tilde{u}}{\partial y} - \overline{u''}\frac{\partial \overline{p}}{\partial x} - \overline{\rho}\left(\varepsilon + \varepsilon_0\right) \tag{15}$$

$$\frac{\partial}{\partial x}\left(\overline{\rho}\varepsilon\tilde{u}\right) + \frac{\partial}{\partial y}\left(\overline{\rho}\varepsilon\tilde{v}\right) = \frac{\partial}{\partial y}\left[\left(\mu + \frac{\mu_T}{\sigma_\varepsilon}\right)\frac{\partial \varepsilon}{\partial y}\right] + \\ + C_{\varepsilon 1}\frac{\varepsilon}{\kappa}\left(\mu_T \frac{\partial \tilde{u}}{\partial y}\right)\frac{\partial \tilde{u}}{\partial y} - f_2 C_{\varepsilon 2}\overline{\rho}\frac{\varepsilon^2}{\kappa} + \overline{\rho}E \tag{16}$$

A viscosidade turbulenta é definida como:

$$\mu_T = C_\mu f_\mu \overline{\rho}\frac{\kappa^2}{\varepsilon} \tag{17}$$

As funções de amortecimento, f_1, f_2, f_μ, ε_0 e E são definidas por:

$$f_2 = 1 - 0.22 e^{-(Re_T/6)^2}$$

$$f_\mu = 1 - e^{-0.0115 y^+}$$

$$\varepsilon_0 = 2\frac{\mu}{\overline{\rho}}\frac{\kappa}{y^2}$$

$$E = -2\frac{\mu}{\overline{\rho}}\frac{\varepsilon}{y^2}e^{-y^+/2}$$

As funções de amortecimento dependem de y^+ e do *número de Reynolds turbulento*, $Re_T = \rho\kappa^2/\mu\varepsilon$ As constantes empíricas de fechamento são: $C_{\varepsilon 1} = 1.35$, $C_{\varepsilon 2} = 1.80$, $C_\mu = 0.09$, $\sigma_\kappa = 1.0$ e $\sigma_\varepsilon = 1.3$.

A média da flutuação da velocidade de Favre, $\overline{u''}$, é modelada através de uma equação algébrica proposta por *Ristorcelli* [7].

4 Método Numérico

Um *esquema completamente implícito*, onde aparecem três incógnitas na discretização da equação diferencial, foi empregado. O sistema algébrico de equações que surge com a discretização da equação diferencial geral é solucionado usando-se o *algoritmo de Thomas* [6, p. 52 - 54]. O conjunto de sistemas algébricos associados a cada equação diferencial é resolvido de forma seqüencial em cada estação da marcha.

A camada limite turbulenta apresenta uma estrutura em duas regiões, caracterizada por dois comprimentos de escala distintos. Estes dois comprimentos de escala são utilizados num gerador de malha adaptativa algébrico, que se ajusta automaticamente com as mudanças que ocorrem no domínio físico durante o processo de marcha, sendo mais eficiente que um gerador de malha adaptativa diferencial [8, p. 875 - 876].

Como o comprimento de escala na região de parede é $\mu/\overline{\rho}u_\tau$, é razoável começar a discretização da camada limite com um espaçamento de malha determinado por:

$$\Delta y_1 = r_1 \frac{\mu}{\overline{\rho}u_\tau} \tag{18}$$

onde r_1 é um número usado para especificar o espaçamento próximo à parede como uma fração do comprimento de escala naquela região.

Afastado da parede, na região de esteira, um comprimento de escala relevante é a *espessura de camada limite de perturbação*, δ, definida pela distância entre a superfície e o ponto em que a velocidade é cerca de 99 % da velocidade do escoamento não perturbado. Para progredir do comprimento de escala na região de parede para o comprimento de escala na região de esteira é utilizado um sistema de progressão geométrica, dado por:

$$\Delta\eta_{j+1} = K\Delta\eta_j \tag{19}$$

onde K é a razão entre dois espaços adjacentes da malha.

A distribuição dos pontos da malha vai de $\eta = 0$ até $\eta_{max} = r_2\delta$, onde r_2 é usado para especificar o ponto de discretização mais afastado na direção normal à superfície, cuja ordenada é um múltiplo da espessura de perturbação da camada limite.

O número total de pontos da malha em cada estação da marcha é determinado pelos dois comprimentos de escala naquela estação junto com os três parâmetros computacionais, r_1, r_2 e K.

A solução começa com uma malha arbitrária na primeira estação. A velocidade de atrito, u_τ, e a espessura de perturbação da camada limite, δ, obtidos com a solução da primeira malha são utilizados para gerar uma nova malha, de acordo com as Equações (5.13) e (5.14). Para resolver as equações diferenciais com a nova malha na estação da marcha, a solução da estação anterior precisa ser interpolada na nova malha. Depois das soluções convergirem com a malha adaptada a marcha prossegue a jusante e o processo se repete.

5 RESULTADOS

Serão apresentados resultados numéricos obtidos usando os modelos acima descritos para três casos experimentais, de camada limite turbulenta compressível com gradiente de pressão nulo, favorável e adverso, respectivamente. São os experimentos selecionados para a comparação: o experimento 740218 de *Mabey, Meier e Sawer* [5] por ser o mais confiável [4, p. 74]. Das dezoito combinações possíveis de número de Mach e número de Reynolds oferecidas no experimento foi escolhida a única que apresentava dados de perfis de velocidade e temperatura, no caso, $M_\delta = 4.5$ e $Re_\delta = 2.8\text{x}10^7$. O escoamento escolhido para ser simulado foi o experimento 7401 de *Thomas* [5] por apresentar resultados para gradiente de pressão favorável e adverso, perfis bem detalhados e gradiente de pressão linear [5, p. 7401 A.1 - A.2]. O número de Mach varia entre 2.57 a 3.24 com gradiente de pressão favorável e entre 2.52 e 2.21 com gradiente de pressão adverso e o número de Reynolds está situado na faixa entre 2.5×10^7 e 4.0×10^7.

Os resultados para o coeficiente de atrito para camada limite turbulenta compressível com gradiente de pressão nulo, favorável e adverso são apresentados nas figuras 1 a 3, respectivamente, junto com os dados experimentais. Observamos que os dois modelos apresentam bons resultados para o caso de escoamento sem gradiente de pressão, os resultados para o modelo $\kappa - \varepsilon$ para baixo número de Reynolds foram superiores ao modelo algébrico, enquantio os resultados para o modelo algébrico foram superiores ao modelo $\kappa - \varepsilon$ para baixo número de Reynolds.

As Figuras 4 e 5 apresentam os perfis de velocidade para escoamento com gradiente de pressão favorável e adverso. Observamos que os resultados obtidos usando os dois modelos apresentam excelentes concordância com o dados experimentais no caso de escoamento de gradiente de pressão favorável e o de algébrico ligeiramente melhor no caso de gradiente de pressão adverso.

A Figura 6 apresenta os perfis de temperatura. Observamos novamente boas concordâncias entre os resultados numéricos e os experimentais.

6 CONCLUSÕES

Investigamos o comportamento do modelo algébrico de Cebeci-Smith e do modelo $\kappa - \epsilon$ de Chien em camada limite turbulenta compressível sem e com gradiente de pressão. No equacionamento de camada limite e da equação da energia cinética turbulenta foram considerados termos em que aparecem médias da flutuação da velocidade de Favre ao longo do escoamento $\overline{u''}$ que segundo *Ristorcelli* [7] representam o efeito da compressibilidade sobre o escoamento. O código numérico proposto com método das diferenças finitas e malha adaptativa mostra-se uma ferramenta eficiente na simulação de camada limite turbulenta compressível. O modelo algébrico de Cebeci-Smith e o modelo $\kappa - \varepsilon$ para baixo número de Reynolds de Chien mostraram, de modo geral, desempenho satisfatório na simulação de camada limite turbulenta compressível, embora cada modelo tenha as suas peculiaridades. No escoamento sem gradiente de pressão os dois modelos apresentam excelente desempenho. O modelo $\kappa - \varepsilon$ apresenta desempenho superior em gradiente de pressão favorável, já o modelo algébrico mostra-se superior em gradiente de pressão adverso. O perfil de velocidade gerado pelo modelo $\kappa - \varepsilon$ apresenta característica mais turbulenta que o gerado pelo modelo algébrico, ou seja, um gradiente de velocidade mais acentuado nas proximidades da superfície sólida.

Agradecimento. J.S. agradece o CNPq e a FAPERJ pelos apoios financeiros concedidos durante a realizacão deste trabalho.

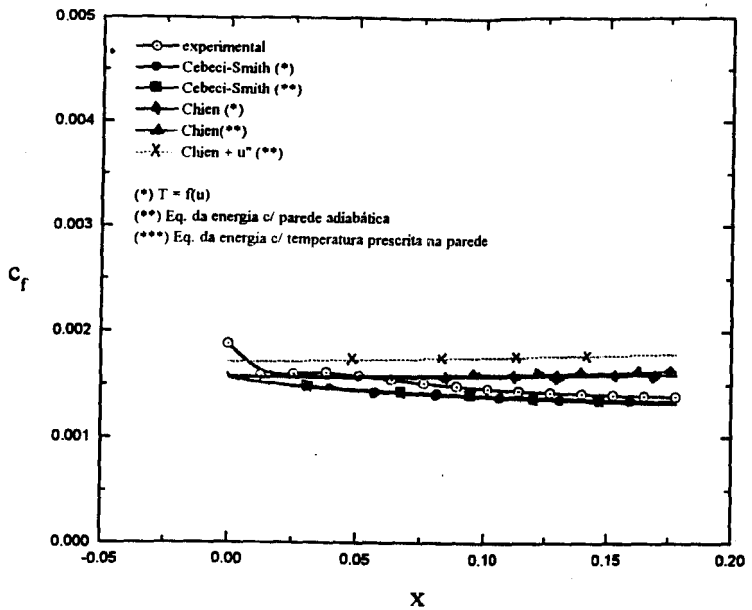

Figure 3: Gradiente de pressão adverso: Coeficiente de atrito.

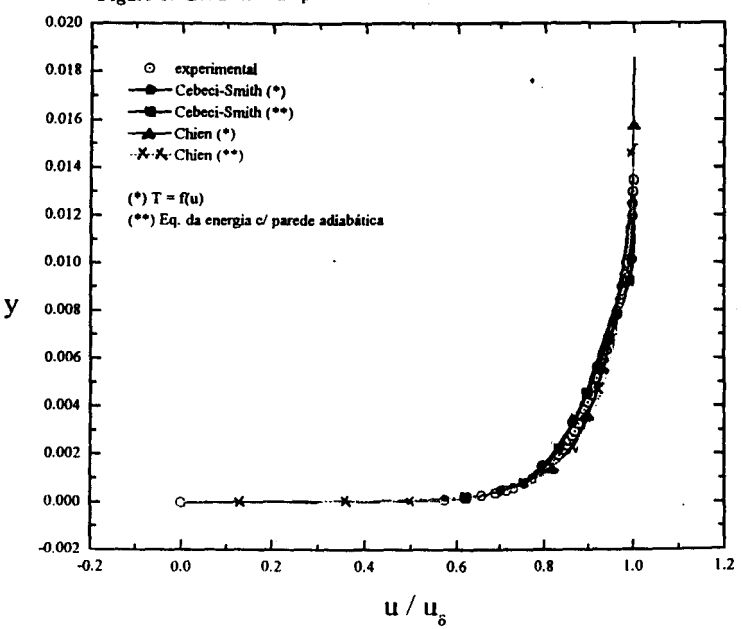

Figure 4: Gradiente de pressão favorável: Perfil de velocidade em x = 0.2032m.

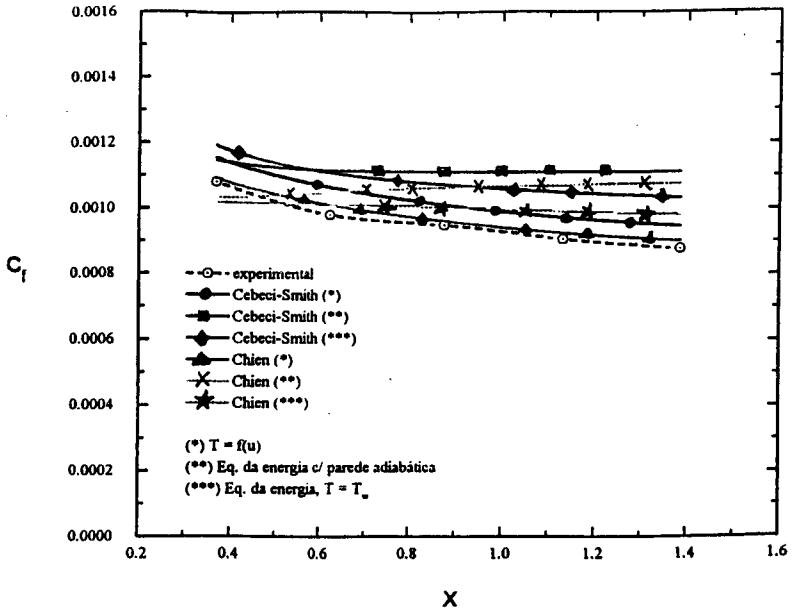

Figure 1: Gradiente de pressão nulo: Coeficiente de atrito.

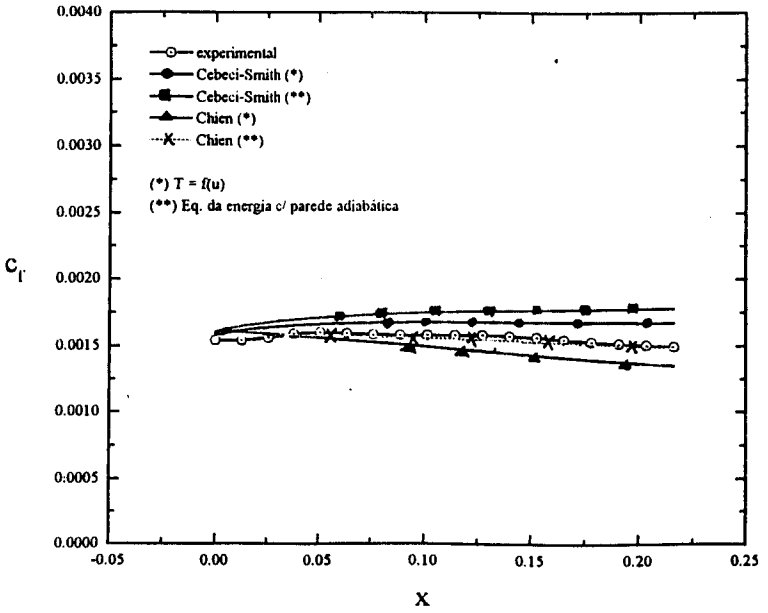

Figure 2: Gradiente de pressão favorável: Coeficiente de atrito.

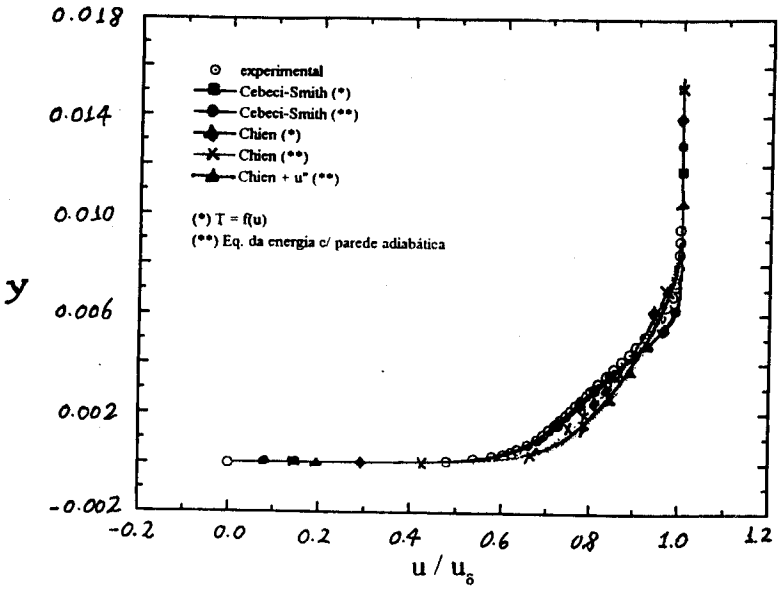

Figure 5: Gradiente de pressão adverso: Perfil de velocidade em x = 0.1778m.

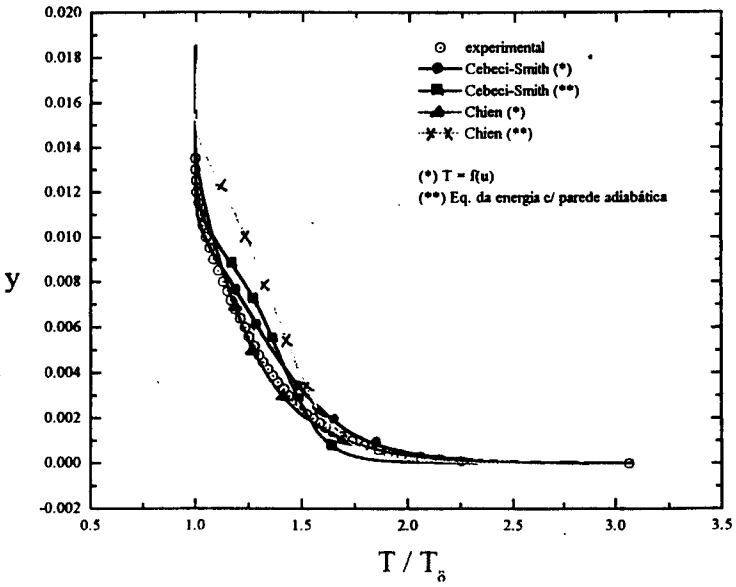

Figure 6: Gradiente de pressão favorável: Perfil de temperatura em x = 0.2032m.

7 REFERENCES

References

[1] BRADSHAW, P. Turbulence Modeling with Apllication to Turbomachinery. Prog. Aerospace Sci., 32:575–624, **1996**.

[2] CEBECI, T. & SMITH, A. M. O. **Analysis of Turbulent Boundary Layer**. Ser. in Appl. Math. & Mech., Vol. XV, Academic Press, 1974.

[3] CHIEN, K. Y. Predictions of Channel and Boundary-Layer Flows with a Low-Reynolds-Number Turbulence Model. AIAA Journal, 20(1):33–38, **1982**.

[4] FERNHOLZ, H. H. & FINLEY, P. J. *A Critical Commentary on Mean Flow Data for Two-Dimensional Compressible Turbulent Boundary Layer - AGARDograph No. 253.* Technical Report, North Atlantic Treaty Organization - Advisory Group for Aerospace Research and Development, **1980**.

[5] FERNHOLZ, H. H. & FINLEY, P. J. *A Critical Compilation of Compressible Turbulent Boundary Layer Data - AGARDograph No. 223.* Technical Report, North Atlantic Treaty Organization - Advisory Group for Aerospace Research and Development, **1977**.

[6] PATANKAR, Suhas V. **Numerical Heat Transfer and Fluid Flow**. Hemisphere Publishing Corporation, 1980.

[7] RISTORCELLI, J. R. A Representation for the Turbulent Mass Flux Contribution to Reynolds-Stress and Two-Equation Closures for Compressible Turbulence. **1996**. Institute for Computer Applications in Science and Engineering - NASA Langley Research Center.

[8] SU, Jian. An Adaptive Nonlinear Coupled Solution Procedure for Turbulent Boundary Layers with Low Reynolds Number Turbulence Models. In IV CEM-NNE, **1996**.

Laboratório de Mecânica da Turbulência, PEM/COPPE/UFRJ
C.P. 68503, 21945-970, Rio de Janeiro